

VELOCITY DISPERSION AND WAVE ATTENUATION
IN RESERVOIR ROCKS

A Dissertation

Presented to

the Faculty of the Department of Earth and Atmospheric Sciences

University of Houston

In Partial Fulfillment

of the Requirements for the Degree of

Doctor of Philosophy

By

Qiuliang Yao

May, 2013

VELOCITY DISPERSION AND WAVE ATTENUATION IN RESERVOIR ROCKS

Qiuliang Yao

APPROVED:

Dr. De-hua Han, Committee Chair

Dr. Leon Thomsen

Dr. Hua-wei Zhou

Dr. Stuart Hall

Dr. Aibing Li

Dr. Colin Sayers

Dean, College of Natural
Sciences and Mathematics

ACKNOWLEDGEMENTS

First of all, I want to express my sincere gratitude to my advisor Dr. De-hua Han for his continuous encouragements and advice during my research. Without his help, it would have been impossible for me to finish the degree, in my forties. I would also like to thank my doctoral committee members, Dr. Leon Thomsen, Dr. Colin Sayers, Dr. Huawei Zhou, Dr. Stuart Hall, and Dr. Aibing Li for their advice, time, and commitment. Their constructive reviews of this dissertation helped improve my research and are greatly appreciated.

I am deeply thankful for the unselfish help and support from Dr. Mike Batzle, Dr. Manika Prasad, Mr. Weiping Wang, and many of the students at the Colorado School of Mines during my research work, especially in developing and calibrating the low frequency measurement system.

I would like to acknowledge the Rock Physics Lab at the University of Houston and all researchers working there. The discussions with my colleagues Huizhu Zhao, Min Sun, Fuyong Yan, and many current and former students including Zijian Zhang, Shenghong Tai, Ayato Kato, and Luanxiao Zhao provided me with constant stimulation and refreshed interest in the studied subjects.

Dr. Kaibo Zhou, as an expert in electronics engineering, offered great assistance in diagnosing and solving various electronics problems in our low frequency

measurement system. He even helped me to design and build a special low signal amplifier which improved the overall performance of the data acquisition subsystem.

I am very grateful to Dr. Mike Myers, Dr. Ronny Hoffman, and Dr. Keith Love of Shell for sharing of their in-house low frequency measurement techniques.

Finally, I am most indebted to my wife Hong and son Tian, for their patience and encouragement. Without their support and sacrifice, I would not be able to enjoy my academic life.

VELOCITY DISPERSION AND WAVE ATTENUATION
IN RESERVOIR ROCKS

An Abstract of a Dissertation
Presented to
the Faculty of the Department of Earth and Atmospheric Sciences
University of Houston

In Partial Fulfillment
of the Requirements for the Degree of
Doctor of Philosophy

By
Qiuliang Yao
May, 2013

ABSTRACT

My dissertation focuses on establishing a link between the rock heterogeneities and the fluid flow-related velocity dispersion and wave attenuation in sedimentary rocks, through both theoretical and experimental studies.

From theoretical studies, I found that the frequency dependency of velocity or modulus is ultimately determined by the amount of additional support the porous frame gets from the fluid, if the fluid is allowed to flow in or out of the pore. An incoming fluid flow stiffens the frame and an outgoing flow softens the frame. A frequency-dependent “Dynamic Fluid Modulus” (DFM) can effectively describe this effect, and model the fluid flow-related velocity dispersion and wave attenuation. Using DFM, the application of Gassmann’s equation is extended from homogeneous to heterogeneous rocks. More importantly, the DFM can be easily and deterministically inverted from measured data. The inverted result is a good indicator of the degree and distribution of heterogeneities in the rock.

For experimental studies, a low frequency measurement system was developed at The University of Houston Rock Physics Lab. This system can measure the velocities and attenuation in rock samples at seismic frequency range (2-500 Hz). As an essential part of the system, a virtual lock-in amplifier was developed to improve the quality and efficiency of the data acquisition and processing. Its performance was carefully evaluated with synthetic and real data. The random errors in our measurements are controlled to be

equal or better than published data. The systematic errors on attenuation (phase) are calibrated to remove the electronic circuit effects. The systematic errors on velocities (amplitude) have to be calibrated with velocities measured at ultrasonic frequency for dry samples. Tests on aluminum, Lucite, and sandstone samples demonstrated that this system can successfully capture the velocity dispersion and attenuation coming from the various fluid flows in sedimentary rocks.

TABLE OF CONTENTS

1	Introduction.....	1
1.1	Motivation.....	1
1.2	Dissertation statement.....	5
1.3	Approach.....	6
1.4	Chapter organization and contributions.....	7
1.5	References.....	8
2	Dispersion and attenuation: heterogeneity.....	11
2.1	Abstract.....	11
2.2	Dispersion and attenuation in sedimentary rocks.....	11
2.2.1	Non-intrinsic attenuation.....	12
2.2.2	Intrinsic attenuation.....	13
2.3	Fluid effect in homogeneous porous media: undrained deformation.....	15
2.4	Fluid effect in inhomogeneous porous media.....	25
2.5	Comments on Pride and Berryman’s double-porosity model (2004 JGR).....	35
2.6	Localized compressibility determines dispersion and attenuation.....	41
2.7	References.....	45
3	Dynamic fluid modulus: dispersion and attenuation from wave-induced fluid flow in heterogeneous porous media.....	49
3.1	Summary.....	49
3.2	Introduction.....	49
3.3	Partial drainage and dynamic fluid modulus.....	50
3.4	Internal fluid flow and bulk compressibility.....	52
3.5	Determination of fluid flow amount q	59
3.6	Example: Dispersion and attenuation in water saturated porous/cracked rocks.....	62
3.7	Inverting dynamic fluid modulus from lab-measured data.....	70
3.8	Discussions.....	88
3.9	Conclusions.....	89
3.10	References.....	90
3.11	Appendix A.....	93
4	Laboratory measurement of dispersion and attenuation at seismic frequency: Principles and limitations.....	97
4.1	Introduction.....	97
4.2	Measurement principle: Force-deformation.....	100
4.2.1	Dispersion: Young’s modulus and Poisson ratio.....	100
4.2.2	Attenuation: phase difference.....	103
4.3	Data acquisition.....	108

4.3.1	Strain gage	108
4.3.2	Wheatstone bridge	109
4.3.3	Lock-in amplifier	111
4.4	System as a whole.....	113
4.5	Limitation.....	117
4.5.1	Frequency range.....	118
4.5.2	Scale of heterogeneity.....	122
4.5.3	Drain effect from pore fluid line.....	124
4.6	References.....	134
5	Lab measurement: System design, build and calibration	137
5.1	Introduction.....	137
5.2	Critical design considerations.....	140
5.2.1	Pressure vessel structure	140
5.2.2	Vibration source.....	143
5.2.3	Virtual lock-in amplifier	146
5.2.3.1	Test on synthetic data.....	148
5.2.3.2	Test on real experimental data	152
5.3	Critical challenges in system building.....	156
5.3.1	Vibration mode and stress distribution	157
5.3.2	Acquisition: small signal protection	166
5.4	Errors and calibrations	167
5.4.1	Phase errors.....	170
5.4.2	Amplitude errors	173
5.5	Tests	175
5.5.1	Test 1: Aluminum	175
5.5.2	Test 2: Lucite	178
5.5.3	Test 3: Rock sample.....	181
5.6	References.....	186
5.7	Appendix A: Matlab code of Virtual Lock-in Amplifier.....	188
6	Conclusions.....	190

LIST OF FIGURES

Figure 2.1 Schematic representations of Maxwell model (left) and Kelvin–Voigt model (right), for a viscoelastic material.	14
Figure 2.2 Three different types of mechanisms to cause pore pressure gradient in porous medium.	20
Figure 2.3 Optical and acoustic vibrations in a linear diatomic chain.	23
Figure 2.4 Pore pressure increment depends on both dry frame bulk modulus and pore fluid modulus.	27
Figure 2.5 Schematic of a micromechanical model to describe the squirt-flow mechanism (after Mavko <i>et al.</i> , 2009).	28
Figure 2.6 A typical velocity dispersion or wave attenuation curve spans about two orders of magnitude in frequency (after Mavko <i>et al.</i> , 2009).	31
Figure 2.7 Measured data on tight gas sandstone show that the dispersion spreads from Hz to MHz frequency range for fluid saturated sample (Measured by Batzle, unpublished).	32
Figure 2.8 Superposition of 12 pairs of relaxation times with a standard linear solid model gives a near constant Q and wide dispersion band (Liu <i>et al.</i> , 1976).	33
Figure 2.9 Reduction of a two-phase heterogeneous composite material with internal flow into an effective homogeneous single phase Biot medium. The effective Biot medium has no internal flow, but with certain frequency dependent moduli, to exhibit an overall viscoelastic behavior.	38
Figure 2.10 In local compressibility approach, consider a volume with a representative pore.	43
Figure 2.11 Modeled dispersion of bulk modulus, based on localized variation on frame dry bulk modulus. $K_0=39\text{GPa}$, $K_f=2.5\text{GPa}$, $K_{dry1}=16\text{GPa}$, $\phi_1=0.1$, $K_{dry2}=1\text{GPa}$	44
Figure 3.1 Partial drainage effect can be equivalent to a modified “Dynamic Fluid Modulus”.....	51
Figure 3.2 Frame stiffness heterogeneity causes pore pressure gradient and internal fluid flow.	53
Figure 3.3 At non-zero frequency, rock is stiffened by an equivalent incoming fluid flow q'	58

Figure 3.4 a) Internal fluid flow. b) Dynamic fluid modulus. c) P-wave velocity dispersion predicted from dynamic fluid modulus (red) and Gassmann prediction (blue). d) P-wave attenuation 1/Q predicted from dynamic fluid modulus. Heterogeneity size=30cm.	61
Figure 3.5 Comparison between P-wave dispersions modeled by dynamic fluid modulus and by Tang's model (2011), using the rock and fluid parameters given in Table 3.2.	68
Figure 3.6 A wide band of dispersion and attenuation is simulated by seven sets of cracks, each set with its own crack density and aspect ratio.	70
Figure 3.7 a) Left. Low frequency measured V_p in three different saturation conditions. b) Right. Attenuation 1/Q under the same conditions as in a. Measurements made with apparatus discussed in chapter 5.	72
Figure 3.8 Inverted dynamic fluid modulus from the data shown in Figure 3.7.	74
Figure 3.9 Dynamic fluid moduli inverted from ultrasonic measurement data using Gassmann equation indicate the rock heterogeneities, and their response to pressure change.	76
Figure 3.10 Inverted dynamic fluid modulus has a negative correlation with porosity. (From Han's data, 1986).	76
Figure 3.11 At a fixed crack density, fluid effect increases with decreasing crack porosity (and aspect ratio), while the dry bulk modulus remain as constant. Calculation performed with equation 3.33 for dry bulk modulus and Gassmann equation for saturated bulk modulus.	79
Figure 3.12 In an elliptical crack dominated sandstone. a) Responses of dry and saturated bulk moduli to increasing pressure. b) Indicated by dynamic fluid modulus, increasing pressure results in higher heterogeneity. Calculated with equation 3.33-3.35.	81
Figure 3.13 In a non-elliptical crack-dominated sandstone. a) Responding to increasing pressure, the dry and low frequency saturated bulk moduli increase much fast compared with elliptical cracked model (Figure 3.12a). b) Indicated by dynamic fluid modulus, increasing pressure results in lower heterogeneity. The results from elliptical crack model also plotted here for comparison. Calculated with equation 3.33-3.35.	82
Figure 3.14 Thin-sections for Fountaiebleau D and Del Light Grey samples.	84
Figure 3.15 Tight gas sandstone: a) Left. Inverse correlation between dynamic fluid modulus and porosity. b) Right. Heterogeneity can either increase or decrease with the increasing pressure, depends on the crack geometry.	85

Figure 3.16 Thin-sections for sample GA2 and samples GA3 in Figure 3.15.....	85
Figure 3.17 Comparison between well-log velocity and ultrasonic velocities for a tight gas sandstone reservoir.	87
Figure 4.1 In ultrasonic measurement, the wavelength is much smaller than the sample size, but for seismic frequency, the wavelength is much larger than the typical core sample, making it impossible to use pulse transient wave and first arrival pick up method to measure velocity.	101
Figure 4.2 Principles for using stress strain relationship to measure elastic moduli of solid sample.	103
Figure 4.3 Stress-strain hysteresis loop, caused by the phase difference between stress and strain. The area inside the elliptical loop represents the energy loss in one cycle of stress-strain disturbance. When the phase difference between strain and stress is zero, the loop reduces to a straight line and no energy loss will occur.....	105
Figure 4.4 Using a standard material with known Young's modulus to stack with sample, the relative measurement eliminate the need to measure stress or force with different sensors and electronics system; therefore reduces the systematic error.	107
Figure 4.5 Strain gage: deformation of length (strain) is reflected in the relative change of resistivity, which can be measured electronically.....	109
Figure 4.6 Schematic of a Wheatstone bridge consists of two standard resistors and two strain gages.....	110
Figure 4.7 The principles of a lock-in amplifier.	111
Figure 4.8 Schematic for low frequency measurement system.	114
Figure 4.9 Program flow chart for automatic measurement through a range of frequencies inputted by users.....	116
Figure 4.10 Screen shot of a live measurement.	117
Figure 4.11 Frequency response for B&K 4810 Small Vibration Exciter.....	119
Figure 4.12 Picture of the vibration system.	121
Figure 4.13 Numerical experiment setup to simulate the effect of fluid drainage at pore fluid line opening, on strain measured at the middle of the sample surface.	127
Figure 4.14 Instantaneous pore pressure distribution after the external stress applied on top of the sample.	129

Figure 4.15 Pore pressure evolution curve at strain gage location, in 0.01 second time span, with various permeability and opening sizes.....	130
Figure 4.16 Pore pressure evolution curve at strain gage location, in 1 second time span, with various permeabilities.....	131
Figure 4.17 Modified fluid boundary condition at pore fluid line opening: connection to a small dead volume of fluid instead of a complete open boundary.....	133
Figure 4.18 With modified boundary condition in Figure 4.17, there is no drainage effect at the strain gage location.....	134
Figure 5.1 Schematic for fixed pressure vessel with moving sample assembly.....	141
Figure 5.2 Schematic for fixed sample assembly with moving pressure vessel.....	142
Figure 5.3 First three periods of synthetic waveforms, with different level of white noises, to test the performance of the lock-in amplifier.....	148
Figure 5.4 Using lock-in amplifier to retrieve amplitude (left) and phase (right) from 10 realizations of synthetic noisy data.....	149
Figure 5.5 Error analysis based on experiments on 10 realizations of synthetic data..	151
Figure 5.6 Typical waveforms from sample Young's gage (left), sample Poisson gage (middle) and Al Young's gage (right). Vibration frequency is 20 Hz. Both time domain waveforms and frequency domain spectra show the signal-noise ratio well above 1.....	151
Figure 5.7 PC Labview program for automatic acquisition, processing, display, and recording.....	152
Figure 5.8 Real data from Ch1 at 20 Hz are mixed with power line noise at 60 Hz, as well as its harmonics at 120 Hz, 180 Hz. The noise amplitudes are 1000 times of the signal amplitude. Top is the waveform in time domain, and bottom is amplitude spectrum in frequency domain.....	154
Figure 5.9 Numerical simulation shows a non uniform strain distribution throughout the cylindrical core plug sample, due to the boundary constraints.....	158
Figure 5.10 Strain variation along the height of the sample. "Arc length" represents the vertical position (bottom to top).....	159
Figure 5.11 With non-welded contacts, the stress in an aluminum sample shows a strong azimuth variation.....	160

Figure 5.12 Numerical experiment setup to simulate the bad contact at center of the interface.....	161
Figure 5.13 Strain distribution throughout the cylindrical core plug sample, with bad contact at center of the interface.	162
Figure 5.14 Strain variation along the height of the sample, with bad contact at center of the interface. “Arc length” represents the vertical position (bottom to top).	163
Figure 5.15 Left: Numerical experiment setup to simulate the bad contact at edge of the interface. Right: Strain distribution throughout the cylindrical core plug sample, with bad contact at edge of the interface.....	164
Figure 5.16 Strain variation along the height of the sample, with bad contact at edge of the interface. “Arc length” represents the vertical position (bottom to top).	165
Figure 5.17 Comparison of random errors on Young’s modulus and Poisson ratio, between our system (left) and Adam <i>et al.</i> , 2006 (right).	168
Figure 5.18 Comparison of random errors on attenuation, among our system (left), Adam <i>et al.</i> , 2006 (right top), and Piane <i>et al.</i> , 2011 (right bottom).	169
Figure 5.19 Introduce a 10mV AC signal to the original DC excitation input terminals, to calibrate the phase shift due to electronics. Left: without strain gage connected. Right: with strain gage connected.	170
Figure 5.20 Phase shift from electronics. Top: without strain gages. Bottom: with strain gages.	172
Figure 5.21 Four strain gages are installed vertically at middle of each cylinder, with even azimuth distribution at 0°, 90°, 180°, and 270° respectively.	177
Figure 5.22 Calibration on Aluminum show no dispersion on Young’s modulus and a negligible attenuation value.	178
Figure 5.23 Measured Young’s modulus, Poisson ratio, and attenuation 1/Q, on a Lucite sample.	179
Figure 5.24 Measured Young’s modulus and Poisson ratio on a sandstone sample.	183
Figure 5.25 Measured attenuation 1/Q on a sandstone sample.....	185
Figure 5.26 Calculated bulk and shear modulus (left), Vp and Vs (right) on a sandstone sample.	186

LIST OF TABLES

Table 3.1 Input parameters used to compute the P-wave dispersion and attenuation in Figure 3.4.	62
Table 3.2 Input parameters used to computer P-wave dispersion in Figure 3.5, after Tang (2011).....	67
Table 4.1 Rock and fluid properties used in numerical simulation of leak drain effect from fluid line opening.	128
Table 5.1 Amplitudes and phases retrieved from synthetic noisy data by virtual lock-in amplifier.....	149
Table 5.2 Comparison between the retrieved amplitudes and phases by Labview lock-in amplifier and Matlab lock-in amplifier, on a real data set acquired at 20 Hz.....	153
Table 5.3 Comparison between the retrieved amplitudes and phases by Labview lock-in amplifier and Matlab lock-in amplifier, on a real data set acquired at 200 Hz.....	153
Table 5.4 Adding 1000 times noises from power line does not affect the lock-in amplifier's performance to retrieve amplitude and phase of low frequency measurement signal.....	155
Table 5.5 The effect of 18 Hz noise on the 20 Hz data.	156
Table 5.6 Special features in hardware and instrumentation to protect the small signals.	166
Table 5.7 Lucite properties measured by ultrasonic transducers (1MHz).	179
Table 5.8 Ultrasonic measured dry properties, as well as low frequency properties predicted by Gassmann fluid substitution.....	182

1 INTRODUCTION

1.1 Motivation

Seismic waves traveling in the subsurface can never be treated as pure elastic waves, since there is always certain levels of anelasticity in natural rocks. This will cause wave energy attenuation and velocity dispersion during its propagation. For example, a global seismology study has observed the shear wave attenuation in the upper mantle and used this information to map the temperature distribution (Bhattacharya, 1996). In sedimentary rocks, seismic wave attenuation and velocity dispersion are well observed in petroleum exploration seismology (Thomas, 1978; Goetz *et al.*, 1979; Stewart *et al.*, 1984; De *et al.*, 1994). Recently, the particular interests are drawn into the fluid flow related seismic wave attenuation and velocity dispersion, because those phenomena are closely related to both the rock and fluid properties (Batzle *et al.*, 2006; Müller *et al.*, 2010) and may provide useful information on detecting the hydrocarbons through seismic techniques.

The foundation of the theories for fluid flow related dispersion and attenuation was established by Biot in a series of papers (*e.g.*, Biot, 1956a, 1956b, 1962). If a viscous fluid in the pore space has a relative movement regarding its hosting solid frame, certain energy will dissipate into heat and cause wave energy attenuation and velocity dispersion. In Biot's discussion, the fluid flow is induced by the pressure difference between the peak and trough of a passing plane seismic wave. The porous media itself is treated as completely homogeneous. The existence of slow P-wave predicted by Biot's theory was

experimentally observed by Plona (1979). And the Biot global flow attenuation in a carbonate aquifer with very high permeability (10-3000Darcy) was observed from crosswell data (Yamamoto, 2003). However, in most of the cases, observed dispersion and attenuation in sedimentary rocks are much stronger than what Biot theory predicts in the seismic domain. It has also been noted that local heterogeneity can also generate pore pressure gradient and thereby cause fluid flow. The first type of heterogeneity is on the different compliance of adjacent pores. When a seismic wave passes through, the fluid stored in those more compliant cracks will be squeezed into those less compliant pores, generating a squirt flow (O'Connell and Budiansky, 1974, 1977; Mavko and Nur, 1975). The second type of heterogeneity is on the fluid compliance. When two or more immiscible fluids with different compressibility coexist in the pore space (a typical case is the gas bubble within brine or oil), a passing pressure wave will cause the phase boundary to oscillate and dissipate the mechanical energy into heat (White, 1975). While the squirt flow models focus on the pore or grain scale of heterogeneity, the idea of compliance heterogeneity has been expanded into the mesoscopic scale in double-porosity and dual-permeability (DPDP) model (Pride and Berryman, 2003a, 2003b). Indeed, the DPDP model is not only a modeling tool for one single mechanism, but a general framework to include all kinds of non-Biot dispersion and attenuation mechanisms.

There are many other proposed theories and models attempting to characterize the dispersion and attenuation phenomenon in sedimentary rocks. They are either detailed treatments of certain particular parameters (*e.g.*, Mavko and Jizba, 1991; Gelinsky and

Shapiro, 1997; Gurevich, 2003; Müller and Gurevich, 2004; Ren *et al.*, 2009) or attempts to unify the local flow mechanism with global flow mechanism with little success (*e.g.*, Dvorkin and Nur, 1993; Jakobsen and Chapman, 2009; Tang, 2011). There is no more new fundamental physical energy dissipation mechanism revealed in those theories.

However, the application of the dispersion and attenuation in exploration is still very limited, and the reason for this lagged application probably comes from two big gaps. The first gap is between the model input parameters and the measurable properties of real rocks; and the second gap is between the model predictions and experimentally proven results.

Almost all of the existing models incorporate some input parameters that are not directly measurable experimentally. With those “tuning knobs”, models can always well predict or match the field data in forward modeling work flow. But the real challenge lies in inversion, since most of the exploration goals are to interpret the data through inversion work flow. Those non-measurable properties are difficult to calibrate; thus impose large non-uniqueness into the inversion results. To make things worse, a typical dispersion/attenuation model involves complicated, highly nonlinear, and multiple-step computations. It is not easy to find an invertible parameter that is also meaningful for the interpretation purposes. This situation motivates us to study the existing theories and models, seeking some new parameters that are physically meaningful, mathematically easy to invert from experimental or field data. More importantly, the hope is that those parameters can contain useful information on the rock or fluid properties.

Traditional laboratory measurements of the velocities in reservoir rocks are conducted in MHz frequency range. Sonic well-logs are in 10 KHz and surface seismic ranges from several Hz to hundreds Hz. Theoretical works reveal that in heterogeneous porous media, there is non-negligible velocity dispersion between those frequency ranges. Therefore, directly measuring velocities at seismic or well-log frequency ranges in laboratory becomes highly desired. Academically, such kind of measurement results can test and calibrate the various theoretical dispersion and attenuation models, and help people to better understand the physical mechanisms behind the observations. Practically, laboratory low frequency velocities on core samples provide important calibration points in applications like seismic-well ties and many inversion work flows. However, the techniques to measure velocity dispersion and attenuation at seismic frequency in laboratory are rarely available and still face some critical challenges. The principles of using the force-deformation method to measure velocities and attenuation in porous core samples were early demonstrated by Liu and Peselnick (1983), and Spencer (1981). This techniques were further developed by Batzle *et al.* (Batzle *et al.*, 2006; Adam *et al.*, 2009), who obtained and published several sets of seismic frequency dispersion and attenuation data for various reservoir rocks. Due to the very high complexity of the measurement techniques, such laboratory measurements are still rarely available to other investigators. This work aims to fill this gap by building a low frequency measurement system in our lab. In short term, the plan is to produce some measurement results which can be cross-calibrated with Batzle's result to prove the reliability and reproducibility of this lab measurement technique. In long term, the goal is to use the lab measurement

results to establish certain empirical relationships between rock/fluid properties and dispersion and attenuation. Finally, the hope is that such data can be used to test the theoretical models and further extend our understanding on the fundamental dispersion and attenuation mechanisms.

1.2 Dissertation statement

The dissertation statement in the dissertation is that current theories and models have provided a good qualitative understanding of the physical mechanisms causing dispersion and attenuation in sedimentary reservoir rocks. They appear to be capable in forward modeling the dispersion and attenuation in some simple cases, but quantitatively, they still lack the ability to fully characterize the dispersion and attenuation in a realistic manner, especially in inversion work flow. Lack of direct laboratory measurements on velocity and attenuation at seismic frequencies also significantly delays the advancement of theoretical understanding and development of practical applications. More efforts are needed to fill those gaps. In theoretical study, the aim is to search for a bridge to relate the model parameters to measurable rock or fluid properties, with focus on providing interpretation power through inversion of data. In laboratory work, the aim is to set up a reliable low frequency measurement system, so that one can obtain real hands-on knowledge about the velocity dispersion and attenuation in reservoir rocks, and use these data to constrain the theoretical model development.

1.3 Approach

This dissertation aims to establish the relationship between the observable velocity dispersion and wave attenuation in reservoir rocks and the heterogeneities of the corresponding rock-fluid system along with their properties. The study is performed in the following procedures:

The first step is to review the evolution of the existing theories and models of dispersion and attenuation in sedimentary rocks. The specific concentration was focused on the Biot's theory as well as Pride and Berryman's double-porosity and dual-permeability theory. The former theory lays out the foundation for all fluid flow related energy dissipation, and the latter theory set up the general relationship between local heterogeneities and wave dispersion and attenuation. Some of the critical comments on those two theories eventually led me to develop a new method to characterize the fluid related dispersion and attenuation in heterogeneous porous rocks.

The second step is to develop a new idea, select a new parameter, and formularize new equations to more explicitly relate the dispersion and attenuation to the heterogeneities of the reservoir rocks. This was done through poroelasticity analysis both in an intuitive approach and a strict mathematical derivation.

The third step is to demonstrate our new model's capability to characterize the dispersion and attenuation in heterogeneous reservoir rocks. Forward modeling is performed and compared with other models. More importantly, it is shown that through

inversion, this new method can help to obtain some parameters which are useful to interpret the heterogeneity features of the rocks and provide new insights on their microstructures.

Paralleling to the theoretical study mentioned above, a laboratory measurement system was designed and built. With this system, velocity dispersion and wave attenuation can be measured in a wide frequency range from 1 Hz to 500 Hz. Along with the ultrasonic measurements at 1 MHz, the fluid relaxation behaviors related to a wide spectrum of heterogeneities were evaluated, which are much more closer to the realistic in-situ subsurface condition in seismic surveys.

1.4 Chapter organization and contributions

The following dissertation comprises two relatively independent parts. The first part consists of chapters 2 and 3 and focuses on the theoretical study on dispersion and attenuation in heterogeneous reservoir rocks. In chapter 2, the fundamental dispersion and attenuation mechanisms are discussed through the critical reviews on major existing models. Chapter 3 presents a new concept, the dynamic fluid modulus, and discusses how to use this concept to relate the dispersion and attenuation to the heterogeneities of reservoir rocks. The second part consists of chapters 4 and 5. Chapter 4 introduces the principles of measuring velocity and attenuation at seismic frequency in laboratory. Chapter 5 documents how the low frequency measurement system in Rock Physics Lab at the University of Houston was designed, built, and calibrated. Chapter 6 summarizes

the achievements from current work and discusses the potential research direction in the future.

1.5 References

Adam, L., M. L. Batzle, and K. T. Lewallen, 2009, Seismic wave attenuation in carbonates: *Journal of Geophysical Research*, **114**, B06208.

Batzle, M. L., D.H.Han, and R. Hofmann, 2006, Fluidmobility and frequency- dependent seismic velocity—Direct measurements: *Geophysics*, **71**, no. 1, N1–N9.

Bhattacharyya, J. G., G. Masters, and P. Shearer (1996), Global lateral variations of shear attenuation in the upper mantle, *Journal of Geophysical Research*, **101**, 22,273–22,290.

Biot, M. A., 1956a, Theory of propagation of elastic waves in fluid-saturated porous solid. I. Low-frequency range: *Journal of the Acoustical Society of America*, **28**, 168–178.

———, 1956b, Theory of propagation of elastic waves in a fluid-saturated porous solid. II. Higher frequency range: *Journal of the Acoustical Society of America*, **28**, 179–191.

———, 1962, Mechanics of deformation and acoustic propagation in porous media: *Journal of Applied Physics*, **33**, 1482–1498.

De, G. S., D.F. Winterstein, and M.A. Meadows, 1994, Comparison of P- and S-wave velocities and Q's from VSP and sonic log data: *Geophysics*, **59**, 1512-1529.

Gelinsky, S., and S. A. Shapiro, 1997, Dynamic-equivalent medium approach for thinly layered saturated sediments: *Geophysical Journal International*, **128**, F1–F4.

Goetz, J. F., L. Dupal, and J. Bowler, 1979, An investigation into discrepancies between sonic log and seismic check shot velocities: *Australian Petroleum Exploration Association Journal*, **19**, 131-141.

Gurevich, B., 2003, Elastic properties of saturated porous rocks with aligned fractures: *Journal of Applied Geophysics*, **54**, 203–218.

Liu, H., and L. Peselnick, 1983, Investigation of internal friction in fused quartz, steel, plexiglass, and Westerly Granite from 0.01 to 1.00 Hertz, *Journal of Geophysical Research*, **88**, 2367-2379.

Mavko, G., and D. Jizba, 1991, Estimating grain-scale fluid effects on velocity dispersion in rocks: *Geophysics*, **56**, 1940–1949.

- Mavko, G., and A. Nur, 1975, Melt squirt in the aesthenosphere: *Journal of Geophysical Research*, **80**, 1444–1448.
- Müller, T. M., and B. Gurevich, 2004, One-dimensional random patchy saturation model for velocity and attenuation in porous rocks: *Geophysics*, **69**, 1166-1172.
- Müller, T. M., B. Gurevich, and M. Lebedev, 2010, Seismic wave attenuation and dispersion resulting from wave-induced flow in porous rocks-A review, *Geophysics*, **75**, 147-164.
- O’Connell, R. J., and B. Budiansky, 1974, Seismic velocities in dry and saturated cracked solids: *Journal of Geophysical Research*, **79**, 5412–5426.
- , 1977, Viscoelastic properties of fluid-saturated cracked solids: *Journal of Geophysical Research*, **82**, 5719–5740.
- Plona, T., 1979, Observation of a second bulk compressional wave in a porous medium at ultrasonic frequencies, *Applied Physics Letters*, **36**(4), 259-261.
- Pride, S. R., and J. G. Berryman, 2003a, Linear dynamics of double-porosity and dual-permeability materials. I. Governing equations and acoustic attenuation: *Physical Review E*, **68**, 036603.
- , 2003b, Linear dynamics of double-porosity and dual-permeability materials. II. Fluid transport equations: *Physical Review E*, **68**, 036604.
- Ren, H., G. Goloshubin, and F. J. Hilterman, 2009, Poroelastic analysis of amplitude-versus-frequency variations: *Geophysics*, **74**, 6, N41–N48.
- Spencer, J.W., 1981, Stress relaxations at low frequencies in fluid-saturated rocks: Attenuation and modulus dispersion: *Journal of Geophysical Research*, **86**, 1803–1812.
- Stewart, R. R., P.D. Huddleston, and T.K. Kan, 1984, Seismic versus sonic velocities: A vertical seismic profiling study, *Geophysics*, **49**, 1153-1168.
- Tang, X., 2011, A unified theory for elastic wave propagation through porous media containing cracks- An extension of Biot’s poroelastic wave theory: *Science China—Earth Sciences*, **54**, 1441– 1452.
- Thomas, D.H., 1978, Seismic application of sonic logs: *The Log Analyst*, **19**, 1.
- White, J. E., 1975, Computed seismic speeds and attenuation in rocks with partial gas saturation: *Geophysics*, **40**, 224–232.

Yamamoto, T., 2003, Imaging permeability structure within the highly permeable carbonate earth: inverse theory and experiment, *Geophysics*, **68**, 1189-1201.

2 DISPERSION AND ATTENUATION: HETEROGENEITY

2.1 Abstract

In this chapter, three fundamental questions about dispersion and attenuation are reviewed: (1) what are velocity dispersion and wave attenuation; (2) what is the relationship between fluid flow and dispersion and attenuation; and (3) what is the relationship between heterogeneity and induced dispersion/attenuation.

2.2 Dispersion and attenuation in sedimentary rocks

Seismic attenuation and dispersion have been observed and used to study the earth's subsurface structure for a long time. For example, global shear wave attenuation tomography has been used to invert the upper mantle temperature map (Bhattacharya, 1996). For the interest of petroleum industry, the attenuation and dispersion associated with the seismic wave-induced fluid flow (WIFF) draws particular attention because it contains the information about the rock and fluid properties (Müller *et al.*, 2010).

Although the proposed work here will focus on the WIFF related attenuation and dispersion, it is important to understand that there are other mechanisms not covered in this work which may cause the wave energy dissipation. Those include the elastic ones like interface energy partitioning, geometrical spreading, multipath focusing and defocusing, and scattering, and anelastic ones like large scale intrinsic friction, small scale defects migration, grain boundary sliding, and vibration of dislocation.

As the most general definition, any amplitude decay of the wave front during its propagation can be viewed as attenuation. It may or may not be associated with velocity dispersion, depending on the physical mechanism causing the amplitude decay.

2.2.1 **Non-intrinsic attenuation**

Exploration seismic wave comes from one or more point sources. In a homogeneous isotropic medium, it propagates with a spherical wave front. As a rule of energy conservation, the wave front amplitude decays proportionally to the square of the distance traveled. This is called spherical spreading and must be considered in near surface seismic data processing. At far field, it can be approximated as plane wave. At stratigraphic interfaces, the seismic wave splits into transmission and reflection waves so that the energy in the incident wave partitions to multiple outgoing waves. The amplitude relationship between reflection, transmission, and incident waves at a planar interface obeys Zoeppritz equation (Aki and Richard, 1980). In a more general case, if the rock properties gradually change, the seismic wave will travel in a curve, causing focusing or defocusing according to the geometry. The interference among different ray traces will also alter the amplitude.

In the above cases, although the amplitude of the wave front may decrease (sometime it increases, like in focusing), there is no mechanical energy loss into heat. All the energies remain in mechanical form, but are just converted into other waves. These are called non-intrinsic attenuation.

2.2.2 Intrinsic attenuation

In most of the real subsurface situations, the seismic wave propagates in a medium that is not completely elastic. The stress and strain relationship in such a medium does not obey the simple Hooke's law which only considers the effect of springs. Instead, it can be generally viewed as a spring-dashpot system. The spring and dashpot can be configured in a series Maxwell model, a parallel Kelvin-Voigt model, or a combination of both models into a complicated network (Figure 2.1).

The existence of the dashpot has two effects. First, the movement of the piston inside the dashpot will cause the frictional energy loss into heat. This is the root cause of the wave attenuation in the so-called viscoelastic material. Second, the stress exerted on the dashpot part of the medium is not proportional to the strain, but rather the rate of strain (Holmes, 2009). In other words, the apparent stiffness of a dashpot depends on how fast it is deformed. This is the root cause of the modulus (or velocity) dispersion in viscoelastic material. If the material is linear, the causality in a physical system requires the modulus dispersion should be related to the attenuation with Kramers-Kronig equation (Toll, 1956), which basically says a larger attenuation is always associate with a larger dispersion, and zero attenuation requires no dispersion.

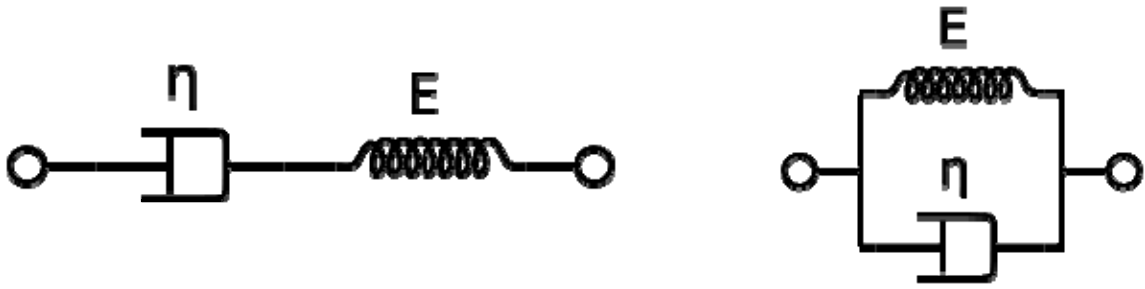


Figure 2.1 Schematic representations of Maxwell model (left) and Kelvin–Voigt model (right), for a viscoelastic material.

What can cause the dashpot-like behavior in sedimentary rocks? Early researchers believed the sliding between the grain surfaces is the main contributor to energy loss when the seismic wave passing through. Later studies showed that except for the cases in shallow weathering zone, the seismic strain amplitude in typical exploration depth is in range of 10^{-6} or below. With such small amplitude, it is less likely for grains to slide to each other. Therefore, the friction at grain boundary, due to sliding, should not be considered as the main source of attenuation and dispersion in sedimentary rocks (Winkler and Nur, 1982).

Biot, in his series of papers (1956a, 1956b, 1962) discussed that the relative movement between the fluid and solid frame in a porous medium can constitute the dashpot and thus cause the viscoelastic behavior. This opened a new era to dispersion and attenuation study, and many researchers followed the path to develop various theories and models to account for the observed dispersion and attenuation in sedimentary rocks in terms of different types of wave-induced fluid flow (WIFF).

To fully understand the frequency dependent fluid effect in porous media, it is better to first review the frequency independent fluid effect, where the fluid is not allowed to move relative to its host frame.

2.3 Fluid effect in homogeneous porous media: undrained deformation

When an external stress is applied to a porous medium with its pore filled with fluid, the deformation of the pore space compresses the fluid and changes the pressure of the pore fluid. Compared with the case that pore is empty, this additional pore pressure will provide an extra support to the frame and therefore reduce the total strain. The classical Gassmann equation (Gassmann, 1951) fully quantifies the amount of the fluid effect in a homogeneous porous medium, in terms of the grain modulus K_0 , frame dry modulus K_{dry} , porosity ϕ , and fluid modulus K_f .

$$K_{sat} = K_{dry} + \frac{\alpha^2}{(\alpha - \phi) / K_0 + \phi / K_f} \quad (2.1)$$

Here α is the Biot coefficient and $\alpha = 1 - K_{dry} / K_0$.

The term “homogeneous” here means within a representative element volume (REV), one can use a single value for each of those four parameters. There is another assumption to assure the validity of the Gassmann relation: the pore fluid has to be completely confined in the pore space (closed boundary). This is particularly important in the present study, since it can be shown here that by carefully selecting a proper size of the REV, it is almost always possible to satisfy the homogeneous condition, but not possible to satisfy the closed boundary condition simultaneously. Furthermore, by

exploring the fluid effect under non-closed boundary conditions, a new approach will be introduced to characterize the frequency dependency of the fluid effect.

Berryman (1999) in his tutorial for Gassmann's equation presented a concise and elegant way to derive the Gassmann relationship, in which the closed boundary condition is explicitly included in the formulation. Pride's and Berryman's later theory (*e.g.*, Pride and Berryman, 2003a, 2003b) on double-porosity dual-permeability model can be viewed as a logical extension from this set of formulas, just by allowing the boundary open to the surrounding material.

Before I start to discuss the fluid related dispersion and attenuation in inhomogeneous rocks, it is worthwhile to first review how dispersion and attenuation can occur even in a completely homogeneous porous media.

Biot is the first person who realized that in a fluid-filled porous media, the fluid and solid frame can have a relative movement under a time varying stress field. And if the fluid has viscosity (which is almost always true in real world), some parts of the strain energy will dissipate into heat and cause wave attenuation as well as velocity dispersion.

There is a common perspective that Biot's theory only describes the global flow in homogeneous porous media. This global flow is caused by the pressure gradient naturally existing in a plane wave. However, the value of Biot's theory is much more than that. Actually global flow dispersion and attenuation is just one example Biot

presented in the case of a passing plane wave in porous medium, in order to demonstrate that an analytical solution can be obtained when the applied external stress is analytically given. The most important contribution of Biot's work is that he pointed out the relative movement between the fluid and frame is the ultimate cause of the mechanical energy dissipation into heat. Biot has published his theories in a series of papers, with different notations and different ways to derive and formulate the equations. But his 1962 paper on *Journal of Applied Physics* (Biot, 1962) contains most complete and comprehensive material for his whole theory. In this paper he presented a much general frame work which is not dependent on any specific type of fluid flow.

Compared with non-porous solid, a porous medium just adds one more state variable: fluid increment, to the strain, and one more field variable: pore pressure, to the stress. So the generalized stress strain relationship has two more components. Biot (1962) obtained this relationship using a standard strain energy analysis. He assumed the fluid increment is a known or measurable variable. Until this point, there is no association with dispersion and attenuation. This concept can be applied to static case, where everything is in equilibrium.

If the field variable has a disturbance away from the equilibrium, like in the case of passing seismic wave, it is necessary to consider the viscoelasticity. Because any non-equilibrium state will, by nature, relax to the equilibrium state, which is a dynamic process. The frequency dependency of the relaxation process is determined by the internal resistance (like the friction force) against the relaxation. If the resistance is smaller, it takes shorter time to reach the equilibrium; and if the resistance is larger, it

takes longer to reach the equilibrium. No matter what the specific cause and mechanism of the relaxation process is, such system can always be mathematically equivalent to a spring-dashpot system, and can be formulated using the viscoelastic model.

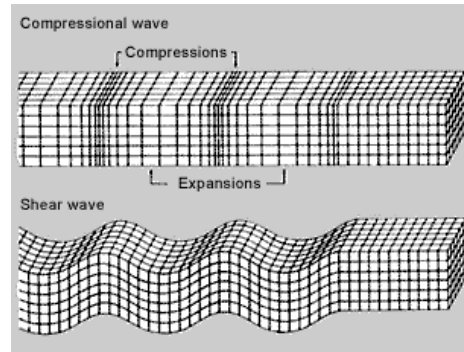
In discussing the relationship between viscoelasticity and elasticity, Biot (1962) introduced the concept of “correspondence principle”. In viscoelasticity, the stress strain relationship still retains the same format as in elasticity. However all the elastic coefficients are replaced by a set of operators that are complex numbers. Not only the one associated with fluid flow, but all the coefficients can be viscoelastic. Biot actually mentioned several possible relaxation mechanisms besides fluid flow, including crystal dissolution and precipitation, thermal diffusion, and pure fluid viscoelasticity. From this, one can see that Biot had attempted to understand and describe the viscoelastic behavior in porous media from a very wide angle, at least qualitatively. Of course, the focus of the rest of the paper is to quantitatively characterize one such relaxation mechanism, which is fluid pressure equilibration. But it hasn’t been discussed how this pressure gradient is generated. From later studies (White, 1975; O’Connell and Budiansky, 1974, 1977; Pride and Berryman, 2003a, 2003b), people eventually got to know there are several ways to generate the fluid pressure gradient in porous medium:

1. Pore pressure increment is caused by the deformation of pore space by external stress. If the exerted stress is not spatially uniform, then the induced pore pressure will follow the pattern of the applied stress field with a spatial gradient. In the case of passing seismic wave, the peak and trough within a wavelength exhibits a sinusoidal stress distribution.

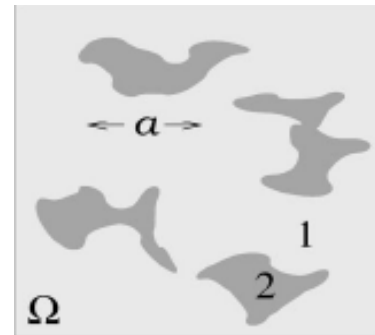
Therefore, the induced pore pressure also has such a continuous sinusoidal gradient along the wavelength, with approximately the same initial phase as applied external stress.

2. In a scale much smaller than the seismic wavelength, the pore pressure gradient mentioned above is sufficiently small and can be ignored most of the time. However, the compressibility of the pore space in general is not spatially uniform. Those more compliant pores will induce larger pore pressure increment compared with those less compliant pores. This is another cause of the pore pressure gradient, which is heavily related to the rock heterogeneity.
3. If there are multiple phases of immiscible fluids with different compressibility in the pore space, an applied stress will induce different pressures in different fluid phases. This is the third type of pore pressure gradient, which is independent of rock heterogeneity.

Heterogeneity in applied stress



Heterogeneity in rock frame



Heterogeneity in pore fluid

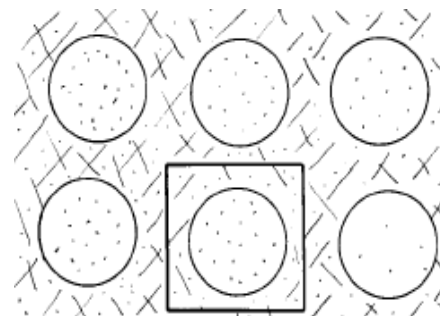


Figure 2.2 Three different types of mechanisms to cause pore pressure gradient in porous medium.

Figure 2.2 outlines the three major types of the pore fluid pressure gradient causes, whose mechanisms will be discussed in more detail later. The main point here is that in Biot's theory it is assumed there is a pore fluid flow driven by certain pressure gradient, without explicitly giving which mechanism causes such gradient. Therefore it is obviously underestimating the value of Biot's theory if viewing it only as a "global flow" model.

In order to formulate the velocity dispersion and wave attenuation, it is necessary to give an analytical expression of the stress field, then obtain the expression of the fluid increment term as function of the stress (in complex form). This was first accomplished by Biot (1956a), where he selected the first type of gradient generation mechanism to demonstrate how to obtain the final dispersion and attenuation expressions. The reasons for his selection could be: first, the plane wave stress field has been well studied and defined analytically; and second, this type of pore pressure gradient has nothing to do with either rock frame heterogeneity or fluid heterogeneity; thus requiring fewer input parameters than the other two types of mechanisms. It is mathematically less complicated and serves as a good starting point to apply his general theory to one particular problem.

From this point of view, the later proposed models dealing with the other two types of pressure gradient generation mechanisms are just specific applications of the general Biot theory. Because they involve the heterogeneities on rock or fluid and additional input parameters, like pore aspect ratio or bubble size, have to be brought in, to obtain the final analytical solutions.

One of the most eye-opening predictions of Biot's theory is the existence of two P-waves in fluid-filled porous media. The prediction of the slow P-wave is experimentally proven in a synthetic rock sample by Plona (1979) and real sandstone by Kelder and Smeulders (1997). These observations greatly promoted the Biot's theory and stimulated developments of new models based on this theory. However, there is a widespread misunderstanding regarding the relationship between slow and fast P-waves, in

which people believe that slow P-wave causes the attenuation of fast P-wave. It is very worthwhile to clarify this issue because it helps towards understanding the fundamentals of Biot's theory as a whole.

As previously mentioned, a viscoelastic material can always be modeled as consisting of springs and dashpots, with various configurations. The spring accounts for the elastic deformation since the stress and strain relationship follows Hooke's law. The dashpot accounts for the viscous deformation, in which the stress is proportional to the first time derivative of the strain (strain rate). For a porous media filled with fluid, the solid frame or skeleton is treated as elastic springs. If the fluid is viewed as non-viscous, then it is also elastic, although with the different elastic constants compared with the skeleton. The whole system can be considered as a network of two types of mass points, connected by two types of springs, one stiffer and one softer (the softer one has another character that it cannot hold any shear stress).

This scenario can be easily analogous to the classic phononic lattice theory (*e.g.*, Donovan and Angress, 1971). In this theory, a phonon is a collective excitation in a periodic, elastic arrangement of atoms or molecules in condensed matters, such as solids and some liquids. Solids with more than one type of atoms, either with different masses or bonding strengths, exhibit two types of phonons: acoustic phonons and optical phonons

Acoustic phonons are coherent movements of atoms of the lattice out of their equilibrium positions. If the displacement is in the direction of propagation, then the atoms will be closer in some areas, and further apart in others, as in a sound wave in the air (hence the name “acoustic”). Optical phonons are out of phase movement of the atoms in the lattice, one atom moving to the left, and its neighbor to the right. This occurs if the lattice is made of atoms of different charge or mass. Under the external excitation from the boundary of the lattice crystal, both phonon modes have to be excited to satisfy the boundary condition. Figure 2.3 depicts the movements of atoms for both modes in a lattice.

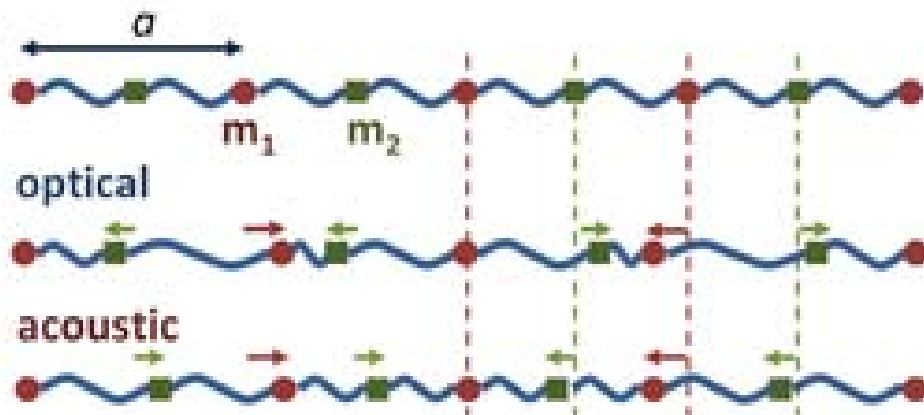


Figure 2.3 Optical and acoustic vibrations in a linear diatomic chain.

A porous medium filled with fluid is just like such a lattice. The solid frame normally has larger density and greater modulus (spring constant). When a traveling P-wave enters the medium, to satisfy the boundary conditions at the interface, it is obvious that this system has two longitudinal wave modes under cycling stress. Both modes are coupled between the stiffer and softer springs, but in one mode two types of springs deform in the same phase (both are compressed or stretched) thus causing a large

wavelength and velocity; and, in another mode, two springs deform in opposite phases (one compressed and one stretched) thus causing a short wavelength and small velocity. This is exactly what Biot's theory (Biot 1956a) has predicted in section 5 of his 1956 paper. One should notice that both wave modes are not dispersive and attenuative since there is no energy dissipation mechanism involved. The existence of the slow P-wave (optical mode phonon) does not cause the attenuation of the fast P-wave (acoustic mode phonon). Both of them are pure elastic waves, without any dispersion and attenuation. The partitioning of the wave energy into two P-waves only happens at the boundary of the porous media, in a similar way like wave reflection and transmission at impedance boundary. In that later case, to satisfy the boundary conditions (continuity of stress, strain, and displacement), an incident P-wave can be partitioned into several reflected and transmitted P and S-waves, as described by Zoeppritz equations (Aki and Richard, 1980).

Only when the fluid is viscous, and the pore spaces are connected and permeable, that the relative movement between the solid and fluid can cause a friction energy loss, just as a dashpot system. The total stress and strain are no longer in linear relationship. In the wave equation, there is a first-order time derivative term. Therefore in the solution, the wave number k is a complex number, and not linear to angular frequency. This means the amplitude is attenuative and the velocity is dispersive.

It is in section 6 of Biot 1956 paper (Biot, 1956a), that the global flow dispersion and attenuation formulation was introduced. Here Biot related the stress-strain

relationship to Darcy's law. And in section 7, he used plane wave to give a numerical example of the dispersion and attenuation in a so called global flow situation.

From the above discussion, one can conclude that attenuation of the fast P-wave is not caused by the slow P-wave stealing its energy. They are, in fact, two separate phenomena. The existence of two P-waves is resulting from the double-mass-spring nature of the fluid filled porous medium. It is completely within the elastic scheme and has nothing to do with dispersion and attenuation. The dispersion and attenuation are caused by the frictional energy loss due to relative movement between the viscous fluid and host porous frame. Both fast and slow P-waves have their own dispersion and attenuation features. As demonstrated in section 7 in Biot (1956a), the fast P-wave is slightly dispersive and attenuative, but the slow P-wave is significantly dispersive with huge attenuation. Here is an intuitive explanation of such a difference. In the fast P-wave, the solid and fluid move in the same phase; thus the relative movement between them is small. But in the slow P-wave, they move in the opposite phase; therefore exhibiting a large relative movement resulting in significant frictional energy loss, with huge dispersion and attenuation. Typically, the slow P-wave will damp out in couple of cycles, thus being very difficult to be observed (Plona, 1979).

2.4 Fluid effect in inhomogeneous porous media

In the last section, through the detailed review of Biot's theory, it is clarified that the frictional energy loss between the viscous fluid and host rock frame is the root cause of the WIFF associated dispersion and attenuation in sedimentary rocks. Logically, the

next step is to study what can cause the relative movement of the pore fluid. Biot solved one simple case in homogeneous rocks, where the pressure gradient comes from the sinusoid stress distribution of the traveling plane seismic wave.

But for real sedimentary rocks, in most cases, the homogeneous conditions are not even approximately satisfied. As discussed previously, a confining pressure increment from the passing seismic wave will generate a pore pressure increment through the pore deformation. This pore pressure increment provides the additional support to the frame and increases the total stiffness of the porous media. The ratio of the pore pressure increment to confining increment is a function of K_0 , K_{dry} , K_f , and ϕ (Skempton, 1954; Thomsen, 1985):

$$\frac{\Delta P_p}{\Delta P_c} = \frac{\alpha K_f}{K_{dry} [\phi + \frac{K_f}{K_0} (\alpha - \phi)] + \alpha^2 K_f} \quad (2.2)$$

Figure 2.4 plots the ratio of pore pressure increment to confining pressure increment (Skempton coefficient) against the dry frame modulus. Different curves in the plot represent the effect of the pore fluid modulus and this plot can be used to analyze two types of heterogeneities.

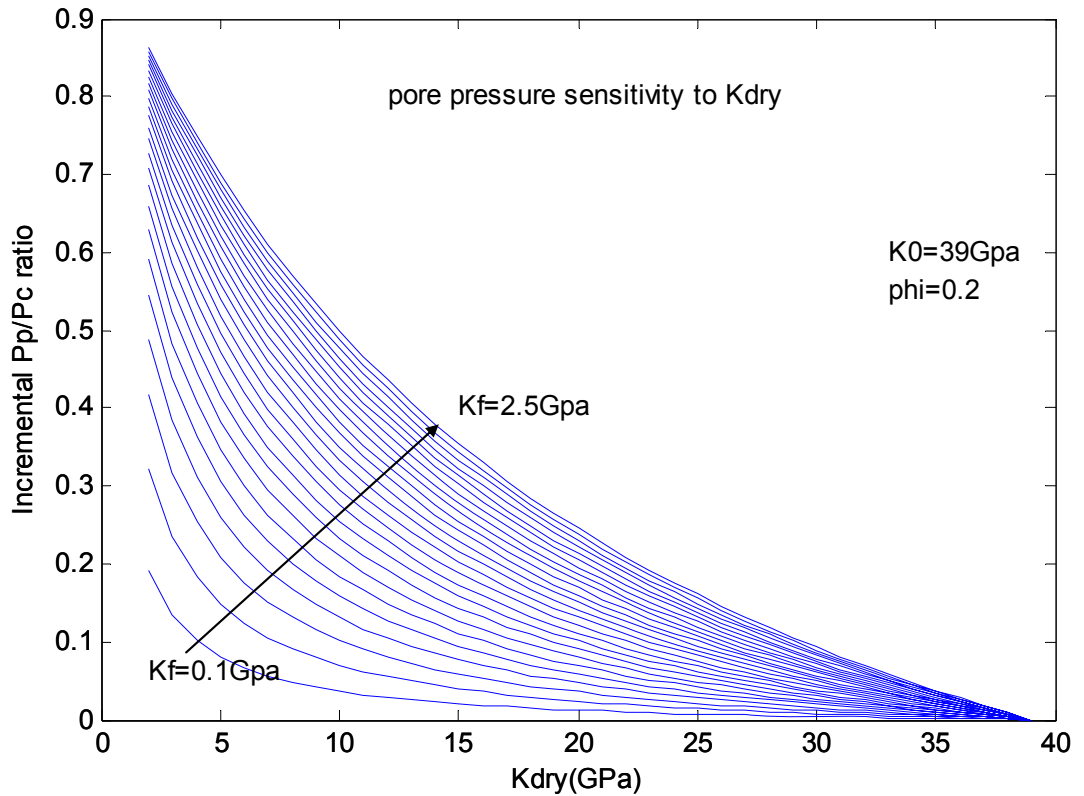


Figure 2.4 Pore pressure increment depends on both dry frame bulk modulus and pore fluid modulus.

We can first consider that the rock frame is homogeneous. The pore pressure will have a much larger increment in stiffer fluids, like brine or oil, than in softer fluid, like gas. If two of such fluids are neighboring to each other, the pressure difference between them will drive the phase boundary to move towards the low pressure side. This is exactly what White's gas pocket model (White, 1975) and partial saturation model (Dutta and Od, 1979a, b) described.

Next, we consider the fluid saturation as homogeneous. Along each curve in the plot, the pore pressure increment varies with the dry frame modulus. The natural deposition and diagenesis of sedimentary rocks are complicated processes. The frame modulus can have spatial variations in different scales for many reasons. In the macro scale, the boundary between strata imposes large contrasts on most of the physical properties of the rock, including the dry modulus. In the micro scale, a thin crack and an equant pore may have a large difference on their local compressibility. In the mesoscopic scale, variations on original mineral compositions, compaction stress distributions, cementations and precipitations, and many other factors can result in the spatial heterogeneity of rock frame elastic properties. When compressed by a passing seismic wave, each of those heterogeneities will convert to a gradient on induced pore pressure increment.

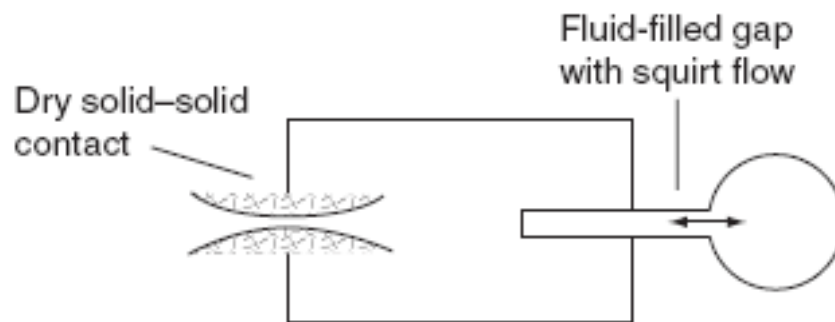


Figure 2.5 Schematic of a micromechanical model to describe the squirt-flow mechanism (after Mavko *et al.*, 2009).

The micro scale (i.e., in the size of grain or pore) type of heterogeneity was early recognized by O’Connell and Budiansky (1974, 1977), and Mavko and Nur (1975). The name “squirt flow” is commonly used to represent the fluid squeezed from the thin cracks

into neighboring round pore spaces. Figure 2.5 shows the schematic illustration of a micromechanical model to describe the squirt-flow mechanism (after Mavko *et al.*, 2009). The study on the squirt flow attenuation is continued by many investigators to interpret the inelastic properties in fractured or cracked porous media (Mavko and Jizba, 1991, 1994; Dvorkin *et al.*, 1995; Le Ravalec and Gueguen, 1996; Gurevich *et al.*, 1997; Chapman, 2002; Lambert *et al.*, 2006; Gurevich *et al.*, 2009; Tang, 2011). The most important contribution of the squirt flow mechanism to the attenuation and dispersion theories is that it explicitly established the bridge between the rock frame heterogeneity and the seismic wave attenuation and velocity dispersion. Here in this case the heterogeneity is just from the geometry of the pore space. Based on early classical poroelasticity studies (Skempton, 1954; Walsh, 1965; Hudson, 1984) the pore pressure gradient induced by compressional seismic wave is solved as a function of certain heterogeneity parameters, like pore aspect ratio, crack density and porosity. The diffusion and pore pressure equilibration process is then solved to obtain the energy dissipation and modulus or velocity dispersion relationship. Due to its small heterogeneity scale and short diffusion time, it was widely believed that squirt flow attenuation and dispersion mainly occur at a relatively higher frequency range (i.e., well-log and ultrasonic) and does not have a significant effect in seismic frequency range. However, the recent unconventional hydrocarbon exploration has challenged this perspective from two aspects. Batzle *et al.*, (2006) suggested the characteristic frequency of a local diffusion process is controlled by a parameter called fluid mobility:

$$M = \frac{\kappa}{\eta} \quad (2.3)$$

Fluid mobility M is defined as the ratio of permeability κ and fluid viscosity η . It represents how easy or difficult the fluid can flow between the pores. If the mobility is large, it takes little time for the pore pressure to be equilibrated thus the characteristic frequency is high; and vice versa. Strictly speaking, to deal with the pore or grain scale heterogeneity and diffusion process, the macro-parameter permeability is normally not applicable. A more pore geometry specific parameter like fluid conductivity (Tang and Cheng, 1989) might be needed to replace the permeability. But nevertheless they are both the frame properties to represent how well the pore space is connected. The viscosity is the fluid property independent to the frame. From equation 2.3 it can be seen that mathematically the fluid mobility can be small enough to take the characteristic frequency into seismic range, if the permeability (or fluid conductivity) is very low, or the fluid viscosity is very high. The latter case becomes applicable in heavy oil reservoirs, where the heavy oil has a viscosity several orders greater than conventional pore fluids like brine, oil, or gas (Das, 2010). On the other hand, the exploration in tight gas sandstone has experienced very low permeability in microDarcy range. More recently, in shale gas reservoirs, the permeability can even goes to nanoDarcy range. Cracks and fractures play important roles in the properties of both tight gas sandstone and shale gas reservoirs. Along with other intergranular pores or micropores, they constitute the necessary heterogeneities in pore compressibility, and are very good candidates for the squirt flow attenuation and dispersion. With such low permeability or fluid conductivity, even if the heterogeneity size is very small, the resulting relaxation time may still be long enough to drive the characteristic frequency into seismic range. Therefore it can be

essential to include the attenuation and dispersion analysis into the seismic processing and interpretation of those types of reservoirs.

Although the low fluid mobility helps to explain why the dispersion and attenuation can be observed in seismic frequency in certain types of tight formation reservoirs, in general, the question why the dispersion and attenuation occur in a much wider frequency band than predicted by the squirt flow models has not been satisfactorily answered until the mesoscopic heterogeneity and corresponding fluid flow was introduced.

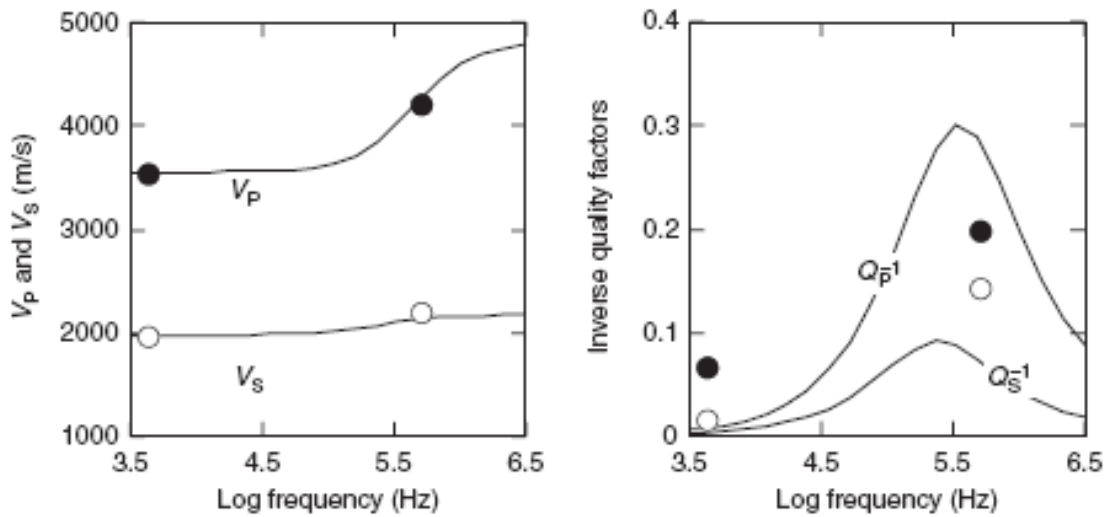


Figure 2.6 A typical velocity dispersion or wave attenuation curve spans about two orders of magnitude in frequency (after Mavko *et al.*, 2009).

The typical frequency dependence of velocity and attenuation is shown in Figure 2.6 as a Debye peak with a width of 10^2 - 10^3 . However, a wide comparison among the seismic, well-log, and ultrasonic data suggests that the dispersion and

attenuation in real rocks may span over a much wide range than that (Sams *et al.*, 1997). Adam *et al.*, (2009) also reported continuous dispersions from seismic (several Hz) to ultrasonic (MHz) range in both sandstones and carbonate rocks saturated with various fluids. In Figure 2.7, the measured data on a tight gas sandstone show that the dispersion spreads from Hz to MHz frequency range for fluid saturated sample.

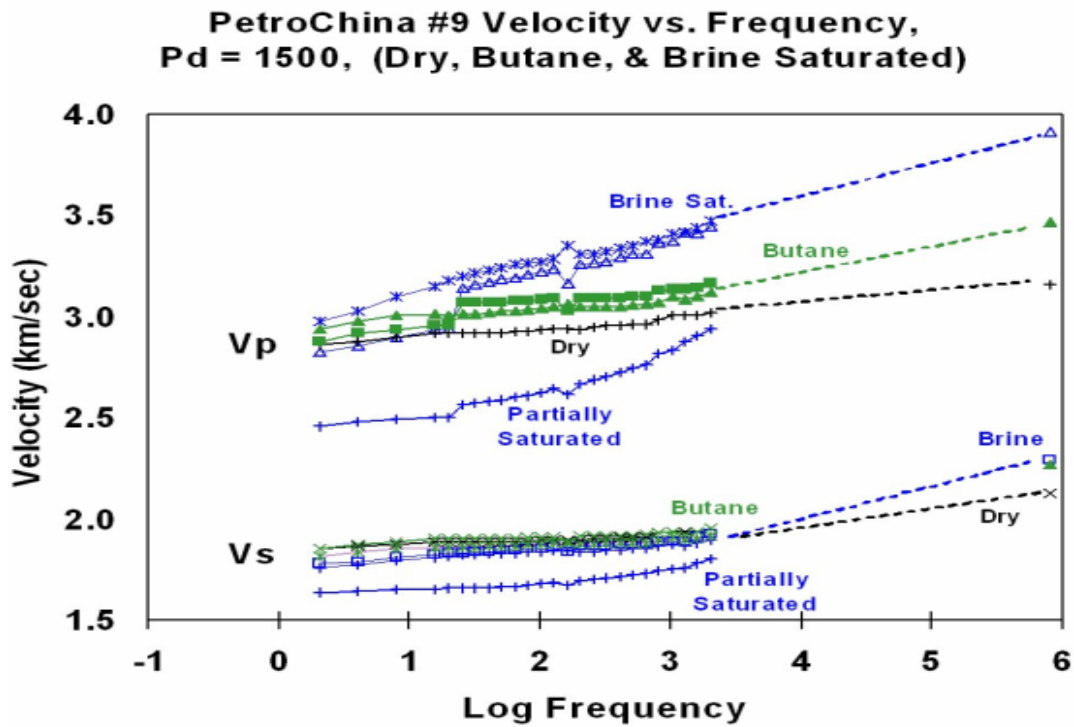


Figure 2.7 Measured data on tight gas sandstone show that the dispersion spreads from Hz to MHz frequency range for fluid saturated sample (Measured by Batzle, unpublished).

Liu *et al.*, (1976) first theoretically addressed this behavior. They used a phenomenological viscoelastic model rather than poroelastic theory to describe the effective relaxation behavior of porous media as a stand linear solid. Two important parameters: stress relaxation time and strain relaxation time fully mathematically model the attenuation and dispersion curves. Each pair of relaxation times represents

a particular relaxation mechanism and gives a Debye peak in attenuation $1/Q$ spectra. Liu *et al.* argued that there are multiple relaxation mechanisms coexisting in the rock. By selecting a set of twelve relaxation times, they literally generated an almost constant $1/Q$ spectrum and a wide velocity dispersion curve in a 10^5 frequency range (Figure 2.8).

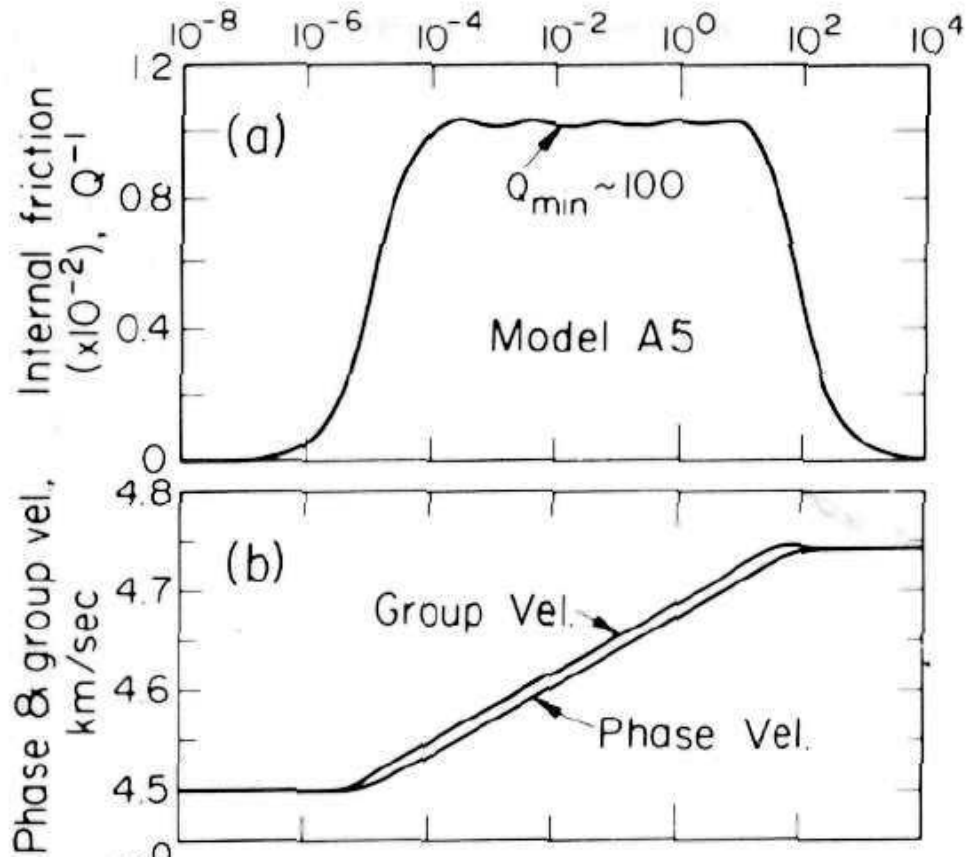


Figure 2.8 Superposition of 12 pairs of relaxation times with a standard linear solid model gives a near constant Q and wide dispersion band (Liu *et al.*, 1976).

Many authors, like White (1975), O'Connell and Budiansky (1977), have mentioned in their papers that a distribution of the controlling parameters can blur out the dispersion band and attenuation peak. But people continue to use simple effective

parameters in practical applications, until recently. Müller *et al.*, (2007) used a concept of dynamic permeability to numerically demonstrate the broadening of dispersion curve and $1/Q$ spectrum. Han and Yao (2009) used capillary pressure data to model the distribution of fluid mobility to obtain a wide dispersion curve matching the measured data.

The wide spreading of the dispersion and attenuation is better addressed by the concept of mesoscopic heterogeneity and corresponding fluid flow. Berryman and Wang (2001) first introduced the idea of double-porosity to represent the large contrast on the pore compressibility between a background porous medium and large fractures. It is distinguished with squirt flow model that the fractures here are much larger than the pore or grain size, but much smaller than the wavelength. This concept was further developed into a double-porosity and dual-permeability model (Pride and Berryman, 2003a, b) to generally characterize the spatial variation of either rock frame or fluid compressibility in such a scale, the so-called mesoscopic heterogeneity. This expansion is non-trivial. First, the fluid mobility includes two factors, permeability and viscosity, to account for the spreading of relaxation time. This model adds one more dimension: length of diffusion, to further expand the possible range of relaxation time. This new dimension of variation reflects an important natural geological feature which shouldn't be neglected. Second, this new model is a generalization of the previous models on heterogeneities. Recalling the three types of pore pressure gradient generation mechanisms discussed before, if the first type, from

applied stress variation, can be viewed as external heterogeneity, then the other two types can be viewed both as internal heterogeneities. In Pride *et al.*, (2004), they demonstrated that both the fluid heterogeneity (White model) and rock frame heterogeneity (squirt flow model) can be contained into this general framework. With such a generalization, the relationship between the heterogeneity and fluid flow related attenuation and dispersion becomes much clearer, enabling people to develop better interpretations to the observations. Our work of the dynamic fluid modulus, which will be presented in chapter 3, is also heavily stimulated by the ideas and reasoning in double-porosity and dual-permeability model.

Due to the historical significance of this model, and its specific impact on the development of our work, I will perform a somewhat detailed and critical review on the paper by Pride *et al.* (2004). The emphasis will be placed on how they handle the relationship between heterogeneity and induced dispersion/attenuation.

2.5 Comments on Pride and Berryman's double-porosity model (2004 JGR)

The more detailed mathematical derivations of “double-porosity dual-permeability” model are presented in Pride and Berryman (2003a, b). In Pride *et al.* (2004), the physical and geological meaning of the model is discussed more clearly. The applications of this model to three attenuation mechanisms, which were thought independent previously, demonstrate it as a unified frame work. So my review and comments will focus on the 2004 paper. Their original equation numbers will be quoted

in format (Eqn. xx), only meaningful in this section, and should not be confused with the general equation numbers in the chapter.

The overall approach in the DPDP model is to find an equivalent homogeneous porous medium (single porosity Biot medium) to replace the heterogeneous composite material, so that this final effective medium can be simply handled with formulas of Biot's theory. In order to achieve this, some of the originally static (non-frequency dependent) properties of the Biot medium have to become dynamic (frequency dependent), in order to account for the effect of fluid flow due to heterogeneities. The composite material in the paper consists of two phases, each with its own porosity, permeability, and other elastic properties. The only thing they share is the same fluid. The reason to choose two phases is just for mathematical simplicity so that an analytical expression can be obtained. It shouldn't prevent one from considering the real rock as a composite of multiple phases, either in a discrete manner or continuous distribution spectrum.

The first step is to select an appropriate representative element volume (REV). It is selected large enough to statistically contain both phases, but small enough compared to wavelength. Within the REV, each phase LOCALLY (in a scale much smaller than the REV, or say within a sub-REV) completely obeys the Biot's theory (Eqn 1-4). It contains a flow (in or out) term. By taking space average over the REV, Pride *et al.* obtain Eqn. 6-10. There are three (compared one in Eqn. 1-4) flow terms, two for the fluid exchange on REV surface for each phase, and one for the internal fluid exchange between the two

phases. The authors called them macroscopic equations, but it may be more appropriate to call them mesoscopic equations, since they represent the behavior of the mesoscopic REV and they contain the internal flow term which is only meaningful in mesoscopic scale. The name of “macroscopic equations” should be reserved to the “effective single porosity Biot equations” reduced from Eqn. 6-10, which are in the same format of Eqn. 1-4, but with effective poroelastic moduli (Eqn. 11-13).

Next, the most important step in double-porosity model is to reduce the so-called mesoscopic equations (which still contain the internal fluid flow term) into the effective Biot theory. In the resultant effective Biot theory, there is now no internal flow term, and no two sets of elastic moduli for the two phases. Instead, it appears as a single porosity homogeneous medium, with one set of necessary elastic and inelastic moduli for the solid and fluid (Figure 2.9). The effect of the internal fluid flow is taken into account by those frequency dependent moduli. It is a matter of choice to select which moduli to be inelastic and which to be elastic. Pride *et al.* (2004) chose to keep the fluid modulus as elastic, and change almost all the bulk moduli of the solid part into inelastic. Those include dry bulk modulus, wet bulk modulus, and the Skempton coefficient. (Eqn. 11-13). This choice is fully legitimate mathematically as an effective medium approach. However, since one knows the frequency dependency of the moduli relies on the existence of pore fluid, it is against our physical intuition to allow the dry modulus also exhibiting a frequency dependency. In chapter 3, an alternative approach to Pride *et al.*'s approach will be introduced, in which the dry moduli will remain intact as a real static parameter, but the fluid modulus will be treated as a complex and dynamic parameter.

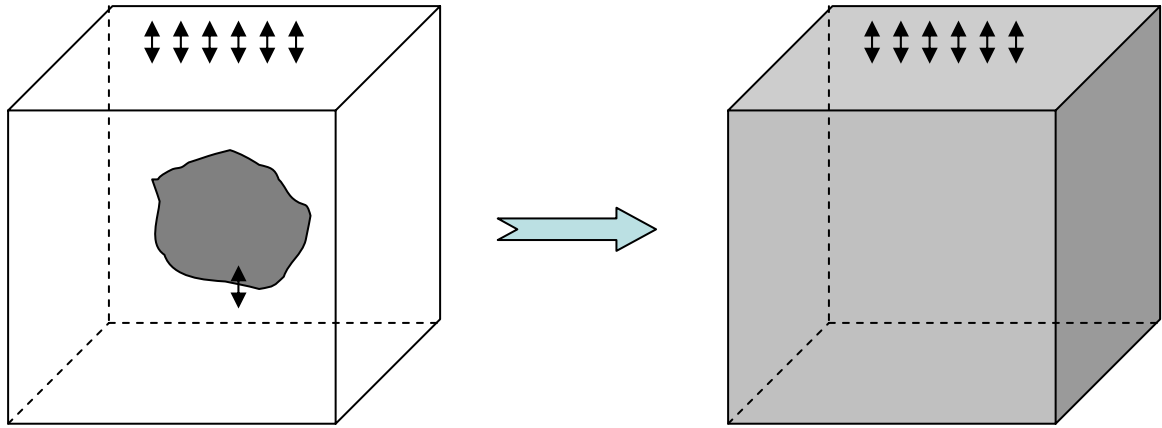


Figure 2.9 Reduction of a two-phase heterogeneous composite material with internal flow into an effective homogeneous single phase Biot medium. The effective Biot medium has no internal flow, but with certain frequency dependent moduli, to exhibit an overall viscoelastic behavior.

It is interesting and beneficial to look at how the frequency dependencies of those effective moduli are determined in Eqn. 11-13. First of all, there are six non-frequency dependent constants a_{ij} used to include the spatial average effect from two composites. Those are defined by Eqn. 14-20. The Hashin-Shtrikman low bound is chosen as the principle average scheme and discussed with meaningful geological scenarios.

The most important parameter in Eqn. 11-13 is internal transport coefficient γ . This is a frequency dependent parameter and contains all the information about the mesoscopic internal flow. From its definition in Eqn. 24, it can be seen that the maximum magnitude of the fluid flow is determined by γ_m (Eqn. 25), and the location of the attenuation peak and dispersion ramp is determined by a characteristic frequency ω_m (Eqn. 33).

$$\gamma(\omega) = \gamma_m \sqrt{1 - i \frac{\omega}{\omega_m}} \quad (\text{Eqn. 24 from Pride } et al., 2004)$$

Looking into the more details of Eqn. 25 and Eqn. 33 helps one understand the role of the heterogeneity geometry on the dispersion and attenuation in this theory. Common sense tells us that wave induced fluid flow is strongly dependent on the local heterogeneity geometry. Pride *et al.* claimed that this theory can model the wave induced flow for arbitrary mesoscopic geometry. This does not mean that the same formulations can be used to solve local flow dispersion for any geometry. Actually there are two important geometry parameters, LI and V/S appearing in Eqn. 25 and 33 respectively. They just appear here symbolically. The discussion on the meaning and calculation of those two parameters is somewhat conceptual. But from the examples on how they are estimated under certain specific geometry, one can see that the first parameter LI is basically a length parameter which is associated with the volume fraction of the two phases, and the second parameter V/S is a shape parameter which represents how the two phases are spatially arranged. Eqn. 25 only contains LI but not V/S . It means that to determine the maximum dispersion of a two phase composite material, one only needs to know the volume fraction of each phase and the property contrast between the two phases. Eqn. 33 explicitly contains V/S and also implicitly contains LI through γ_m . It implies that in order to fully characterize the dispersion and attenuation curve over the whole frequency range, additional detailed geometry information about how each phase is distributed in the space will be needed. These implications are very important to understand the relationship between heterogeneity and internal fluid flow relaxation.

These principles will then be used to develop our approaches to formulate the WIFF related dispersion and attenuation in heterogeneous rocks.

Besides the above geometry dependency, one should also notice that when applying this theory to other dispersion mechanisms than local frame compressibility (along with porosity and permeability) heterogeneity, like patchy saturation and squirt flow, it is necessary to use different set of a_{ij} constants. This is not geometry dependency, but can be viewed as even higher level “scenario dependence”.

It is also worthwhile to notice that the dependence on viscosity and permeability (or fluid mobility) appears at three places:

Eqn. 25: the amount of local flow, which affects the effective Biot poroelastic coefficient.

Eqn. 33: relaxation time of local flow, which determines characteristic frequency of the local flow attenuation and dispersion.

Eqn. 39: dynamic permeability of global flow. It has nothing to do with the local flow, but just affects the original dispersion and attenuation characters of global flow.

While the permeability in two phases has different values, it is always the less permeable phase dominating the fluid relaxation time and determining the attenuation and dispersion behavior of the composite material.

Although there are those two levels of dependencies as discussed above, one should still recognize and appreciate the generality of the double-porosity model. It provides a universal platform to treat various fluid relaxation caused dispersion and attenuation mechanisms.

Regarding the application, its limits still relies on how to accurately measure or properly model the basic rock parameters, like dry bulk modulus, porosity, permeability, tortuosity of each phase, and how to model the relative geometry relationship between two phases.

2.6 Localized compressibility determines dispersion and attenuation

The concepts and formulization presented here are not intended to replace any existing theory or models, but rather aim to use simple and minimum physical principles to demonstrate how the rock frame heterogeneity determines the dispersion through fluid relaxation.

In general, one can treat the heterogeneities in both double-porosity model and squirt flow model with a concept of localized frame compressibility. It is the different level of deformation of the pore space causing the different pore pressure change, which in turn determines the velocity dispersion and wave attenuation. Although the scale of the heterogeneities can be quite different in those two cases, but the governing physics are

not different from each other. To treat them within one framework can help to understand recently observed wide band continuous dispersion curve.

To characterize a dispersion behavior, one mainly needs to know two things: how much is the dispersion and at what frequency does the dispersion occur. The amount of dispersion is determined by the amount of compressibility difference and volume fraction between each component. The location of the dispersion slope is determined by the fluid connectivity and mobility between the phases.

Conceptually, if one is able to fully obtain the pore compressibility to the detailed level of each pore, then the Biot_Gassmann calculation can be performed to the same scale that each REV only include one pore, so that the pore pressure increment in each pore can be computed.

Given the fluid pressure heterogeneity and geometry, the relaxation process is governed by the diffusion.

Most existing models tend to use certain pore geometry parameters like aspect ratio and crack density to calculate the dispersion and attenuation. However, aspect ratio and crack density are both conceived parameters and only can be determined by inversion from measured velocities data. Non-uniqueness is a big problem and lack of direct confirmation from independent set of measured data is an even bigger challenge. To avoid the puzzle, one can use a localized K_{dry} to represent the acoustic

property of a frame-pore system. Consider a volume containing a representative pore as illustrated in Figure 2.10. Up until now, there isn't an effective way to obtain this K_{dry} . But the recent advancement on digital rock physics and FEM computation may provide a solution.

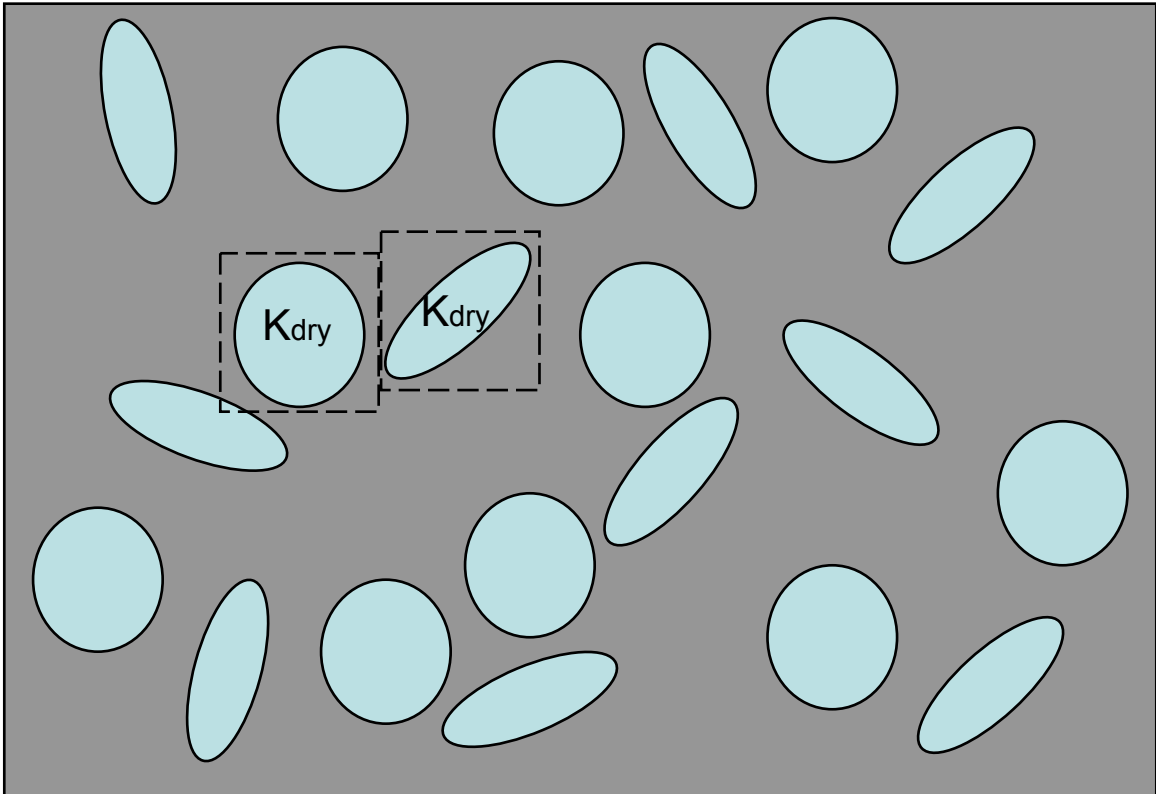


Figure 2.10 In local compressibility approach, consider a volume with a representative pore.

Figure 2.11 demonstrates the dispersion of bulk modulus between high and low frequency in a binary K_{dry} case, in which $K_{dry1}=16\text{GPa}$ with fixed porosity 0.1, and $K_{dry2}=1\text{GPa}$ with porosity varying from 0 to 0.1. In high frequency scenario (solid line), pore fluid is restricted in each pore and its support to every individual pore just follows Gassmann relationship (Gassmann, 1951) to give us K_{sat1} and K_{sat2} respectively. The bulk stiffness of the whole volume should come from certain spatial

average scheme. In this study the Voigt-Reuss-Hill (Hill, 1963) average was used. The resulting bulk modulus K_{sat_hf} represents the high frequency end value. In low frequency scenario (dashed line), the spatial average is first taken on the frame property to obtain K_{dry_lf} so that it behaves like a homogeneous porous media. As a consequence, the pore pressure increment within the representative volume is also homogeneous, and a single Gassmann fluid substitution can be applied to whole volume to get the K_{sat_lf} . This simple example demonstrate that to calculate the maximum dispersion between the low frequency and high frequency ends, one only need to know the volume fraction and local physical properties of each phase.

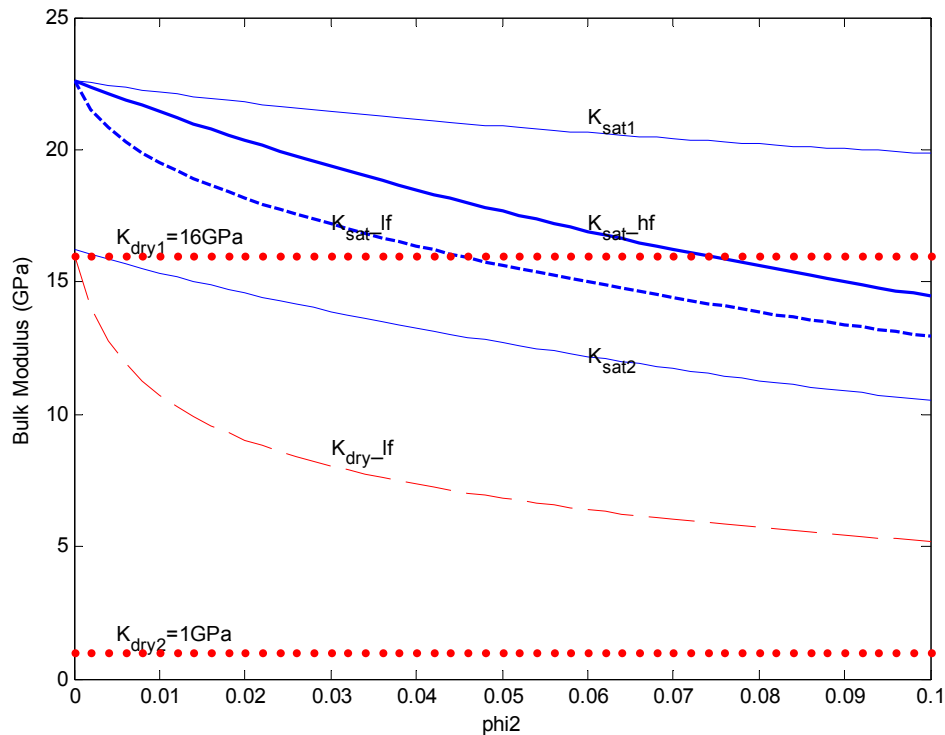


Figure 2.11 Modeled dispersion of bulk modulus, based on localized variation on frame dry bulk modulus. $K_0=39\text{GPa}$, $K_f=2.5\text{GPa}$, $K_{dry1}=16\text{GPa}$, $\phi_1=0.1$, $K_{dry2}=1\text{GPa}$.

For a frequency between these two scenarios, the pore pressure difference between different K_{dry} areas will be partially equilibrated through a diffusion process depending upon the time it is given. A small amount of fluid will flow from the softer pore into stiffer pore, since the pore pressure increment is always higher in softer pore than in stiffer pore. This makes both pores under partially drained condition, but the effect of the fluid support is reduced in softer pores but enhanced in stiffer pores. A proper spatial average scheme will show the final bulk stiffness below the original high frequency bound. If the pore geometry can be fully analytically formulated, then fluid dynamic equations can give exact solution for the dispersion. However, the complexity of the real sedimentary rock makes it impossible. A realistic approach may rely on the advanced finite element numerical simulation, based on high resolution image of the rock. This is possible due to the recent development on the high energy 3D scan technology (Zhang *et al.*, 2011; Derzhi *et al.*, 2010). We plan to explore the capability of this new methodology.

2.7 References

- Adam, L., M. L. Batzle, and K. T. Lewallen, 2009, Seismic wave attenuation in carbonates: *Journal of Geophysical Research*, **114**, B06208.
- Aki, K., and P.G. Richard, 1980, *Quantitative seismology: Theory and methods*: W.H. Freeman & Co.
- Batzle, M. L., D.H. Han, and R. Hofmann, 2006, Fluid mobility and frequency-dependent seismic velocity—Direct measurements: *Geophysics*, **71**, N1–N9.
- Berryman, J. G., 1999, Origin of Gassmann's equations, *Geophysics*, **64**, 1627-1629.
- Berryman, J.G., and H.F. Wang, 2001, Dispersion in poroelastic systems, *Phys. Rev. E* **64**, 011303

- Bhattacharyya, J. G., G. Masters, and P. Shearer (1996), Global lateral variations of shear attenuation in the upper mantle, *Journal of Geophysical Research*, **101**, 22,273–22,290.
- Biot, M. A., 1956a, Theory of propagation of elastic waves in fluid-saturated porous solid. I. Low-frequency range: *Journal of the Acoustical Society of America*, **28**, 168–178.
- , 1956b, Theory of propagation of elastic waves in a fluid-saturated porous solid. II. Higher frequency range: *Journal of the Acoustical Society of America*, **28**, 179–191.
- , 1962, Mechanics of deformation and acoustic propagation in porous media: *Journal of Applied Physics*, **33**, 1482–1498.
- Chapman, M., S. V. Zatsepin, and S. Crampin, 2002, Derivation of a microstructural poroelastic model: *Geophysical Journal International*, **151**, 427–451.
- Das, A., 2010, The viscoelastic properties of heavy-oil saturated rocks, PhD dissertation: Colorado School of Mines.
- Derzhi, N., J. Dvorkin, E. Diaz, C. Baldwin, Q. Fang, A. Sulayman, W. L. Soroka, A. Clark, T. A. Dayyni, and Z. Kalam, 2010, Comparison of traditional and digital rock physics techniques to determine the elastic core parameters in Cretaceous formations, Abu Dhabi, SPE-138586-PP
- Donovan, B., and J.F. Angress, 1971, *Lattice vibrations*: Chapman and Hall.
- Dvorkin, J., G. Mavko, and A. Nur, 1995, Squirt flow in fully saturated rocks: *Geophysics*, **60**, 97–107.
- Gassmann, F., 1951, Über die Elastizität poröser Medien: *Vierteljahrsschrift der Naturforschenden Gesellschaft in Zürich*, **96**, 1–23.
- Gurevich, B., M. Brajanovski, R. Galvin, T. M. Müller, and J. Toms-Stewart, 2009a, P-wave dispersion and attenuation in fractured and porous reservoirs— Poroelasticity approach: *Geophysical Prospecting*, **57**, 225–237.
- Gurevich, B., V. B. Zyrianov, and S. L. Lopatnikov, 1997, Seismic attenuation in finely layered porous rocks: Effects of fluid flow and scattering: *Geophysics*, **62**, 319–324.
- Han, D., Q. Yao, and M. Batzle, 2009, Intrinsic seismic wave attenuation - tight gas sand example: Fluid/DHI consortium annual report.
- Hill, R., 1963, Elastic properties of reinforced solids: Some theoretical principles: *Journal of Mechanics and Physics of Solids*, **11**, 357–72.

- Holmes, M. H., 2009, Introduction to the foundations of applied mathematics: Springer.
- Hudson, J. A., 1981, Wave speeds and attenuation of elastic waves in material containing cracks: *Geophysical Journal of the Royal Astronomical Society*, **64**, 133–150.
- Kelder, O., and D. M. J., Smeulders, 1997, Observation of the Biot slow wave in water-saturated Nivelsteiner sandstone, *Geophysics*, **62**, 1794-1796.
- Kjartansson, E., 1979, Constant Q — Wave propagation and attenuation: *Journal of Geophysical Research B*, **84**, 4737–4748.
- Lambert, G., B. Gurevich, and M. Brajanovski, 2006, Attenuation and dispersion of P-waves in porous rocks with planar fractures: Comparison of theory and numerical simulation: *Geophysics*, **71**, 3, N41–N45.
- Le Ravalec, M., and Y. Gueguen, 1996, High- and low-frequency elastic moduli for a saturated porous/cracked rock-Differential self-consistent and poroelastic theories. *Geophysics.*, **61**, 1080-1094.
- Liu, H.P., D.L. Anderson, and H. Kanamori, 1976. Velocity dispersion due to anelasticity: implications for seismology and mantle composition. *Geophysical Journal of the Royal Astronomical Society*, **47**, 41–58.
- Mavko, G., and D. Jizba, 1991, Estimating grain-scale fluid effects on velocity dispersion in rocks: *Geophysics*, **56**, 1940–1949.
- , 1994, The relation between seismic P- and S-wave velocity dispersion in saturated rocks: *Geophysics*, **59**, 87–92.
- Mavko, G., T. Mukerji, and J. Dvorkin, 2009, *The rock physics handbook*: Cambridge University Press.
- Müller, T. M., B. Gurevich, and M. Lebedev, 2010, Seismic wave attenuation and dispersion resulting from wave-induced flow in porous rocks-A review, *Geophysics*, **75**, A147-A164.
- Müller, T. M., G. Lambert, and B. Gurevich, 2007, Dynamic permeability of porous rocks and its seismic signatures: *Geophysics*, **72**, 5, E149– E158.
- O’Connell, R. J., and B. Budiansky, 1974, Seismic velocities in dry and saturated cracked solids: *Journal of Geophysical Research*, **79**, 5412–5426.
- , 1977, Viscoelastic properties of fluid-saturated cracked solids: *Journal of Geophysical Research*, **82**, 5719–5740.

- Plona, T., 1979, Observation of a second bulk compressional wave in a porous medium at ultrasonic frequencies, *Applied Physics Letters*, **36**(4), 259-261.
- Pride, S. R., and J. G. Berryman, 2003a, Linear dynamics of double-porosity and dual-permeability materials. I. Governing equations and acoustic attenuation: *Physical Review E*, **68**, 036603.
- , 2003b, Linear dynamics of double-porosity and dual-permeability materials. II. Fluid transport equations: *Physical Review E*, **68**, 036604.
- Pride, S. R., J. G. Berryman, and J. M. Harris, 2004, Seismic attenuation due to wave induced flow: *Journal of Geophysical Research*, **109**, no. B1, B01201.
- Sams, M. S., J. P. Neep, and M. H. Worthington, 1997, The measurement of velocity dispersion and frequency-dependent intrinsic attenuation in sedimentary rocks: *Geophysics*, **62**, 1456–1464.
- Skempton, A. W., 1954, The pore-pressure coefficients A and B: *Geotechnique*, **4**, 143–147.
- Thomsen, L., 1985, Biot-consistent elastic moduli of porous rocks: low-frequency limit, *Geophysics*, **50**, 2797-2807.
- Tang, X., 2011, A unified theory for elastic wave propagation through porous media containing cracks- An extension of Biot's poroelastic wave theory: *Science China—Earth Sciences*, **54**, 1441– 1452.
- Tang, X., and C. H. Cheng, 1989, A dynamic model for fluid in open borehole fractures: *Journal of Geophysical Research*, **94**, 7567-7576.
- Toll, J. S., 1956, Causality and the dispersion relation: Logical foundations: *Physical Review*, **104**, 1760–1770.
- Walsh, J. B., 1965, The effect of cracks on the compressibility of rock: *Journal of Geophysical Research*, **70**, 381–389.
- White, J. E., 1975, Computed seismic speeds and attenuation in rocks with partial gas saturation: *Geophysics*, **40**, 224–232.
- Winkler, K., and A. Nur, 1982, Seismic attenuation—Effects of pore fluids and frictional sliding: *Geophysics*, **47**, 1–15.
- Zhang, S., F.D. Maestra, N. Combaret, R. Klimentidis, P. Barthelemy, R. Albou, D. Lichau, and D. Bernard, 2011, The analysis and simulation of rock properties using FIB-SEM and virtual material studio, NAFEMS World Congress 2011, Boston, USA.

3 DYNAMIC FLUID MODULUS: DISPERSION AND ATTENUATION FROM WAVE-INDUCED FLUID FLOW IN HETEROGENEOUS POROUS MEDIA

3.1 Summary

In this study, we propose to use a frequency-dependent dynamic fluid modulus to link the wave-induced fluid flow (WIFF) directly to the bulk modulus dispersion and wave attenuation in heterogeneous porous rocks. With a clear physical meaning and simple mathematical expression, the dynamic fluid modulus can be used in Gassmann's equation to predict the dispersion and attenuation. The new method is applied to a pore-crack system to predict the P-wave velocity dispersion induced by squirt flow, with either single or multiple sets of cracks. Inverting the dynamic fluid modulus from measured low frequency and ultrasonic data provides an indicator of the level of heterogeneity of the rock.

3.2 Introduction

By allowing the relative movement between solid frame and fluid, Biot (1956a, b, 1962) first revealed wave-induced inertial fluid flow and the dispersion/attenuation associated with it. However, Biot dispersion in general is not a major mechanism in comparison with non-Biot dispersion, as shown by Han (1986). Since then, many WIFF related non-Biot dispersion/attenuation mechanisms have been proposed and formulated. Squirt flow (O'Connell and Budiansky, 1977; Dvorkin *et al.* 1995) focus on the fluid flow from softer cracks to stiffer round pores at pore scale. White (1975) studied the fluid flow caused by compressibility heterogeneity

between two immiscible fluids (patch saturation). The double-porosity and dual-permeability model (Berryman and Wang 1995; Pride and Berryman 2003a, b) provides a more general framework to explicitly relate internal fluid flow to bulk modulus dispersion, and can cover mesoscopic heterogeneity which is recently believed (*e.g.*, Müller *et al.*, 2010) to account for majority of dispersion and attenuation observed in seismic and well-log data in rocks. In Pride and Berryman's approach, not only the fluid saturated bulk modulus, but also the dry rock bulk modulus are formulated as frequency-dependent parameters. While it is known that this is just an effective way to account for the frequency-dependent fluid flow effect, it is still against the intuition that the dry rock properties vary with frequency. In this study an alternative approach is proposed to use only one frequency dependent effective property: the fluid modulus, which is directly related to the fluid flow, for modeling the non-Biot dispersion.

3.3 Partial drainage and dynamic fluid modulus

Gassmann's equation predicts the fluid effect under undrained condition. "Undrained" means that the boundary is closed so that no fluid is allowed to flow into or out from a representative element volume (REV). What will happen if the boundary is not fully closed? It has been experimentally observed that bulk modulus drops if there is leak at the surface of the core sample (Hofmann, 2006). If part of the pore fluid is squeezed out of the REV, then the extra support by the fluid will decrease. If there is additional fluid flowing into the REV, then the extra support increases. A "dynamic fluid modulus" can be introduced to account for this partial

drainage effect. A decreased support can be equivalent to a “still closed system with a reduced fluid modulus”; and vice versa, an increased support can be modeled as an increased fluid modulus. (Figure 3.1)

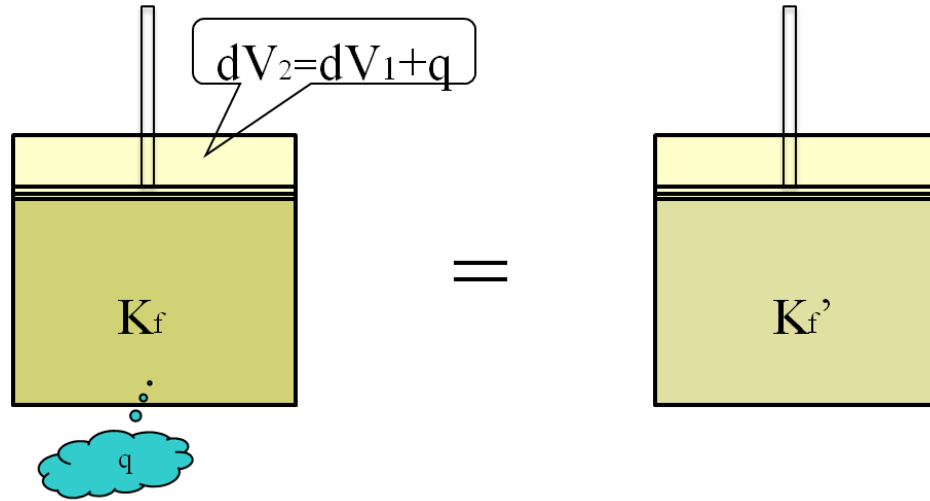


Figure 3.1 Partial drainage effect can be equivalent to a modified “Dynamic Fluid Modulus”

At closed undrained condition, no fluid can flow in or out of the pore space.

Therefore the pore volume change equals to fluid volume change, or

$$-\frac{1}{K_f} = \frac{dV_f/V_f}{dP_f} = \frac{dV_p/V_p}{dP_p} \quad (3.1)$$

Here K_f is the fluid bulk modulus; V_f and V_p denote fluid volume and pore volume respectively; and P_f and P_p denote fluid pressure and pore pressure. At partial drained condition, responding to the applied external stress change, a small amount of fluid will be squeezed out or sucked into the pore space. This amount can be denoted as q , a positive value for incoming flow, and negative value for outgoing flow. Taking

this into account, the pore volume change consists of two parts. The first part is the fluid volume change (compression or dilation) due to the pore pressure change, and the second part comes from the fluid flow amount q . Note that under increasing external pressure, both parts are negative, and the resultant pore volume change is also negative. By imagining that the pore is still closed, but filled with another fluid, with a modified bulk modulus K_f' :

$$\frac{1}{K_f'} = -\frac{(dV_f + q)/V_p}{dP_p} = \frac{1}{K_f} - \frac{q/V_p}{dP_p} \quad (3.2)$$

One can then still use the Gassmann's equation with this K_f' , since the partial drainage effect is equivalently included in this modified fluid modulus (see detailed derivation in Appendix A).

$$K_{sat} = K_{dry} + \frac{\alpha^2}{(\alpha - \phi)/K_0 + \phi/K_f'} \quad (3.3)$$

The partially drained condition can happen in subsurface. The possible applications may include acoustic logging in open hole, and seismic velocity in highly permeable formation close to gas-filled fractures. However, in most of the cases, the fluid will not flow to “nowhere”, but just flow from one part of the rock to another.

3.4 Internal fluid flow and bulk compressibility

Next, we consider the internal fluid flow caused by rock frame heterogeneity. In this case, the flow does not occur at the outer surface of the REV, but between the

different parts of the rock within the REV. Part of the rock has an incoming flow and the other part has an outgoing flow. There is a coupling between the incoming and outgoing flows. This coupling provides a constraint that one can use to compute the q . First we present a derivation of the maximum q , which represents the fluid flow amount at zero frequency.

Consider a REV consisting of two types of pores with pore volume V_{p1} and V_{p2} respectively. Type 1 is stiffer with bulk modulus K_{dry1} and type 2 is softer with bulk modulus K_{dry2} (Figure 3.2). Assuming under iso-stress condition a positive external pressure is applied to the REV so that both types of pores receive the same confining pressure P_c .

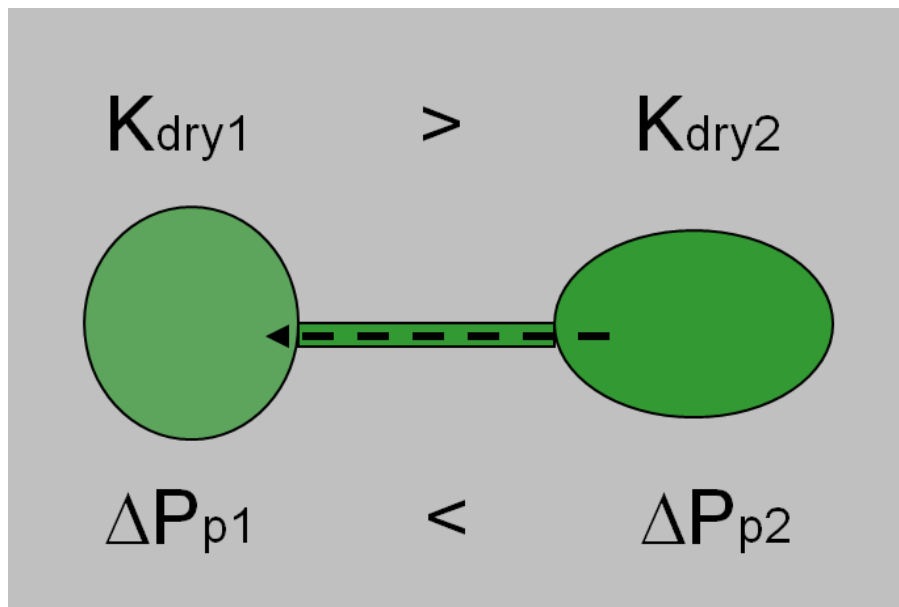


Figure 3.2 Frame stiffness heterogeneity causes pore pressure gradient and internal fluid flow.

First, at the high frequency end, each type of pore is under undrained condition so that the pore pressure in each phase increases separately depending only on its own frame properties (subscript H denotes high frequency):

$$K_f = -\frac{dP_{p1H}}{dV_{p1}/V_{p1}} = -\frac{dP_{p2H}}{dV_{p2}/V_{p2}} \quad (3.4)$$

Here the pore pressure increment in each phase is related to the corresponding confining pressure change by (Thomsen, 1985):

$$dP_{pi} = \frac{\alpha_i K_f}{K_{di} \left[\phi_i + \frac{K_f}{K_0} (\alpha_i - \phi_i) + \alpha_i^2 K_f \right]} dP_c \quad (3.5)$$

Now at zero frequency, fluid in an amount of q flows from pore type 2 to pore type 1. So in pore type 1, the pore pressure change dP_{p1L} becomes (subscript L denotes low frequency):

$$dP_{p1L} = -K_f \frac{dV_{p1} - q}{V_{p1}} \quad (3.6)$$

And in pore type 2 the pore pressure change dP_{p2L} becomes:

$$dP_{p2L} = -K_f \frac{dV_{p2} + q}{V_{p2}} \quad (3.7)$$

Since at zero frequency pore pressures in two phases are equilibrated, $dP_{p1L}=dP_{p2L}$. Combining the above formula with (3.4), one can obtain:

$$q = \frac{1}{K_f} \frac{dP_{p2H} - dP_{p1H}}{1/V_{p1} + 1/V_{p2}} \quad (3.8)$$

Here dP_{p1H} and dP_{p2H} are pore pressure increments at high frequency in phase 1 and 2 respectively.

When $V_{p1} \gg V_{p2}$, (3.8) can be approximated as

$$q = \frac{V_{p2}}{K_f} (dP_{p2H} - dP_{p1H}) \quad (3.9)$$

In a two-phase composite rock, if the elastic properties, porosities, and the volume fraction of each phase are given, the maximum fluid flow amount at zero frequency can be either exactly obtained from equation 3.8 or approximately estimated by equation 3.9. Details on the geometry of the heterogeneities, like size and shape, are not needed to obtain this value, since these will only affect the pore pressure relaxation time and therefore determine the characteristic frequency that mainly separates the relaxed and un-relaxed properties of the heterogeneous porous medium. This will be discussed in more detail later.

Next, we will show how this fluid flow amount q can be related to the change of bulk compressibility of the rock. For clarity, the notation of fluid compressibility $\beta_f = 1/K_f$ is used instead of modulus in this derivation.

At an infinite high frequency, there is no fluid exchange between any pores. Each type of pore just behave as a completely closed system, the pore volume changes in type 1 and type 2 are

$$\delta V_{p1H} = -\beta_f V_{p1} \delta P_{p1H} \quad (3.10)$$

$$\delta V_{p2H} = -\beta_f V_{p2} \delta P_{p2H} \quad (3.11)$$

So the total pore volume change at high frequency δV_H is

$$\delta V_H = \delta V_{p1H} + \delta V_{p2H} = -\beta_f (V_{p1} \delta P_{p1H} + V_{p2} \delta P_{p2H}) \quad (3.12)$$

Then, at low frequency (0 Hz), there is q amount of fluid moved from V_{p2} into V_{p1} ; therefore the pore volume changes in two phases can be written as:

$$\delta V_{p1L} = -\beta_f (V_{p1} + q) \delta P_{pL} \quad (3.13)$$

$$\delta V_{p2L} = -\beta_f (V_{p2} - q) \delta P_{pL} \quad (3.14)$$

And the total pore volume change at low frequency δV_L is

$$\delta V_L = \delta V_{p1L} + \delta V_{p2L} = -\beta_f (V_{p1} + V_{p2}) \delta P_{pL} \quad (3.15)$$

Now let us look at the difference of the total pore volume change between low frequency and high frequency cases:

$$\delta V_L - \delta V_H = -\beta_f \left[V_{p1} (\delta P_{pL} - \delta P_{p1H}) + V_{p2} (\delta P_{pL} - \delta P_{p2H}) \right] \quad (3.16)$$

When $V_1 \gg V_2$, the fluid flow will barely change the pore pressure in V_1 thus the first term in the right hand side vanishes, and (3.16) can be approximated to:

$$\delta V_L - \delta V_H = -\beta_f V_{p2} (\delta P_{pL} - \delta P_{p2H}) \quad (3.17)$$

Compared to (3.9), this is just the amount of fluid moved from V_{p2} into V_{p1} . One can conclude that, under the condition that the soft pore space is much smaller than the stiff pore space, the applied stress will cause a larger deformation at zero frequency than at high frequency due to the fluid flow from the soft space into the stiff space. The difference between them is approximately equal to the volume of the fluid flow from the soft space to the stiff space.

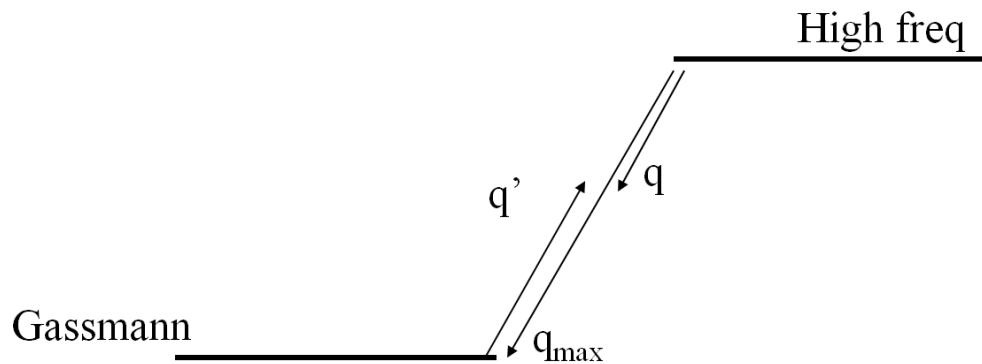
Although the above reasoning is based on the process from an infinitely high frequency relaxing to zero frequency, it is obvious that the same reasoning is also valid for any intermediate non-zero frequency as long as the fluid amount $q=q(f)$ at this frequency can be determined. The zero frequency case is just a specific case in which the relaxation is fully accomplished from the high frequency end, with the maximum internal fluid flow amount q_{max} .

However, if one wants to build the dispersion curve above the well-established Gassmann formulation which represents the zero frequency, one should treat it in a reversed way. It can be imagined that any non-zero frequency case is caused by the fluid flow from the stiffer phase to the softer phase, with the amount of $q'(f)$

$$q'(f) = -(q_{\max} - q(f)) \quad (3.18)$$

Here q_{\max} is defined by (3.8), or can be obtained from any specific modeling by setting frequency $f=0$ Hz (Figure 3.3). Based on this analysis, one can modify (3.2) to the following:

$$\frac{1}{K_f''} = \frac{1}{K_f} - \frac{q'/V_p}{dP_p} \quad (3.19)$$



$$q' = -(q_{\max} - q)$$

Figure 3.3 At non-zero frequency, rock is stiffened by an equivalent incoming fluid flow q' .

Note that equation 3.18 differs from equation 3.2 critically, since it includes an additional step to enable us to treat any non-zero frequency case as a deviation from the zero frequency case. With this treatment, the frequency dependent $1/K_f''$ can be used to replace the original $1/K_f$ in Gassmann's equation, to correctly characterize the velocity dispersion and attenuation due to internal fluid flow. The detailed mathematical derivation is presented in Appendix A.

$$K_{sat} = K_{dry} + \frac{\alpha^2}{(\alpha - \phi) / K_0 + \phi / K_f''} \quad (3.20)$$

3.5 Determination of fluid flow amount q

So the problem left now is to find out the amount of fluid flow as a function of frequency $q=q(f)$. Obviously, this q should be associated with the following factors: pressure gradient at boundary between two phases, local permeability or transport coefficient at boundary, and fluid viscosity, which in turn should be functions of frequency. Derivation of analytical expression of fluid flow q requires detailed information about the geometry of the heterogeneity. It involves Navier-Stokes equation with some assumption on the boundary conditions. Certain approximations are also required to obtain practical solutions. Nevertheless, due to the nature that all internal flows are diffusive-type flows, it is possible to use a general expression on internal fluid flow (Berryman, 2003):

$$q = \frac{q_{max}}{(1 - 0.5i\omega / \omega_c)^{1/2} - i\omega / \omega_c} \quad (3.21)$$

Here q_{max} is obtained using equation 3.8 or 3.9; ω is the angular frequency of perturbing stress; ω_c is the characteristic frequency to separate the relaxed and unrelaxed regions.

To estimate ω_c , two different scales of heterogeneities need be considered separately. The cases of pore or grain size heterogeneities will be discussed in section 3.6. Here for the cases in which heterogeneity size is much larger than the pore or grain size for orders of magnitudes, the diffusion process can be properly described by Darcy's law (Darcy, 1856) using the permeability. In those cases, the ω_c can roughly be estimated to be (Mavko *et al.*, 2009):

$$\omega_c \approx \frac{4D}{L^2} \quad (3.22)$$

D is the diffusivity of the less permeable phase, and L is the characteristic length of the heterogeneity.

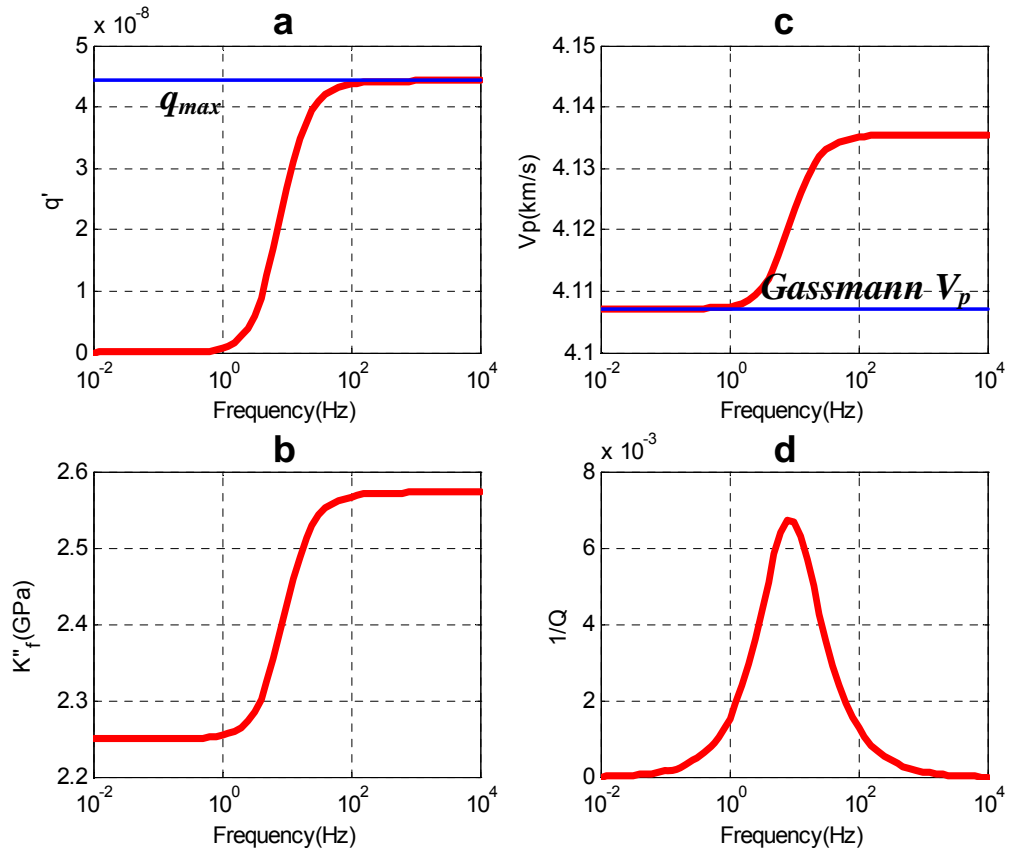


Figure 3.4 a) Internal fluid flow. b) Dynamic fluid modulus. c) P-wave velocity dispersion predicted from dynamic fluid modulus (red) and Gassmann prediction (blue). d) P-wave attenuation 1/Q predicted from dynamic fluid modulus. Heterogeneity size=30cm.

As an example, this approach is used to model a two-phase rock with mesoscale heterogeneity. Both phases are quartz grain packages but phase one is well consolidated and phase two is loose. All input parameters are listed in Table 3.1.

Table 3.1 Input parameters used to compute the P-wave dispersion and attenuation in Figure 3.4.

	Phase 1	Phase 2
Volume fraction	0.99	0.01
Grain bulk modulus K_0 (GPa)	37	37
Dry bulk modulus K_{dry} (GPa)	18	2
Saturated shear modulus μ_{sat} (GPa)	15	
Saturated density ρ (g/cc)	2.49	2.49
Porosity ϕ	0.1	0.1
Permeability κ (Darcy)	0.01	0.01
Fluid bulk modulus K_f (GPa)	2.25	
Fluid viscosity η (cP)	1	
Heterogeneity size L (cm)	30	

Figure 3.4a shows the fluid flow amount normalized to the bulk volume. This is actually the imagined reversed flow amount (Equation 3.18); therefore has 0 value at the low frequency end and maximum value at the high frequency end. The characteristic frequency appears around 10 Hz. Figure 3.4b, displays the calculated dynamic fluid modulus. At relaxed zone it equals the virgin water bulk modulus 2.25 GPa. Climbing up through the dispersion zone around the characteristic frequency, it finally reaches the unrelaxed value 2.57 GPa. Figure 3.4c is the resultant water saturated P-wave velocity dispersion curve, which shows about 0.7% dispersion. Figure 3.4d shows the P-wave attenuation with an absorption peak at the characteristic frequency.

3.6 Example: Dispersion and attenuation in water saturated porous/cracked rocks

For grain or pore scale heterogeneities, like in squirt flow models, fluid flow is controlled by a parameter called transport coefficient (Pride and Berryman, 2003b).

This parameter is highly dependent on the detailed geometry of the microstructure. If the featuring structure is close to a regular shape, like ellipse, then solving Stokes equation is a feasible way to obtain the full frequency range fluid transport behavior. If the shape is highly irregular, a numerical technique like finite element method is probably the only way to estimate the ω_c .

Many authors (*e.g.* Eshelby, 1957; Walsh, 1965; Kuster and Toksöz, 1974; O'Connell & Budiansky, 1974, 1977; Cheng, 1978; Hudson, 1980,1981) have used a penny-shaped ellipsoidal inclusion to model the relatively compliant pore space, in order to obtain an analytical expression for effective media properties. Tang and Cheng (1989) developed a dynamic model to relate the Stoneley wave dispersion and attenuation to the fluid flow into the fracture. By solving the pressure distribution in a penny-shaped crack, Tang (2011) described and formulated the fluid flow from thin cracks into round pores as:

$$\frac{q}{\delta P_f V_f} = \frac{8\pi\varepsilon(1-\nu_s)}{3\phi\mu_s} f(\zeta) \left[\frac{1/K_d - 1/K_s}{1/K_d - 1/K} - f(\zeta) \right] \left/ \left\{ 1 + \frac{4(1-\nu_s)K_f}{3\mu_s\gamma} [1 - f(\zeta)] \right\} \right. \quad (3.23)$$

The cracks are assumed randomly oriented with dilute concentration. The left hand side of equation 3.23 is just the same as the second term in our definition of dynamic fluid modulus (equation 3.2). The two dominant controlling parameters are crack density ε and crack aspect ratio γ . The other inputs include the grain bulk modulus K_s , shear modulus μ_s , Poisson ratio ν_s , the frame dry bulk modulus K_d , porosity ϕ , and fluid bulk modulus K_f . Frequency dependency is included in

$$f(\zeta) = \frac{2J_1(\zeta)}{\zeta J_0(\zeta)} \quad (3.24)$$

$$\zeta = \sqrt{3i\omega\eta / K_f} / \gamma \quad (3.25)$$

J_1 and J_0 are the order one and order zero first class Bessel functions, and η is the fluid viscosity.

We use this expression of q to compute the dynamic fluid modulus, and then use Gassmann's equation to model the P-wave dispersion in a crack-pore system (Figure 3.5). All input rock and fluid parameters in Table 3.2 are the same as in Tang (2011). As a comparison, we also plot the result from Tang's model. The dispersion curves from both methods looks very similar to each other. However, we can see a number of differences:

1. At low frequencies, Tang's model gives a value below the (generally accepted) Gassmann velocity, calculated from the dry velocity using the standard Biot-Gassmann formula. This is not surprising because in Tang's model the squirt flow contribution to the saturated bulk modulus is expressed in a Gassmann-type equation (eqn. 15 & 16 of Tang (2011)) as:

$$K = K_d + \alpha^2 / [(\alpha - \phi) / K_s + \phi / K_f + S(\omega)] \quad (3.26)$$

$$S(\omega) = \frac{8\pi\varepsilon(1-\nu_s)}{3\mu_s} f(\zeta) \left[\frac{1/K_d - 1/K_s}{1/K_d - 1/K} - f(\zeta) \right] \left/ \left\{ 1 + \frac{4(1-\nu_s)K_f}{3\mu_s\gamma} [1 - f(\zeta)] \right\} \right. \quad (3.27)$$

In the limit of zero frequency ($\omega \rightarrow 0$), the term $f(\zeta) \rightarrow 1$, and the equation 3.27 reduces to:

$$S(0) = \frac{8\pi\varepsilon(1-\nu_s)}{3\mu_s} \left[\frac{1/K_d - 1/K_s}{1/K_d - 1/K} - 1 \right] \quad (3.28)$$

Since this is a non-zero positive real number and appearing in the denominator of the second term in equation 3.26, the low frequency limit predicted by this model goes obviously below the Gassmann value.

At high frequencies (near 10^4 Hz in Figure 3.5), $f(\zeta)$ (eqn. 3.24) goes to zero, so that $S(\omega)$ (eqn. 3.27) goes to zero as well, and K (eqn. 3.26) goes to the Gassmann value identically.

At still higher frequencies, the global flow effect becomes evident, as discussed later.

2. At intermediate frequencies (10^2 - 10^4 Hz), Tang's model shows a greater increase than the present model. This is due to Tang's analysis in terms of q , compared to the present analysis in terms of q' .

Tang (2012) also suggested another expression without using Bessel functions (eqn. 5 of Tang (2012)):

$$S(\omega) = \frac{\frac{8\varepsilon(1-\nu_0)(1+\lambda)^3}{3\mu_0} \left(\frac{1/K_0 - 1/K_s}{1/K_d - 1/K_0} \right) M}{1 - \frac{3i\omega\eta(1+2\lambda)}{K_f\lambda\gamma^2} \left[1 + \frac{4(1-\nu_0)K_f(1+\lambda)^3}{3\pi\mu_0\gamma(1+2\lambda)} M \right]} \quad (3.29)$$

$$\text{where } M \equiv 1 + \frac{4-5\nu_0}{2(7-5\nu_0)} \frac{\lambda^3}{(1+\lambda)^3} + \frac{9}{2(7-5\nu_0)} \frac{\lambda^5}{(1+\lambda)^5}$$

$$\lambda \equiv \left(\frac{3\phi}{4\pi\varepsilon} \right)^{1/3}$$

In the limit of low frequency, this becomes:

$$S(0) = \frac{8\varepsilon(1-\nu_0)(1+\lambda)^3}{3\mu_0} \left(\frac{1/K_0 - 1/K_s}{1/K_d - 1/K_0} \right) M \quad (3.30)$$

This is also a non-zero positive value at zero frequency, therefore will still predict a low frequency limit below the Gassmann value.

In our present model, we use reversed flow q' instead of q in calculating the dynamic fluid modulus. As shown in Figure 3.3, q' has 0 value at zero frequency. So that when frequency goes to zero ($\omega \rightarrow 0$), the dynamic fluid modulus calculated using equation (3.19) just reduces to original fluid modulus; and the saturated bulk modulus calculated using equation (3.20) reduces identically to the original Gassmann value, as it should.

Note that, at the highest frequencies, ($> 10^5$ Hz), both models show the same Biot (global flow) dispersion effect. They are calculated using standard Biot dispersion formulations (Tang and Cheng, 2004).

Table 3.2 Input parameters used to computer P-wave dispersion in Figure 3.5, after Tang (2011)

Parameters (unit)	Value
Grain bulk modulus K_0 (GPa)	37.9
Grain shear modulus μ_0 (GPa)	32.6
Grain density ρ (g/cc)	2.65
Fluid bulk modulus K_f (GPa)	2.25
Fluid density ρ_f (g/cc)	1
Porosity ϕ	0.25
Permeability κ (Darcy)	1
Fluid viscosity η (cP)	10
Crack density ε	0.15
Crack aspect ratio γ	0.001

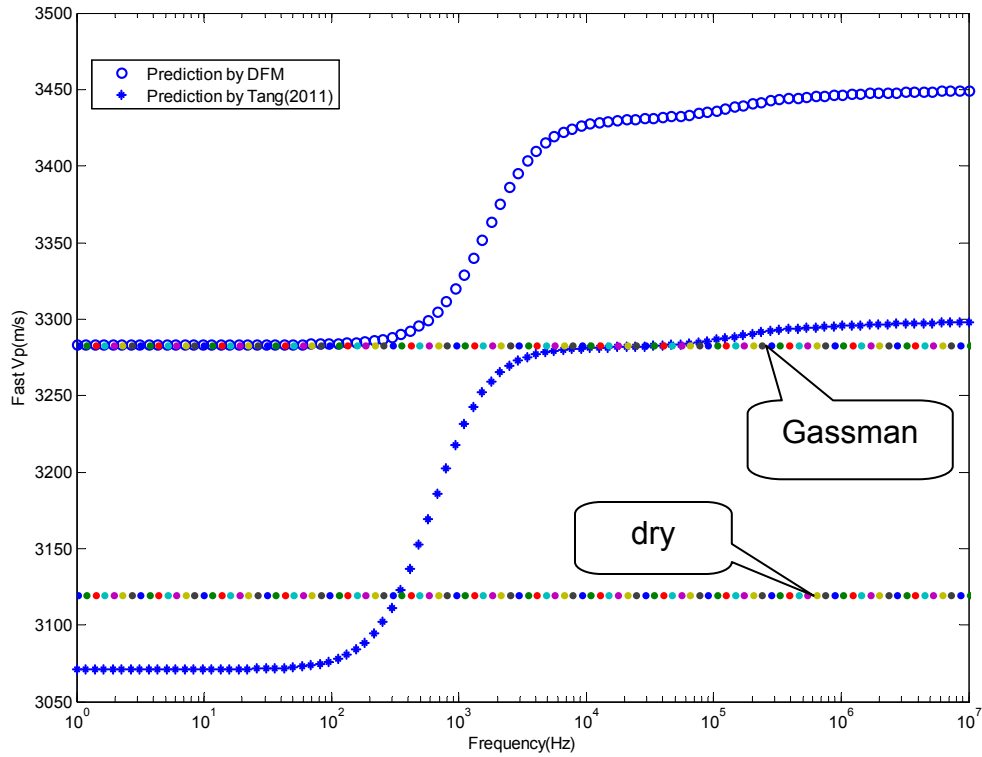


Figure 3.5 Comparison between P-wave dispersions modeled by dynamic fluid modulus and by Tang's model (2011), using the rock and fluid parameters given in Table 3.2.

Furthermore, in real rocks, multiple scales of heterogeneities can coexist either in discrete or continuous spectrum (O'Connell and Budiansky, 1977). To model them using single set of heterogeneity is mostly for the mathematical simplicity and convenience. Liu *et al.* (1976) has conceptually demonstrated that by superimposing multiple relaxation mechanisms together, one can obtain a much wide dispersion curve and a relatively “constant” attenuation value in the corresponding frequency range. However, to model the multiple heterogeneities of real rocks is still challenging, due to above mentioned mathematical complexity. The concept of dynamic fluid modulus we proposed here may possibly provide an easy tool to

address this issue. If each set of heterogeneity can be represented by a corresponding dynamic fluid modulus, then the total heterogeneity can be represented by

$$\frac{1}{K_f'} = \frac{1}{K_f} - \sum_i \frac{q_i' / V_p}{dP_p} \quad (3.31)$$

Here i refers to each set of heterogeneity. To demonstrate this, in Figure 3.6, we simulate a rock with seven sets of cracks. Panel a shows the crack density and aspect ratio for each set of crack. In panel b we display both the real (red) and imaginary (blue) parts of the total dynamic fluid modulus, along with the original fluid modulus of 2.25 GPa, which represents a homogeneous rock. The multiple scales of heterogeneities in this simulation predict a wide spectrum of fast P-wave velocity dispersion (c) and attenuation (d), which are often observed in real reservoir rocks.

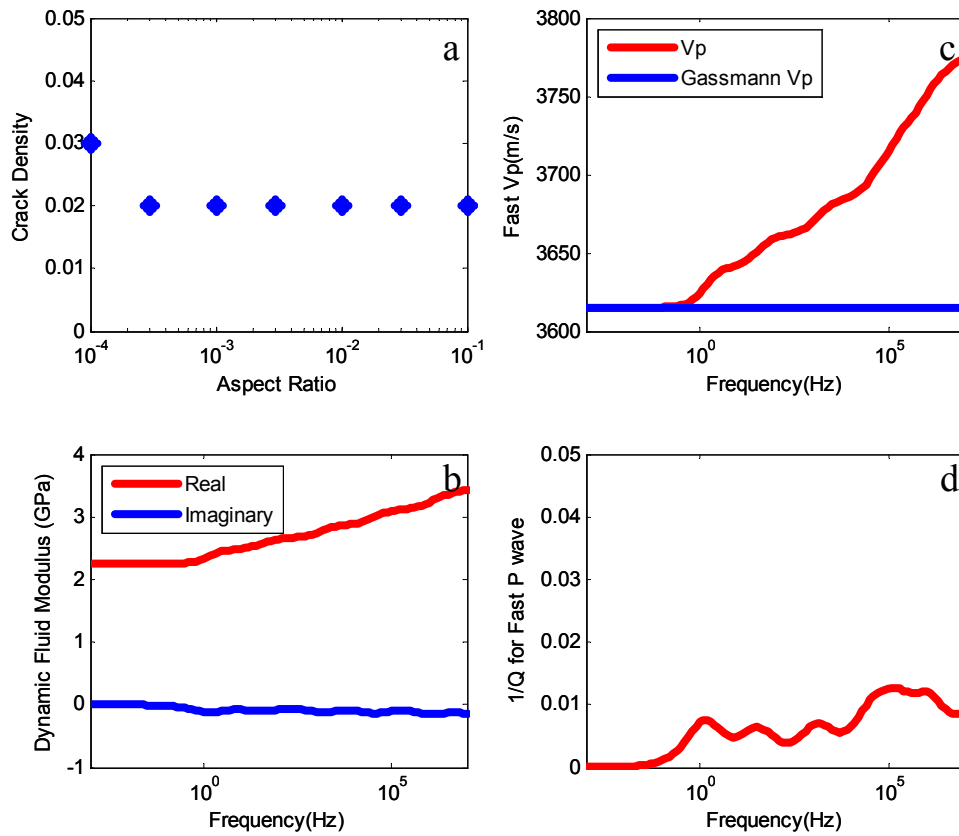


Figure 3.6 A wide band of dispersion and attenuation is simulated by seven sets of cracks, each set with its own crack density and aspect ratio.

3.7 Inverting dynamic fluid modulus from lab-measured data

We have demonstrated that the concept of a dynamic fluid modulus can help model the wave dispersion and attenuation due to WIFF in heterogeneous rocks. It is interesting to evaluate whether this parameter can be used in analyzing measured data, to provide some new insights about rock properties.

A typical laboratory measurement on rock samples consists of dry and water saturated velocities. While the real sample is heterogeneous, and may have velocity dispersion at non-zero frequency fluid saturated measurements, one can effectively view it as a homogeneous one, and apply the Gassmann's equation to the measured data to invert for an "effective dynamic fluid modulus". These inverted values are obviously frequency dependent, and may also be affected by other measurement conditions like differential pressure, temperature, and especially the boundary condition of pore fluid system that can influence the system heterogeneity in term of fluid connection.

Figure 3.7 is the results from a recent low frequency measurement. The sample is a Berea sandstone, with 22.3% porosity and 407 mD permeability. Based on measured Young's modulus and Poisson ratio, as well as the phase difference between strain and stress, the calculated P-wave velocity and attenuation $1/Q$ are displayed in Figures 3.7a and 3.7b. Besides the dry rock condition, two distinct fluid boundary conditions are tested when the sample is water saturated. There is a valve placed very close to the entry point of the pore fluid line into the sample. During the first experiment, the valve was closed after the pore pressure reached the desired setting value, so that the sample pore system was on a closed or undrained condition. In the second experiment, the aforementioned valve was opened. Due to the fairly high permeability of this sample, the pore system inside the sample is well connected to the pore pressure control system, which includes a ISCO digital pump. This pump is

equipped with a large fluid reservoir and a mechanical piston, and imposes a single dashpot like friction force relaxation mechanism into the whole fluid system; therefore the pore fluid inside the sample was under a typical partially drained condition with a viscous boundary. This explains the narrow absorption peak observed in the attenuation plot, as well as the sharp dispersion jump in the velocities plot, for the drained measurement.

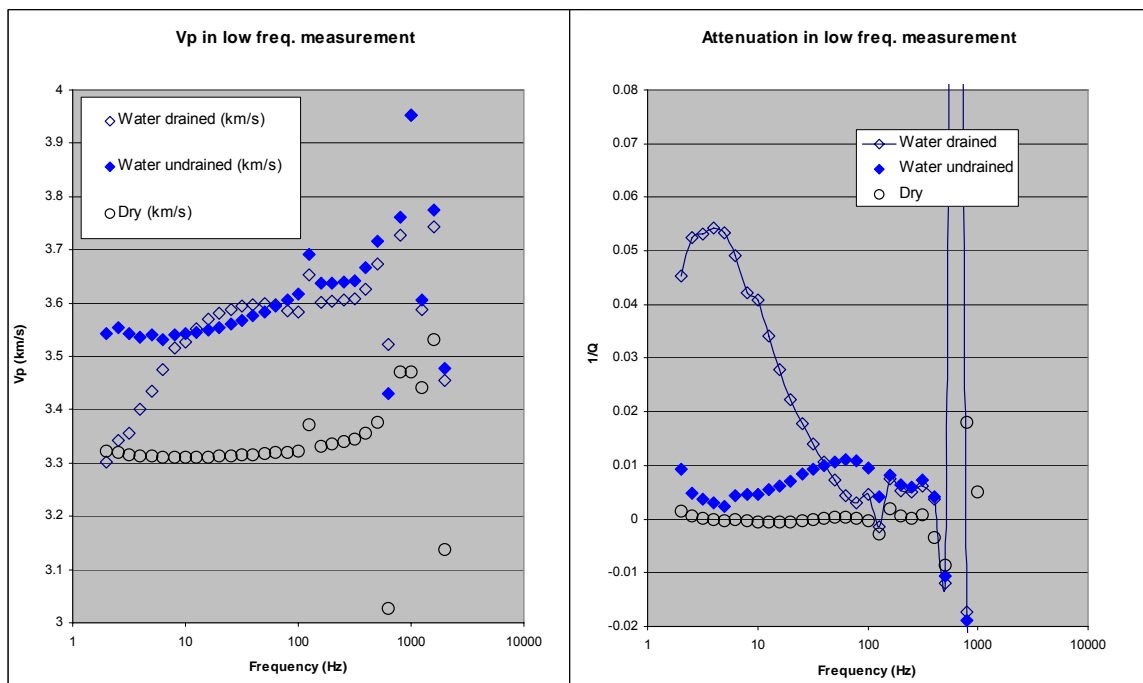


Figure 3.7 a) Left. Low frequency measured V_p in three different saturation conditions. b) Right. Attenuation $1/Q$ under the same conditions as in a. Measurements made with apparatus discussed in chapter 5.

In Figure 3.8, the calculated effective dynamic fluid modulus (DFM) against the frequency is plotted. The real bulk modulus of water at our measurement pressure of 300 psi is 2.25 GPa. First the undrained water saturated data were examined. In our

whole measurement frequency range of 2-2000 Hz, the DFM starts from around 2.7 GPa at the low frequency end, and gradually increase to around 3.5 GPa in the 10-100 Hz frequency range. This means that certain heterogeneity exists in this rock sample, and even under seismic frequency the pore pressure gradient between those heterogeneities cannot relax completely. The rising ramp between 10-100 Hz may represent certain particular geometry of the heterogeneity. This also matches the observed overall above zero value and a moderate peak in the $1/Q$ plot for the undrained water measurement (Figure 3.7). When the pore fluid is partially drained, the DFM remains on similar value as the undrained, at frequencies above 100 Hz. Towards the lower frequency, however, it can be observed that there is a huge drop of the DFM value, and it even goes well below the virgin water bulk modulus. This can be well explained by equation 3.2 where an outgoing external fluid flow is defined by a negative q , and takes down the dynamic fluid modulus.

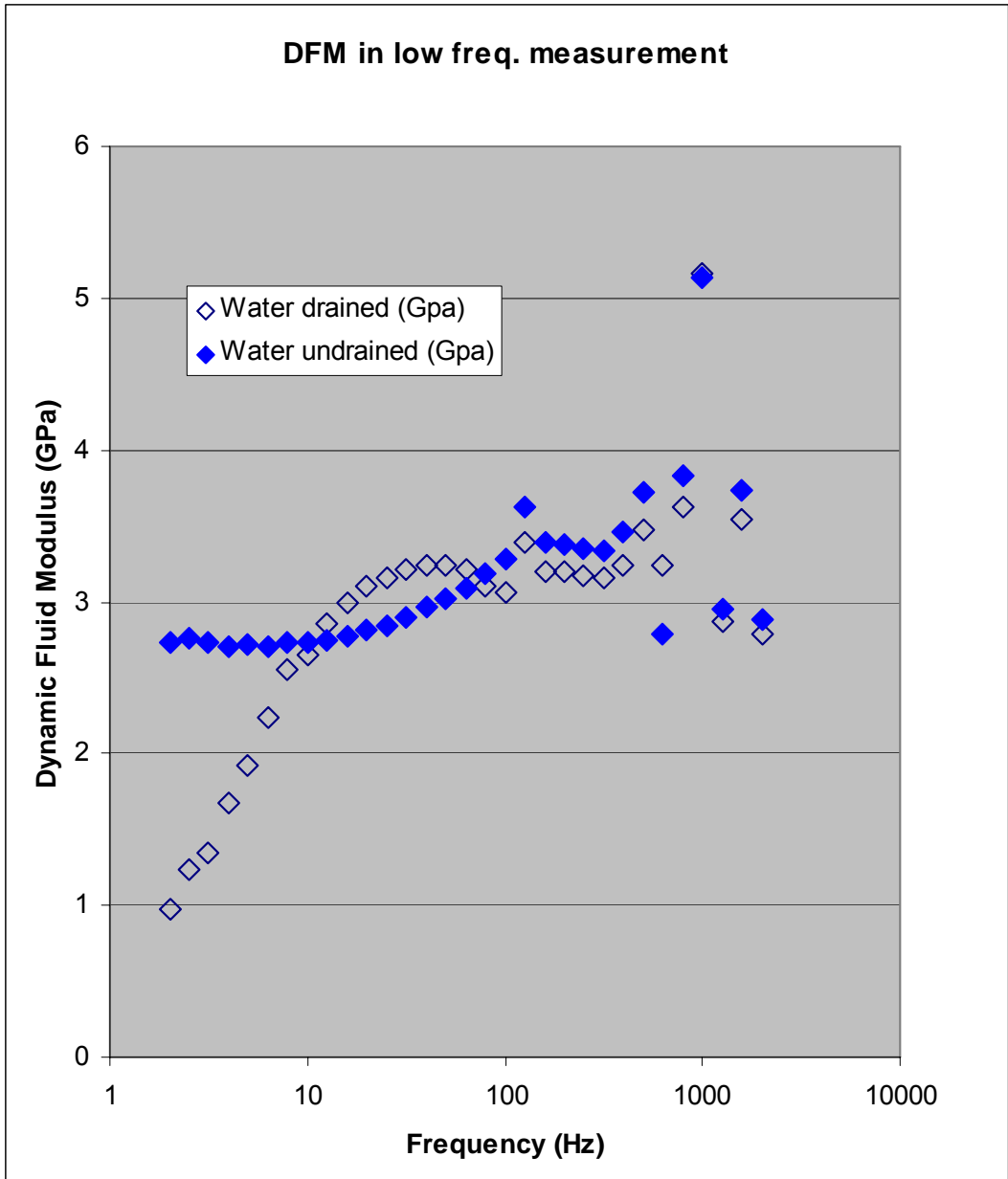


Figure 3.8 Inverted dynamic fluid modulus from the data shown in Figure 3.7.

While broad band laboratory measurement data are still rarely available, one can use the widely available ultrasonic data to invert the dynamic fluid moduli at the particular measurement frequency, and use them as indicators of heterogeneity, to get some insights to the composition, structure, and texture of the interested rock.

We use Han's data (Han, 1986) to calculate the real part of the dynamic fluid moduli at differential pressure range of 5-50 MPa. Two subsets of the results are plotted in Figure 3.9. The first subset covers clean sandstones, and the second for shaly sandstones. First of all, the inverted DFM for all samples have values greater than the virgin water bulk modulus at 2.25 GPa. This suggests that in ultrasonic measurement, although the pore fluid line is not closed, there is no partial drainage effect from this open boundary condition. It also suggests that all samples exhibit certain level of heterogeneity, and at the ultrasonic frequency, the pore pressure gradient among those heterogeneities cannot be equilibrated. Second, while most samples have DFM between 4-6 GPa, there are three samples having much large DFM values. Investigating into other properties of the samples reveals that all of those three samples have fairly low porosity around 4-6%. This encouraged us to cross plot the DFM vs. porosity in Figure 3.10. As expected, there is a general DFM decreasing trend with increasing porosity. This observation implies that in well consolidated low porosity sands, it is more likely to contain thin cracks, and form a high level of stiffness contrast to the background.

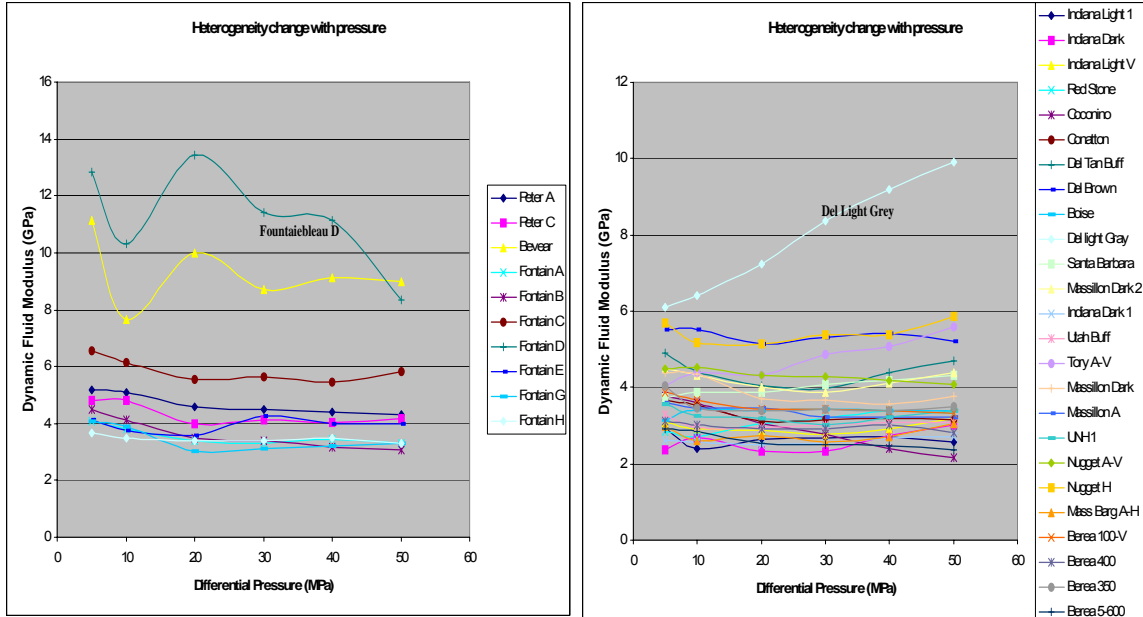


Figure 3.9 Dynamic fluid moduli inverted from ultrasonic measurement data using Gassmann equation indicate the rock heterogeneities, and their response to pressure change.

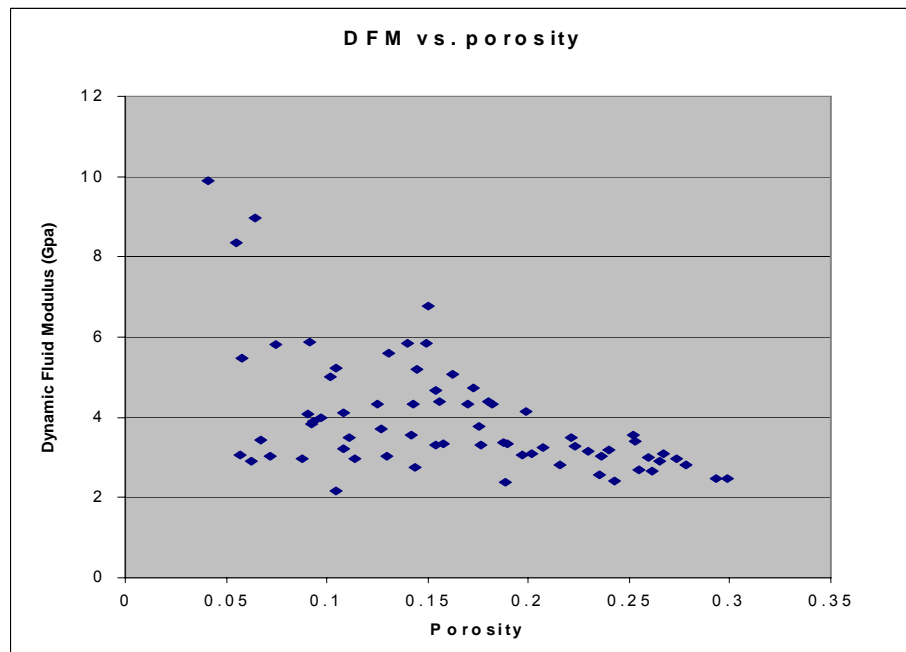


Figure 3.10 Inverted dynamic fluid modulus has a negative correlation with porosity. (From Han's data, 1986).

Finally, while most of the samples exhibit the decreasing DFM trends with increasing pressure, the Delaware Light Grey sample has a totally reversed trend. Such behavior has been also identified for a couple of other samples in the whole dataset. According to common crack models, the increasing pressure tends to close the cracks, resulting higher modulus and less heterogeneity (Nur, 1971; Cheng, 1993). Current observations cannot be explained by the existing crack closing models. If one accept that the inverted DFM is an indicator of the heterogeneity, it seems for some rocks, increasing the pressure will lead to even higher heterogeneity.

Closing of a crack happens only when the pressure reaches a certain value called closing pressure (Mavko *et al.*, 2009). Before this closing pressure, the deformation of the crack will reduce the crack porosity φ_c . At the same time, the crack aspect ratio α may or may not alter much, depends on the nature of the crack. If the crack is in elliptical shape, the applied pressure will push two crack faces closer without shortening its length considerably. This will cause the aspect ratio decrease almost with the same pace as the crack porosity, resulting in a nearly constant crack density ε , defined as (Budiansky and O'Connell, 1976):

$$\varepsilon = \frac{3}{4\pi} \frac{\varphi_c}{\alpha} \quad (3.32)$$

In cracked effective media theories, dry effective properties are controlled neither by crack porosity ϕ_c nor by the aspect ratio α , but by their ratio, or crack density ε , as shown in eqn. 3.33 (Budiansky and O'Connell, 1980; Thomsen, 1985).

$$\begin{aligned} K_{dry} &= K_0 \left(1 - \frac{\phi_p}{1 - a_0} - A_0 \varepsilon \right) \\ \mu_{dry} &= \mu_0 \left(1 - \frac{\phi_p}{1 - b_0} - B_0 \varepsilon \right) \end{aligned} \tag{3.33}$$

In above equations, K_0 , μ_0 are grain bulk and shear moduli, ϕ_p is porosity for non-crack pores. Four model parameters a_0 , b_0 , A_0 , B_0 are only functions of grain Poisson ratio. However, fluid saturated properties in the same media can be influenced by the individual value of aspect ratio and crack porosity (due to the porosity term in Gassmann equation). Le Ravalec and Gueguen (1996) showed that under the same crack density, a rock with thinner crack and lower porosity will have larger fluid effect. This is also depicted here in Figure 3.11, in which the crack density is fixed at 0.0239, with the aspect ratio varies from 0.01 to 0.005. The corresponding crack porosity decreases from 0.1 to 0.05. The dry bulk modulus is calculated using eqn. 3.33, and water-saturated bulk modulus is obtained using Gassmann equation. The results show that the water saturated modulus increases with decreasing crack porosity, while the dry modulus remains unchanged.

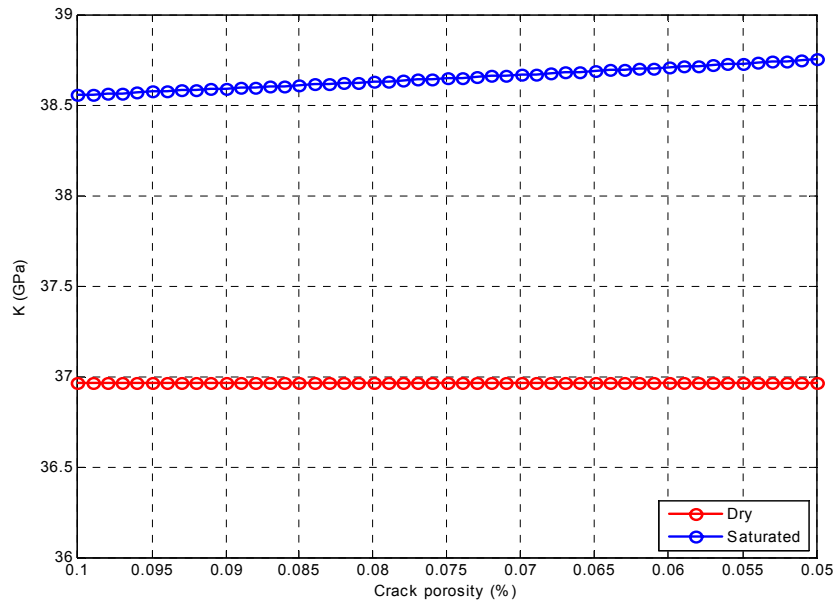


Figure 3.11 At a fixed crack density, fluid effect increases with decreasing crack porosity (and aspect ratio), while the dry bulk modulus remain as constant. Calculation performed with equation 3.33 for dry bulk modulus and Gassmann equation for saturated bulk modulus.

The significant implication from the above analysis is that, when this kind of cracks are mixed with round pores to form a typical porous cracked rock, the distinct isolated saturation effects in the cracks and round pores constitute the heterogeneity. When the pressure increased, some of the cracks may close if the pressure exceeds the closing pressure for those particular cracks. The remaining unclosed cracks have enhanced fluid saturation effects due to the reduced crack porosity and aspect ratio. To demonstrate this, a numerical experiment is used to simulate a rock with 5% round pore porosity, and initially 0.1% crack porosity, and initial crack aspect ratio of 0.01. To simulate the pressure effect, we assign a simple porosity reduction function, in

which the crack porosity linearly reduces from 0.1% to 0.05% when confining pressure P_c increases from 0 to 50 MPa.

$$\phi_c = 0.001 - 0.00001P_c \quad (3.34)$$

To account for the crack closing effect, we also let the crack density slightly reduced with the increasing pressure.

$$\varepsilon = 0.0239(1 - 0.002P_c) \quad (3.35)$$

The resultant moduli are plotted in Figure 3.12a. The dry and low frequency saturated moduli are computed with equation 3.33 and Gassmann equation. To interpret the data measured at ultrasonic frequency, we also compute the high frequency saturated modulus. To prevent the fluid communication between cracks and round pores, the following procedures are used: In first step, the dry bulk modulus is computed for a rock with round pore only, using equation 3.33; In second step, the wet bulk modulus of the above rock is computed using Gassmann equation; In third step, we treat the resultant wet rock in step 2 as a background solid, and add the cracks into it, again using eqn. 3.33, to obtain a rock with dry cracks; finally in step four, Gassmann equation is used to saturated the cracks. Figure 3.12a shows that all three moduli increase with the increasing pressure; but it is difficult to tell how the dispersion or heterogeneity response to the increasing pressure. In Figure 3.12b, we plot the computed dynamic fluid modulus against the pressure and find it does increase with the pressure, matching the observation in Delaware Light Grey and a couple of other samples.

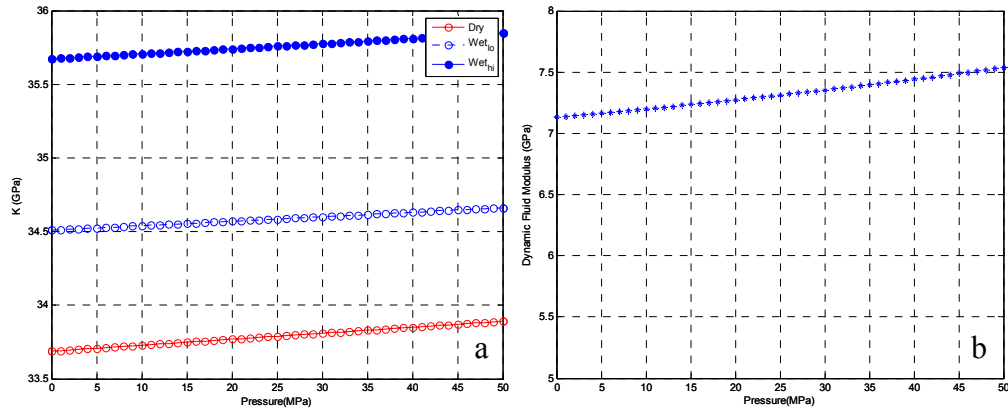


Figure 3.12 In an elliptical crack dominated sandstone. a) Responses of dry and saturated bulk moduli to increasing pressure. b) Indicated by dynamic fluid modulus, increasing pressure results in higher heterogeneity. Calculated with equation 3.33-3.35.

But what about the majority of the sample that showing a stable or decreasing trend with the increasing pressure? Although the ellipsoidal crack is widely used in most of the crack models, in real rocks most of the cracks appear in a non-elliptical form (Mavko and Nur, 1978), with tapered tips. When a compaction pressure is applied, both the thickness and length of the crack are shortened simultaneously. As a first order approximation, the aspect ratio of the crack remains as a constant in this process, but the porosity is reduced in a similar way as in ellipsoidal cracks. The significant difference is that the final crack density is quickly driven down to a lower value by the increasing pressure, even before the crack is closed. A similar numerical experiment is conducted to simulate the non-elliptical crack-dominated rock. This time the aspect ratio is fixed to a constant, and only let the crack porosity linearly reduced with pressure, in the same rate as in the experiment on elliptical crack-dominated rock. The results are shown in Figure 3.13. Compared with Figure 3.12,

one can see that responding to the increasing pressure, the dry and low frequency saturated moduli of non-elliptical cracked rock increase much faster than that of elliptical cracked rock. The most distinctive impacts from those two types of cracks are depicted in Figure 13b. The same increasing compaction pressure may lead to a higher heterogeneity and higher dispersion in elliptical crack-dominated rocks, but a lower heterogeneity and lower dispersion in non-elliptical crack-dominated rocks.

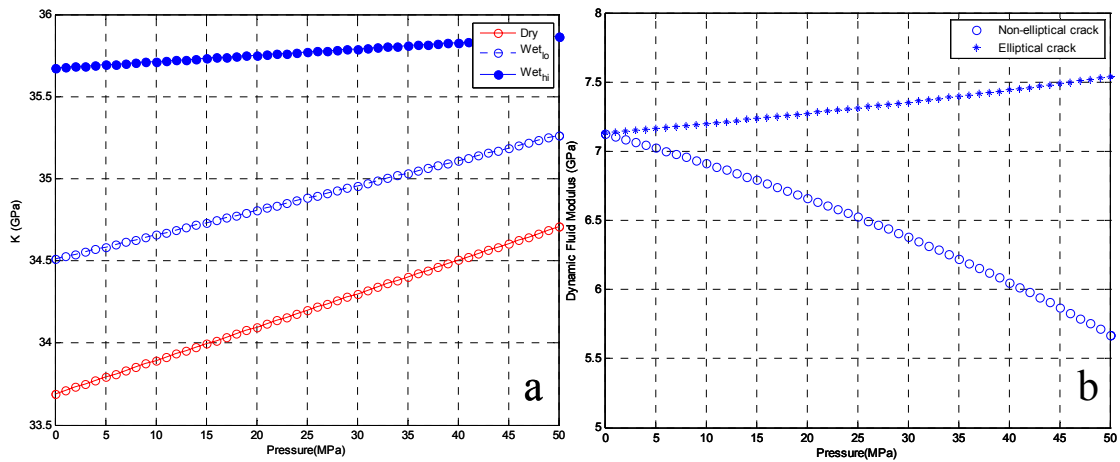


Figure 3.13 In a non-elliptical crack-dominated sandstone. a) Responding to increasing pressure, the dry and low frequency saturated bulk moduli increase much fast compared with elliptical cracked model (Figure 3.12a). b) Indicated by dynamic fluid modulus, increasing pressure results in lower heterogeneity. The results from elliptical crack model also plotted here for comparison. Calculated with equation 3.33-3.35.

From Figure 3.9, we pick up two most representative samples. Fontainebleau D represents the down-going trend and Delaware Light Grey represents the up-going trend. Their thin-sections are compared in Figure 3.14. From the images and thin-

section reports it is known that Fontainebleau D is clean sandstone, well sorted, with grain size between 150-200 microns. The so-called cracks in this sample are mainly formed by contacts between the quartz grains, which are well squeezed together. Although the resolution of the thin-section is not high enough to display the details of the crack geometry, there seems no reason to believe that the majority of the cracks having rounded end to form ellipse like cracks. To the contrary, the Delaware Light Gray sample has 7% clay content, poorly sorted, and grain size is around 300-500 microns. The dispersed clay and other small size minerals may infill some of the original tip ends between quartz grains, and change the overall geometry of the crack to more like an ellipse than tapered opening. The original deposition environment plus the diagenesis history constitute the fundamental difference between those two types of crack geometry, and govern their different response to the pressure.



Figure 3.14 Thin-sections for Fountaibleau D and Del Light Grey samples.

A similar analysis has also been performed on another dataset which includes eight tight gas sandstone samples. Again, a negative correlation between dynamic fluid modulus and porosity is observed (Figure 3.15a). Also, two types of heterogeneity vs. pressure trends exist in this relatively small dataset (Figure 3.15b). The thin-sections for two typical representative samples are shown in Figure 3.16.

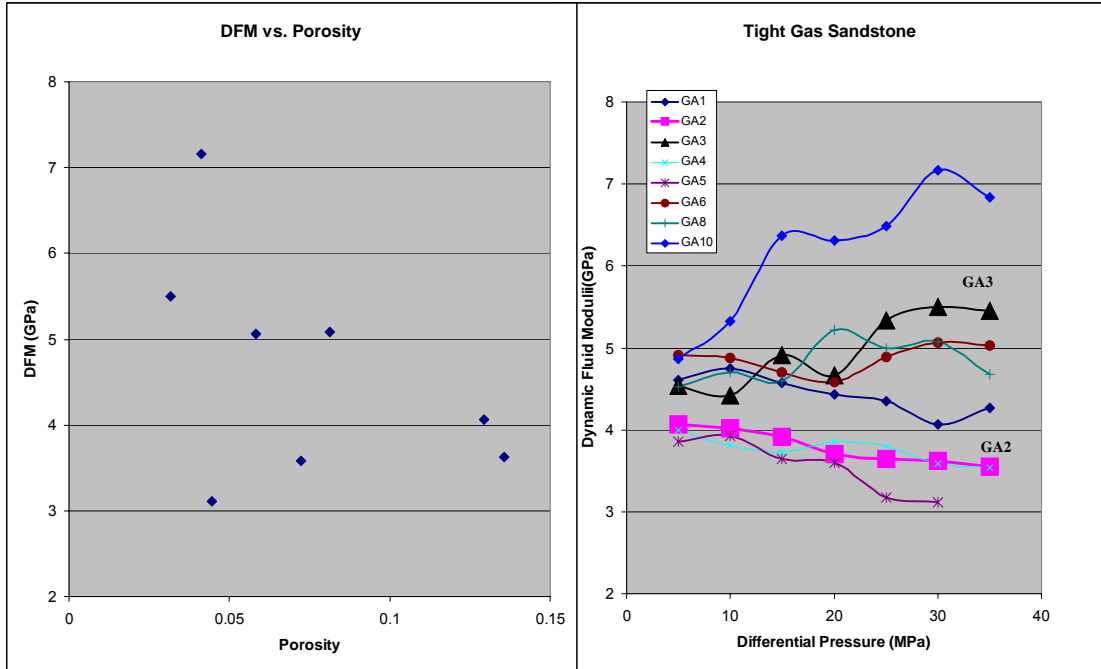


Figure 3.15 Tight gas sandstone: a) Left. Inverse correlation between dynamic fluid modulus and porosity. b) Right. Heterogeneity can either increase or decrease with the increasing pressure, depends on the crack geometry.

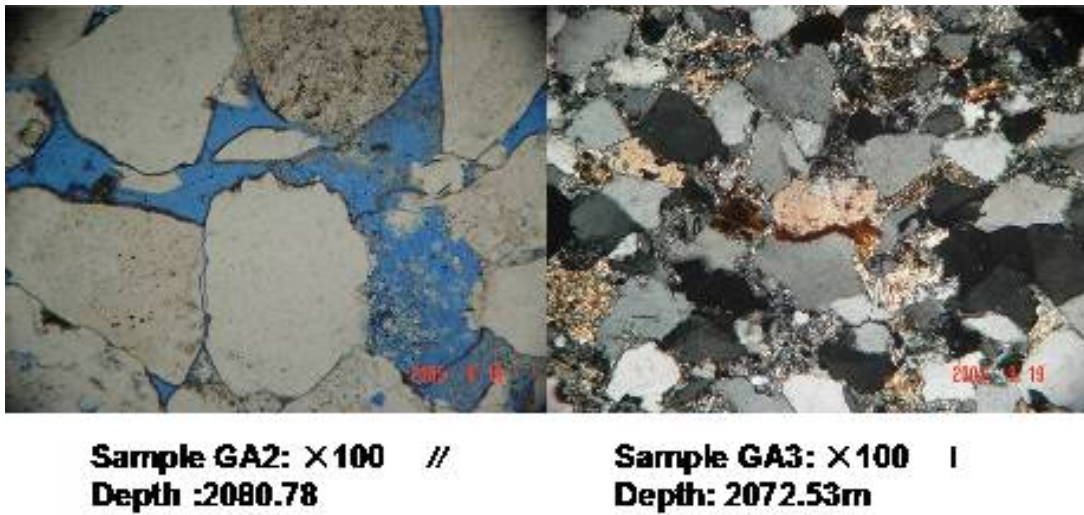


Figure 3.16 Thin-sections for sample GA2 and samples GA3 in Figure 3.15.

Note the above dataset are obtained from ultrasonic measurements, and the analysis is based on the unrelaxed pore pressure gradients between cracks and round pores. So the distinct pressure dependency of dynamic fluid modulus in two types of cracks should not be extended to low frequency cases like seismic data. For well-log data with an intermediate frequency, one needs be even more cautious in determining whether it belongs to the low frequency, high frequency or the transition zone. In the case of tight gas sandstone reservoirs, due to the nature of low permeability, one tends to believe that they fall into the high frequency regime. Furthermore, one must be aware that laboratory dry measurement may not have its counterpart in well-log data. In real subsurface conditions, the gas generation and migration process will only be able to replace the water in relatively permeable and large pore spaces. The capillary force in the tiny, thin crack space tends to retain the water inside the cracks. In a cracked tight rock with low total porosity, the fluid saturation effect is mainly contributed by the crack portion of the pore. Therefore under high frequency, even the large majority of the porosity is gas saturated, as long as the cracks are still water saturated and not be able to communicate to the surrounding round pore, the overall rock will behave not much different as a fully saturated rock. Based on this, it can then be speculated that in tight sandstones, the well-log P-wave velocities in gas zone should be comparable to a lab-measured saturated velocity.

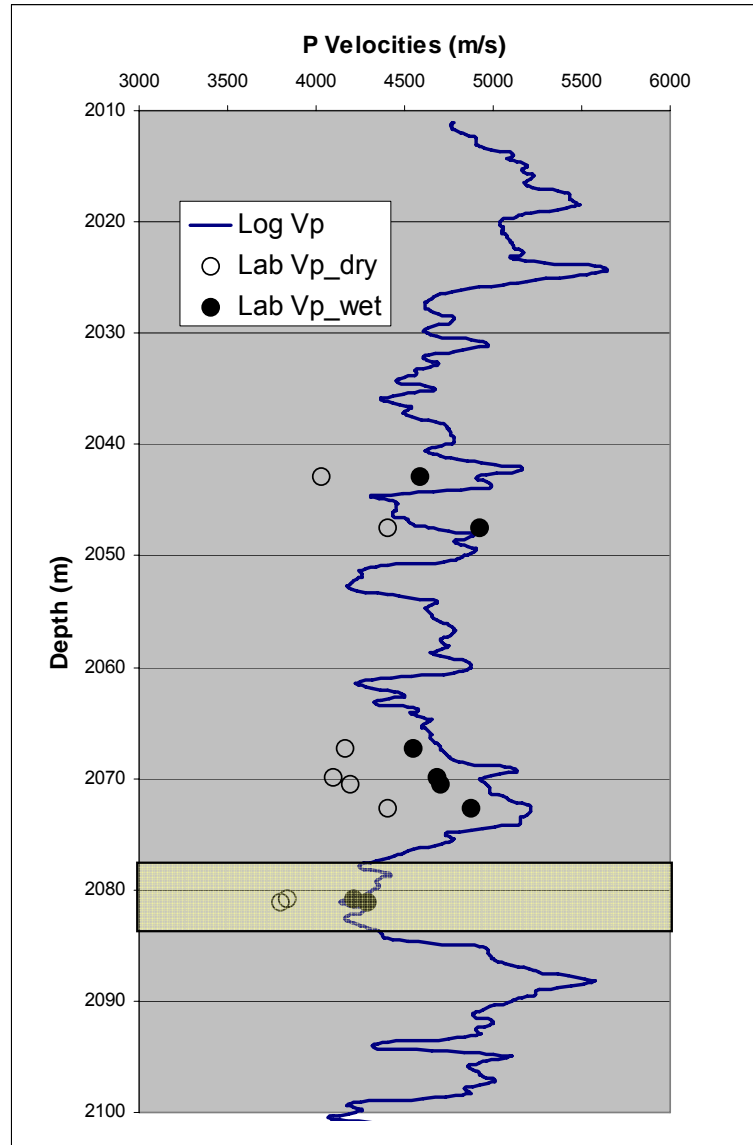


Figure 3.17 Comparison between well-log velocity and ultrasonic velocities for a tight gas sandstone reservoir.

Figure 3.17 is the P-wave velocity log, superimposed with the laboratory measured dry and fully saturated V_p for eight samples from the same well. Around 2080 m is the gas production zone with >80% gas saturation. It is clearly shown that the logging V_p is much high than the lab dry measured data. Indeed, it is almost equal

to the lab saturated data. This implies that due to high heterogeneity and high dispersion, it is not reliable to use velocity to estimate the fluid saturation in a low porosity but cracked reservoir. Actually in the above well-log (Figure 3.17), the lower velocity in the production zone is mainly caused by the porosity variation rather than the saturation variation.

3.8 Discussions

The most important equation in the discussion is equation (3.19), which can also be written in the form of compressibility rather than bulk modulus:

$$\beta' = \beta - \frac{q' / V_p}{dP_p} \quad (3.36)$$

Obviously the second term can be viewed as a modification to the compressibility of the virgin pore fluid, caused by the internal fluid flow across a boundary separating the different phases inside a REV. It has the same dimension as the compressibility. The appearance of dP_p seems making the whole term with an experiment parameter dependency. However, in the small strain linear domain, the fluid flow amount q' is always proportional to the applied pressure dP_c and the induced pore pressure increment dP_p ; therefore in any final analytical expression of the dynamic fluid compressibility, the dP_p will not appear at all, just like in equation 3.23.

Although the name “dynamic fluid modulus” is used to account for the dispersion and attenuation associated with WIFF (wave-induced fluid flow), it must be pointed out that it is just an equivalent concept, and the dispersion and attenuation are actually not caused by changing property of the fluid but rather caused by the heterogeneity. This heterogeneity can either be on the solid frame (like crack-pore model or double-porosity model), or on the fluid (patchy model). One should think this dynamic fluid modulus as an indicator of the heterogeneity.

Alternatively, the analysis could be done in terms of a dynamic pore modulus (Thomsen, 2010). An advantage of the present approach is that it converges at low frequency to the classic Gassmann result ("unrefined").

In ultrasonic measurements, the Biot global flow mechanism may have a non-negligible contribution to the total observed dispersions. Without quantitatively excluding this effect, our current interpretation using the dynamic fluid modulus has a tendency to attribute all observed dispersion to internal fluid flow. This will result in an overestimate on the heterogeneity of the rocks. It is important to be aware of this error and seek a correction in the future work.

3.9 Conclusions

Through poroelasticity analysis, we suggest to use a dynamic fluid modulus to link the bulk modulus dispersion to internal fluid flow, so that Gassmann’s equation is extended to non-Gassmann applications. The extension is successfully applied to

predict squirt flow dispersion. Multiple heterogeneities can be easily handled with the new method as being demonstrated in our examples.

Inverting for the dynamic fluid modulus from measured data provides us some new insights about the rock properties. In cracked low porosity rocks, an increasing compaction pressure can cause either more dispersion or less dispersion, probably due to whether the rock is dominated by elliptical or non-elliptical cracks.

3.10 References

Berryman J.G., 1999, Origin of Gassmann's equation: *Geophysics*, **64**, 1627-1629.

Berryman, J. G., and H. F. Wang, 1995, The elastic coefficients of double-porosity models for fluid transport in jointed rock: *Journal of Geophysical Research*, **100**, 24611 – 24627.

Berryman, J. G., 2003, Dynamic permeability in poroelasticity, Stanford Exploration Project Sponsor Report SEP-113, 443–454.

Biot, M. A., 1956a, Theory of propagation of elastic waves in fluid-saturated porous solid. I. Low frequency range: *Journal of the Acoustical Society of America*, **28**, 168–178.

———, 1956b, Theory of propagation of elastic waves in a fluid-saturated porous solid. II. Higher frequency range: *Journal of the Acoustical Society of America*, **28**, 179–191.

———, 1962, Mechanics of deformation and acoustic propagation in porous media: *Journal of Applied Physics*, **33**, 1482–1498.

Budiansky, B., and R. J. O'Connell, 1976, Elastic moduli of a cracked solid: *Int. J. Solids Structures*, **12**, 81-97.

———, 1980, Bulk dissipation in heterogenous media: *Solid Earth Geophys. and Geotech.*, **42**, 1-10.

Cheng, C.H., 1978, Seismic velocities in porous rocks: Direct and inverse problems: Sc.D. dissertation, Massachusetts Institute of Technology.

———, 1993. Crack models for a transversely anisotropic medium. *Journal of Geophysical Research*, **98**, 675–684.

Darcy, H., 1856. *Les Fontaines Publiques de la Ville de Dijon*. Paris: Dalmont. Dvorkin, J., G. Mavko, and A. Nur, 1995, Squirt flow in fully saturated rocks: *Geophysics*, **60**, 97–107.

Eshelby, J.D., 1957. The determination of the elastic field of an ellipsoidal inclusion, and related problems. *Proc. Royal Soc. London A*, **241**, 376–396.

Han, D., 1986, Effects of porosity and clay content on acoustic properties of sandstones and unconsolidated sediments: Ph.D. dissertation, Stanford University.

Hofmann, R., 2006, Frequency dependent elastic and anelastic properties of clastic rocks: Ph.D. dissertation, Colorado School of Mines

Hudson, J.A., 1980. Overall properties of a cracked solid. *Math. Proc. Camb. Phil. Soc.*, **88**, 371–384.

———, 1981. Wave speeds and attenuation of elastic waves in material containing cracks. *Geophysical Journal of the Royal Astronomical Society*, **64**, 133–150.

Kuster, G.T. and M.N. Toksöz, 1974. Velocity and attenuation of seismic waves in two-phase media. *Geophysics.*, **39**, 587–618.

Le Ravalec, M., and Y. Gueguen, 1996, High- and low-frequency elastic moduli for a saturated porous/cracked rock-Differential self-consistent and poroelastic theories. *Geophysics.*, **61**, 1080-1094.

Liu, H.P., D.L. Anderson, and H. Kanamori, 1976. Velocity dispersion due to anelasticity: implications for seismology and mantle composition. *Geophysical Journal of the Royal Astronomical Society*, **47**, 41–58.

Mavko, G., T. Mukerji, and J. Dvorkin, 2009, *The Rock physics handbook*: Cambridge University Press.

Mavko, G., and A. Nur, 1978. The effect of nonelliptical cracks on the compressibility of rocks. *J. Geophys. Res.*, **83**, 4459-4468.

Müller, T. M., B. Gurevich, and M. Lebedev, 2010, Seismic wave attenuation and dispersion resulting from wave-induced flow in porous rocks-A review, *Geophysics*, **75**, 75A147-75A164.

- Nur, A., 1971. Effects of stress on velocity anisotropy in rocks with cracks. *Journal of Geophysical Research*, **76**, 2022–2034.
- O’Connell, R. J., and B. Budiansky, 1974. Seismic velocities in dry and saturated cracked solids. *J. Geophys. Res.*, **79**, 4626–4627.
- , 1977, Viscoelastic properties of fluid-saturated cracked solids: *Journal of Geophysical Research*, **82**, 5719–5740.
- Pride, S. R., and J. G. Berryman, 2003a, Linear dynamics of double-porosity and dual-permeability materials. I. Governing equations and acoustic attenuation: *Physical Review E*, **68**, 036603.
- , 2003b, Linear dynamics of double-porosity and dual-permeability materials. II. Fluid transport equations: *Physical Review E*, **68**, 036604.
- Skempton, A. W., 1954, The pore-pressure coefficients A and B: *Geotechnique*, **4**, 143–147.
- Tang, X., 2011, A unified theory for elastic wave propagation through porous media containing cracks- An extension of Biot’s poroelastic wave theory: *Science China—Earth Sciences*, **54**, 1441– 1452.
- Tang, X., X. Chen, and X. Xu, 2012, A cracked porous medium elastic wave theory and its application to interpreting acoustic data from tight formations: *Geophysics*, **77**, 245-252
- Tang, X., and C. H. Cheng, 1989, A dynamic model for fluid in open borehole fractures: *Journal of Geophysical Research*, **94**, 7567-7576.
- , 2004, *Quantitative borehole acoustic methods*: Elsevier Science Publishing Co,
- Thomsen, L., 1985, Biot-consistent elastic moduli of porous rocks: low-frequency limit, *Geophysics*, **50**, 2797-2807.
- , 2010, On the fluid dependence of rock compressibility: Biot-Gassmann refined: *SEG Expanded Abstracts*, **80**, 2447-2451.
- Walsh, J.B., 1965. The effect of cracks on the compressibility of rock: *Journal of Geophysical Research*, **70**, 381-389
- White, J. E., 1975, Computed seismic speeds and attenuation in rocks with partial gas saturation: *Geophysics*, **40**, 224–232.

3.11 Appendix A

In this appendix, we present another approach to reach the definition of “dynamic fluid modulus”, different from the intuitive way presented in the main context.

Following the concise and elegant notation in Berryman (1999), and further reducing it to only consider hydrostatic stress and strain, the elastic behavior of a porous media filled with fluid can be described as:

$$\varepsilon = a_{11}\sigma + a_{12}p \quad (\text{A1})$$

$$\xi = a_{21}\sigma + a_{22}p \quad (\text{A2})$$

Here ε is bulk strain, ξ is fluid change normalized to bulk volume, σ is total external stress increment, and p is the pore pressure increment. Coefficients a_{ij} are related to grain bulk modulus K_o , dry bulk modulus K_d , porosity ϕ , and fluid modulus K_f in:

$$a_{11} = 1/K_d \quad (\text{A3})$$

$$a_{12} = a_{21} = 1/K_d - 1/K_o \quad (\text{A4})$$

$$a_{22} = a_{21} / B \quad (\text{A5})$$

$$B = M + \frac{\alpha^2}{K_d}$$

$$M = \frac{\alpha - \phi}{K_o} + \frac{\phi}{K_f}$$

$$\alpha = 1 - \frac{K_d}{K_o}$$

Here B is called Skempton coefficient (Skempton 1954), and α is the Biot-Willis coefficient.

If boundary is closed, $\zeta=0$, from A2 one obtains

$$p = -\frac{a_{21}}{a_{22}}\sigma \quad (\text{A6})$$

Substituting this p into A1 gives

$$\varepsilon = \left(a_{11} - \frac{a_{12}^2}{a_{22}}\right)\sigma \quad (\text{A7})$$

Since we are looking for a relationship $\varepsilon = \sigma / K_{sat}$, it is obviously

$$K_{sat} = \frac{1}{\left(a_{11} - \frac{a_{12}^2}{a_{22}}\right)} \quad (\text{A8})$$

Using A3-A5, it is easy to prove A8 is equivalent to the Gassmann's equation in a more familiar expression:

$$K_{sat} = K_{dry} + \frac{\alpha^2}{\frac{\alpha - \varphi}{K_o} + \frac{\varphi}{K_f}} \quad (\text{A9})$$

Next we consider the non-closed boundary condition where $\zeta \neq 0$. A2 can be written as

$$0 = a_{21}\sigma + \left(a_{22} - \frac{\zeta}{p}\right)p \quad \text{or}$$

$$p = -\frac{a_{21}}{a_{22} - \frac{\zeta}{p}}\sigma \quad (\text{A10})$$

Again, substituting this p into A1 gives us:

$$\varepsilon = \left(a_{11} - \frac{a_{12}^2}{a_{22} - \frac{\xi}{p}} \right) \sigma \quad (\text{A11})$$

Comparing between A11 and A7, it can be seen that the difference is only on the denominator of second term. Recalling the definition of a_{22} in A5, one can write this denominator as

$$a_{22} - \frac{\xi}{p} = M + \frac{\alpha^2}{K_d} - \frac{\xi}{p} = \frac{\alpha - \varphi}{K_o} + \frac{\varphi}{K_f} + \frac{\alpha^2}{K_d} - \frac{\xi}{p}$$

The first and third terms at right-hand side are only related to dry and grain properties; only second term contains fluid information. So if one wants to attribute the last term, which is caused by fluid flow, into an effective fluid modulus, one needs rewrite the above as

$$a_{22} - \frac{\xi}{p} = \frac{\alpha - \varphi}{K_o} + \left(\frac{\varphi}{K_f} - \frac{\xi}{p} \right) + \frac{\alpha^2}{K_d} = \frac{\alpha - \varphi}{K_o} + \varphi \left(\frac{1}{K_f} - \frac{\xi}{\varphi p} \right) + \frac{\alpha^2}{K_d} \quad (\text{A12})$$

From here it can be seen, if one defines

$$\frac{1}{K_f'} = \frac{1}{K_f} - \frac{\xi}{\varphi p} \quad (\text{A13})$$

Then A12 can be rewritten into

$$a_{22} - \frac{\xi}{p} = \frac{\alpha - \varphi}{K_o} + \frac{\varphi}{K_f'} + \frac{\alpha^2}{K_d} = M' + \frac{\alpha^2}{K_d} = a_{22}' \quad (\text{A14})$$

So that A11 can be rewritten into

$$\varepsilon = (a_{11} - \frac{a_{12}^2}{a_{22}})\sigma \quad (\text{A15})$$

It is in the exact same format of A7, with only a_{22} replaced by a_{22}' . With the same reasoning from A7 to A9, one can get the final Gassmann-like expression of the saturated bulk modulus for a non-closed system:

$$K_{sat} = K_{dry} + \frac{\alpha^2}{\frac{\alpha - \varphi}{K_o} + \frac{\varphi}{K_f'}} \quad (\text{A16})$$

In which the dynamic fluid modulus K_f' is defined by A13.

Since ξ is define as fluid change normalized to bulk volume V_b , it is related to the absolute fluid flow amount q by $\xi = q/V_b$. In addition, the pore volume V_p relates to bulk volume by $V_p = \varphi V_b$. So that A13 can also be written as

$$\frac{1}{K_f'} = \frac{1}{K_f} - \frac{q/V_b}{\varphi p} = \frac{1}{K_f} - \frac{q/V_p}{p} \quad (\text{A17})$$

A17 is exactly the same as the equation 3.2 in main context.

4 LABORATORY MEASUREMENT OF DISPERSION AND ATTENUATION AT SEISMIC FREQUENCY: PRINCIPLES AND LIMITATIONS

4.1 Introduction

A low frequency measurement system is essential for the study of velocity dispersion and attenuation in two aspects:

First, the traditional laboratory measurements of the velocities in reservoir rocks are conducted in MHz frequency range. Sonic well-logs are in 10 kHz and surface seismic in several Hz to hundred Hz. Today's challenging exploration requires us to utilize all types of data for a better integrated quantitative interpretation. However, the velocity dispersion between those widely separated frequency ranges makes the integration difficult. Many theories have been developed to understand the various dispersion and attenuation mechanisms, and many models have been proposed to estimate the dispersion and attenuation from other rock properties. But all of the theories and models haven't received strong support from real measured data. The biggest issue is that acoustic velocities in seismic frequency cannot be directly measured in laboratory.

Second, recent theoretical works reveal that the dispersion and attenuation in reservoir rock is closely related to the interaction between pore fluid and rock frame. This suggests that the measured dispersion and attenuation data contain important information about both the rock and fluid. It is possible to dig some fluid indicators out of the

dispersion and attenuation analysis. Before any such attempt can be applied to field data, there is a need to collect sufficient lab test results to establish some robust relationships.

The early laboratory evidences of velocity dispersion are indirectly inferred from discrepancies between measured ultrasonic velocities and low frequency Gassmann predictions (e. g., Gregory, 1976; Domenico, 1976; Gist, 1994). Murphy *et al.* (1984) combined ultrasonic velocity measurements with imaging techniques, including optical, SEM, and X-ray microscopy to relate the velocity dispersion to the centimeter scale heterogeneities. Attenuation is also obtained from ultrasonic data using spectral ratio method (Toksöz *et al.*, 1978) and Weiner filtering method (Tang *et al.*, 1987). Although those early attempts gave robust evidences to the existence of dispersion and attenuation in sedimentary rocks at ultrasonic frequency, it is not appropriate to directly transfer or apply that knowledge to well-log or seismic data due to the large frequency differences among those data sets. Theories on dispersion and attenuation mechanisms suggest they are highly frequency dependent properties.

Efforts must be made to directly measure the velocities and attenuation in those frequency ranges. Winkler and Nur (1982) used resonance-bar technique to measure the P-wave attenuation in sandstone at frequencies from 0.5 to 9 kHz, and found they are mainly caused by the partial saturation. Murphy (1982, 1984) and Yin *et al.* (1992) continued the efforts with resonance-bar and expand the frequency range slightly wide into 0.3-14 kHz, making their results more meaningful to the well-log data interpretation.

However, constrained by the size and geometry of the sample, it is impossible to extend the measurement into seismic frequency range in resonance-bar method.

The force-deformation (stress-strain) method is the only possible technique to measure the elastic and viscoelastic properties in seismic frequency range. This method was originally designed and widely used in material science and mechanical engineering study for measuring the static elastic constants of solid material (e. g., Czichos *et al.*, 2006). It was then developed into stress-strain hysteresis techniques to dynamically measure the frequency dependent elastic constants, as well as the attenuation in granite and other anelastic solids (McKavanagh and Stacey, 1974; Peselnick *et al.*, 1979). Spencer (1981) first successfully managed the measurements with strain amplitude around 10^{-6} and frequency below 100Hz in dry and water saturated sandstone, limestone and granite. His results show strong dispersive modulus and frequent dependency of Q^{-1} in water saturated samples but not in dry samples. Liu *et al.* (1983) discussed the difficulties and challenges to carry out such experiments under small amplitude meaningful to in-situ seismic applications. The techniques were further developed by Batzle and his group in the Colorado School of Mines (Gautam, 2003; Batzle *et al.*, 2006; Adam *et al.*, 2009; Das, 2009), who obtained and published several sets of seismic frequency velocities and attenuation data from various reservoir rocks.

Our low frequency measurement system will follow the same stress-strain hysteresis measurement principles used by Spencer (1981), Liu *et al.* (1983) and Batzle *et al.* (2006).

4.2 Measurement principle: Force-deformation

In this section, I try to present the principles how velocity dispersion and wave attenuation is measured in seismic frequency band, and discuss the system design guidelines.

4.2.1 Dispersion: Young's modulus and Poisson ratio

In conventional laboratory velocity measurements, ultrasonic transducers (MHz) are used to generate a transit acoustic wave pulse. The wavelength of this pulse is in mm range and much smaller compared with the typical core sample length. Another transducer at the other end of the sample can record the arriving pulse, pick its “first arrival” and determine the total travel time of the transient pulse. The velocity V is obtained by sample length s divided by the time of flight t .

$$V = s / t \quad (4.1)$$

If the frequency goes to seismic range (1-100Hz), the corresponding wavelength falls into tens to thousands of meters. It is much larger than a core sample can be. A transient wave and first arrival pick up method is obviously not feasible anymore (Figure 4.1).

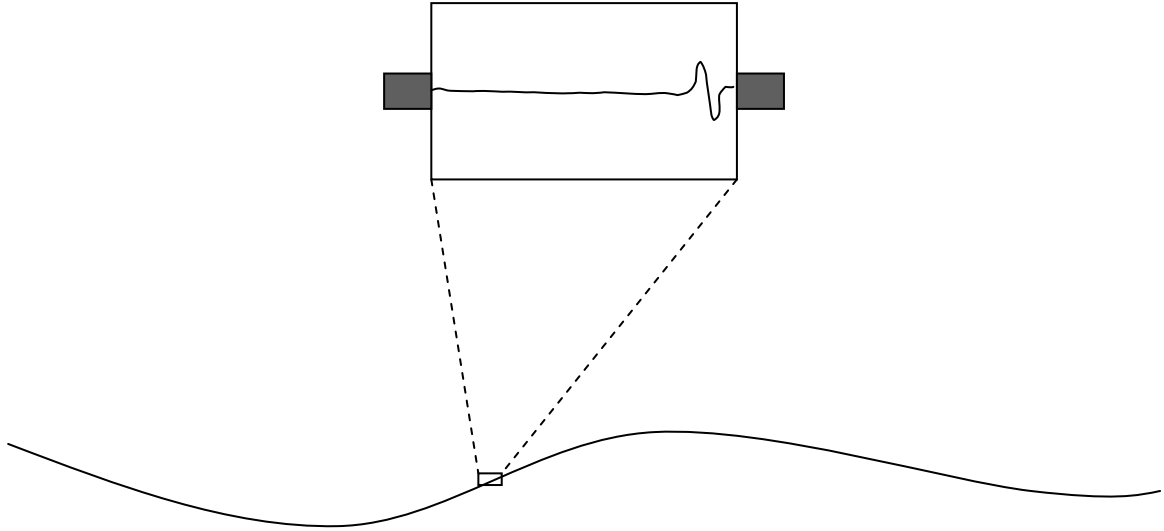


Figure 4.1 In ultrasonic measurement, the wavelength is much smaller than the sample size, but for seismic frequency, the wavelength is much larger than the typical core sample, making it impossible to use pulse transient wave and first arrival pick up method to measure velocity.

The principle of the low frequency measurement is based on the Hooke's Law (stress strain relationship). The elastic constants rather than the velocities are measured directly. In isotropic media, there are only two independent elastic constants. To utilize the well-established strain gage measurement techniques we choose the Young's modulus E and Poisson ratio ν . Figure 4.2 is the schematic setup of the experiment. A sinusoid stress field is applied vertically to the core sample. Two sets of strain gages are attached to the surface of sample vertically and horizontally, and will measure the strain parallel to stress $\varepsilon_{||}$ and perpendicular to stress ε_{\perp} . The Young's modulus and Poisson ratio are obtained as:

$$E = \frac{\sigma}{\varepsilon_{||}} \quad \text{here } \sigma \text{ is the vertical stress.} \quad (4.2)$$

$$\nu = \frac{\varepsilon_{\perp}}{\varepsilon_{\parallel}} \quad (4.3)$$

They can be easily converted into bulk modulus K , and shear modulus G by:

$$K = \frac{E}{3(1-2\nu)} \quad (4.4)$$

$$G = \frac{E}{2+2\nu} \quad (4.5)$$

With separated measured density ρ , we can compute the compressional wave velocity V_p and shear wave velocities V_s are computed as:

$$V_p = \sqrt{\frac{K + \frac{4}{3}G}{\rho}} \quad (4.6)$$

$$V_s = \sqrt{\frac{G}{\rho}} \quad (4.7)$$

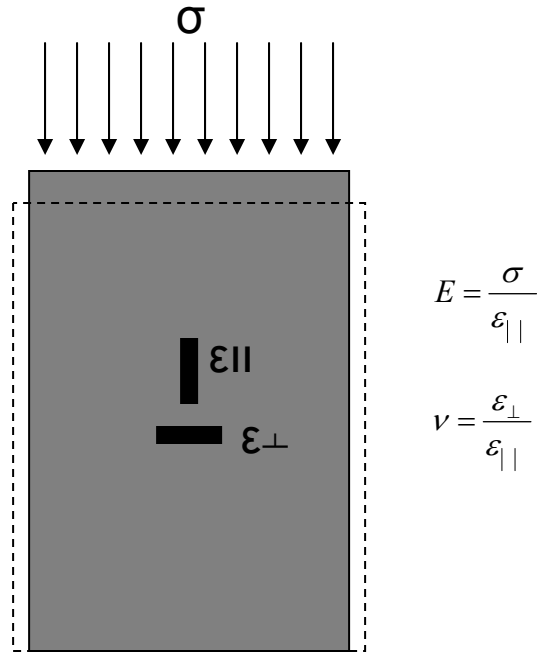


Figure 4.2 Principles for using stress strain relationship to measure elastic moduli of solid sample.

4.2.2 Attenuation: phase difference

When the strain level is small enough, disregarding the specific physical attenuation mechanism, the viscoelastic behavior in a solid can always be described using a “standard linear solid model” (Zener, 1948; Liu *et al.*, 1976). It is a phenomenological model to relate the stress σ and strain ε as:

$$\sigma + \tau_{\sigma} \dot{\sigma} = M_R (\varepsilon + \tau_{\varepsilon} \dot{\varepsilon}) \quad (4.8)$$

Where M_R is relaxed elastic modulus, τ_{σ} is the stress relaxation time under constant strain and τ_{ε} is the strain relaxation time under constant stress.

Under a sinusoidal stress field

$$\sigma(t) = \sigma_o \exp[i(\omega t - kx)]$$

The stress is related to strain with a complex modulus M_c :

$$\sigma(t) = M_c \varepsilon(t) = \frac{M_R}{A - iB} \varepsilon(t) \quad (4.9)$$

where

$$A = 1 - \frac{\omega^2 \tau_\varepsilon^2}{1 + \omega^2 \tau_\varepsilon^2} \left(1 - \frac{\tau_\sigma}{\tau_\varepsilon}\right)$$

$$B = \frac{\omega(\tau_\varepsilon - \tau_\sigma)}{1 + \omega^2 \tau_\varepsilon^2}$$

From 4.9 it can be noted that the strain is out of phase to the stress, and a hysteresis loop is formed (Figure 4.3). The area inside the elliptical loop represents the energy loss in one cycle of stress-strain disturbance. When the phase difference between strain and stress is zero, the loop reduces to a straight line and no energy loss will occur.

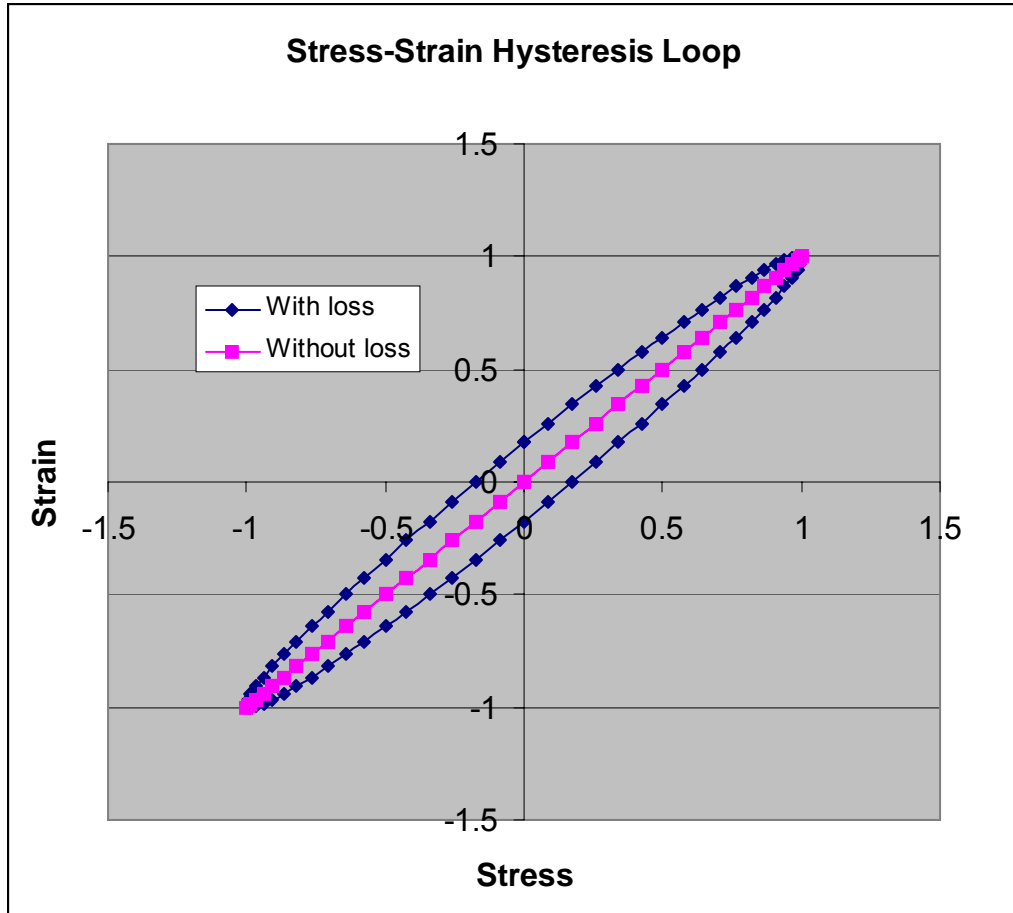


Figure 4.3 Stress-strain hysteresis loop, caused by the phase difference between stress and strain. The area inside the elliptical loop represents the energy loss in one cycle of stress-strain disturbance. When the phase difference between strain and stress is zero, the loop reduces to a straight line and no energy loss will occur.

The attenuation is typically quantified with an inverse quality factor $1/Q$ which is defined as

$$1/Q = \frac{1}{2\pi} \frac{\Delta W}{W} \quad (4.10)$$

W is the elastic strain energy per unit cycle and ΔW is the energy dissipated per unit cycle. It is proved that under small attenuation, the inverse quality factor equals to the tangential of the phase difference between strain and stress θ (White, 1983; Paffenholz and Burkhardt, 1989):

$$1/Q = \tan(\theta) \quad (4.11)$$

So experimentally the phase of the stress and strain can be measured separately and the quality factor of the sample material can be calculated using 4.11.

What is measured here is actually the quality factor for Young's modulus Q_E . The quality factor for P and S wave can be obtained using the following relationships (Gautam, 2003):

$$\frac{1}{Q_S} = \frac{1}{Q_E} - \frac{\nu}{1+\nu} \tan(\theta_\nu) \quad (4.12)$$

$$\frac{(1-2\nu)(1-\nu)}{Q_P} = \frac{1+\nu}{Q_E} - \frac{2\nu(2-\nu)}{Q_S} \quad (4.13)$$

θ_ν is the phase difference between Poisson's gage (horizontal) and Young's gage (vertical), which can also be obtained from measurements.

In reality, we do not measure the stress directly. Instead, a standard aluminum core plug is stacked with the rock sample, and the strains on the standard are measured (Figure 4.4). Since the aluminum standard and rock sample are subject to the same stress field, the ratio of their strains should be equal to the reverse ratio of their Young's modulus.

$$E_{sample} = E_{std} \frac{\epsilon_{std}}{\epsilon_{sample}} \quad (4.14)$$

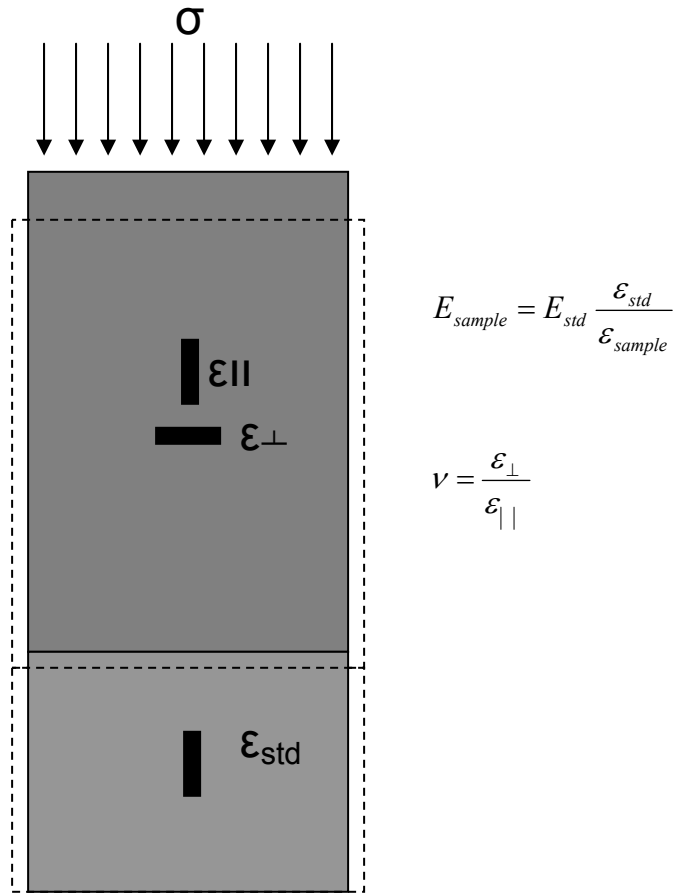


Figure 4.4 Using a standard material with known Young’s modulus to stack with sample, the relative measurement eliminate the need to measure stress or force with different sensors and electronics system; therefore reduces the systematic error.

Also, aluminum can be viewed as pure elastic medium, so the phase of the strain should equal to the phase of the stress. There are several advantages in such relative strain measurement method to the direct stress and strain measurement. First, it is difficult to find a good stress or force sensor satisfying the measurement range and resolution requirements in our application. Second and more important, a stress or force

sensor will use totally different set of electronic instrument to the strain measurement system. Each electronic system has its own system and random errors. Both the amplitude and phase can have different frequency responses in two systems. This makes the calibration between two systems very difficult. However, in our relative strain measurement approach, every measurement is under the same physical mechanism, with same electronic device and instrument, under same acquisition and processing procedures. This will significantly reduce both the system and random errors and increase the consistency.

While the physical principles are fairly straight forward, the engineering challenges to fulfill those principles are very high. I will discuss couple of major issues and present our solutions to them in next chapter.

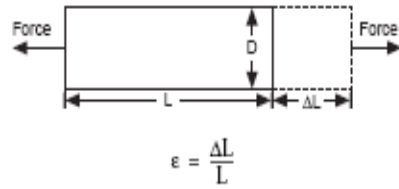
4.3 Data acquisition

4.3.1 Strain gage

A strain gage is basically a small piece of filament, with its electrical resistance changing with the strain (Figure 4.5). It is characterized by its gage factor GF, defined as the ratio of relative resistance change to the strain (relative length change).

$$GF = \frac{\Delta R/R}{\Delta L/L} = \frac{\Delta R/R}{\varepsilon} \quad (4.15)$$

It represents the sensitivity of the strain gage. A typical metal foil gage has a GF value of 2 to 5. To achieve high sensitivity in very small strain measurement, one needs use semiconductor strain gage, which has GF values above 100.



$$GF = \frac{\Delta R / R}{\Delta L / L} = \frac{\Delta R / R}{\epsilon}$$

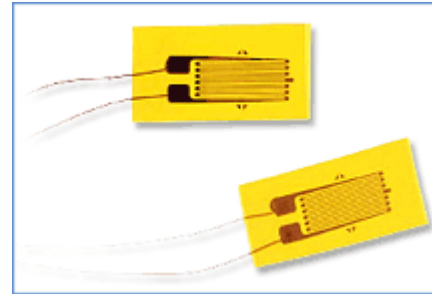
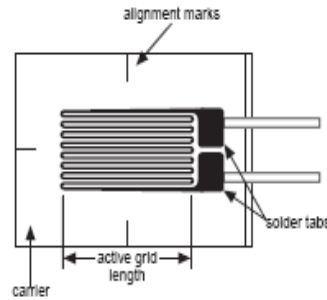


Figure 4.5 Strain gage: deformation of length (strain) is reflected in the relative change of resistivity, which can be measured electronically.

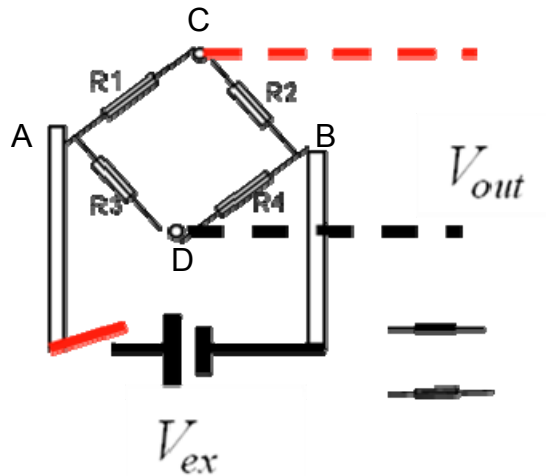
4.3.2 Wheatstone bridge

The most common strain gage measurement involves a Wheatstone bridge arrangement, which consists of resistors (Figure 4.6). Two of them are standard precision resistors (R_2 , R_3), and the other two are strain gages (R_1 , R_4), with the nominal resistance (at zero strain) equal to the standard resistors. An excitation voltage V_E is applied across points A and B. When the bridge is fully balanced, the output voltage across C and D is zero. If the resistance of strain gage changes with the strain

$$dR = R * GF * \epsilon \tag{4.16}$$

When one assumes that $R_1=R_2=R_3=R_4=R$ and $dR_1=dR_4=dR$, then the voltage across the C and D can be written as

$$dV_o = -V_E \frac{1}{2R} dR = -\frac{1}{2} V_E * GF * \varepsilon \quad (4.17)$$



$$V_{out} = V_{ex} \frac{1}{\frac{1}{\varepsilon * \frac{GF}{2}} + 1}$$

$$V_{out} = V_{ex} \cdot \varepsilon \cdot \frac{GF}{2}$$

Figure 4.6 Schematic of a Wheatstone bridge consists of two standard resistors and two strain gages.

To mimic the far field seismic condition, the strain level must be controlled below 10^{-6} . Limited by the power of stress source, the strain generated in a real measurement can even be 1 to 2 orders smaller than that. As its consequences, the strain gage Wheatstone bridge output is in micro-volt range. It can be easily contaminated by environmental electromagnetic noise, which may be 100 times higher than the signal. Special cares have to been taken on hardware (wiring, shielding, grounding), AD conversion (high resolution), and software (signal processing, and measurement automation). Because the measurement results are highly relied on the amplitude and phase, a lock-in amplifier technique is implemented to accurately retrieve the signal.

4.3.3 Lock-in amplifier

A lock-in amplifier is a type of amplifier that can extract a signal with known frequency from an extremely noisy environment. Although it is conventionally called an amplifier, actually it does not amplify the signal, but just retrieve the amplitude and phase of the signal out. This is achieved in two major steps. The important requirement on the signal for a lock-in amplifier to work is that its frequency is known. The procedures are shown in Figure 4.7.

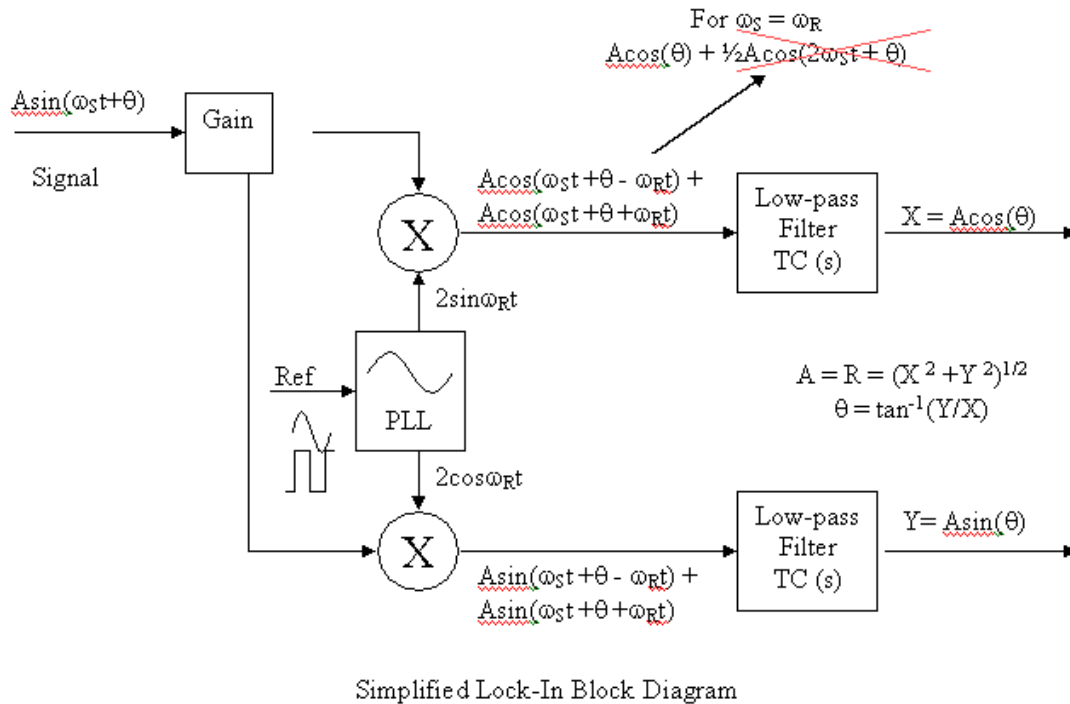


Figure 4.7 The principles of a lock-in amplifier.

In first step, a reference signal with this known frequency ω_R is fed into an internal reference synthesizer that extracts frequency and phase information from the reference signal and generates a pure sine wave. That sine wave is then multiplied with the input signal. For each frequency component in the input signal, the mixer generates

two output terms: one with the frequency equals to the difference between the frequencies of the internal reference and the signal component ($\omega_R - \omega_S$) and the other one equals to the sum of the two frequencies ($\omega_R + \omega_S$). For the component of the input signal with the frequency equals to that of the internal reference ($\omega_S = \omega_R$), the first mixer term will have frequency equals to 0 (a DC signal) and the second mixer term will have frequency equal to twice the reference frequency ($2\omega_R$).

In second step, a low-pass filter that follows the mixer should ideally reject everything but the DC component, which is proportional to the amplitude of the signal component at the ω_R and the cosine of its phase relative to the phase of the internal reference ($A \cdot \cos(\theta)$). This quantity is referred to as “X.” If the same process, mixing and filtering, is applied using a pure cosine wave at ω_R , quantity “Y” will be generated. Y is proportional to the amplitude of the signal component times the sine of the phase shift ($A \cdot \sin(\theta)$). From these two quantities, the amplitude A and relative phase θ of the input signal can be determined.

$$\begin{aligned} A &= \sqrt{X^2 + Y^2} \\ \theta &= \arctan(X/Y) \end{aligned} \quad (4.18)$$

For any noises with the frequency not equal to the reference frequency, both the first and second mixer terms will have a non-zero frequency, and will be removed by the filter.

In the measurements, the deformation of the sample is generated by a well controlled vibration source. The frequency of the vibration is exactly known because it is driven by a function generator and a power amplifier. Therefore the lock-in amplifier fits very well with this application.

4.4 System as a whole

Figure 4.8 is the schematic of the overall measurement system. Besides the force-deformation mechanism and data acquisition discussed above, the sample has to be placed in a pressure vessel, so that both confining pressure and pore pressure can be applied to the sample. This is essential since one of the goals here is to evaluate the fluid flow related wave attenuation and velocity dispersion, so the fluid saturation within the rock sample must be controlled. The confining pressure is supplied by a compressed nitrogen cylinder with a pressure regulator. Currently the maximum pressure can reach 6000 psi. The pore pressure is supplied and controlled by a digital pump, with various fluids as desired by experiment specific purposes.

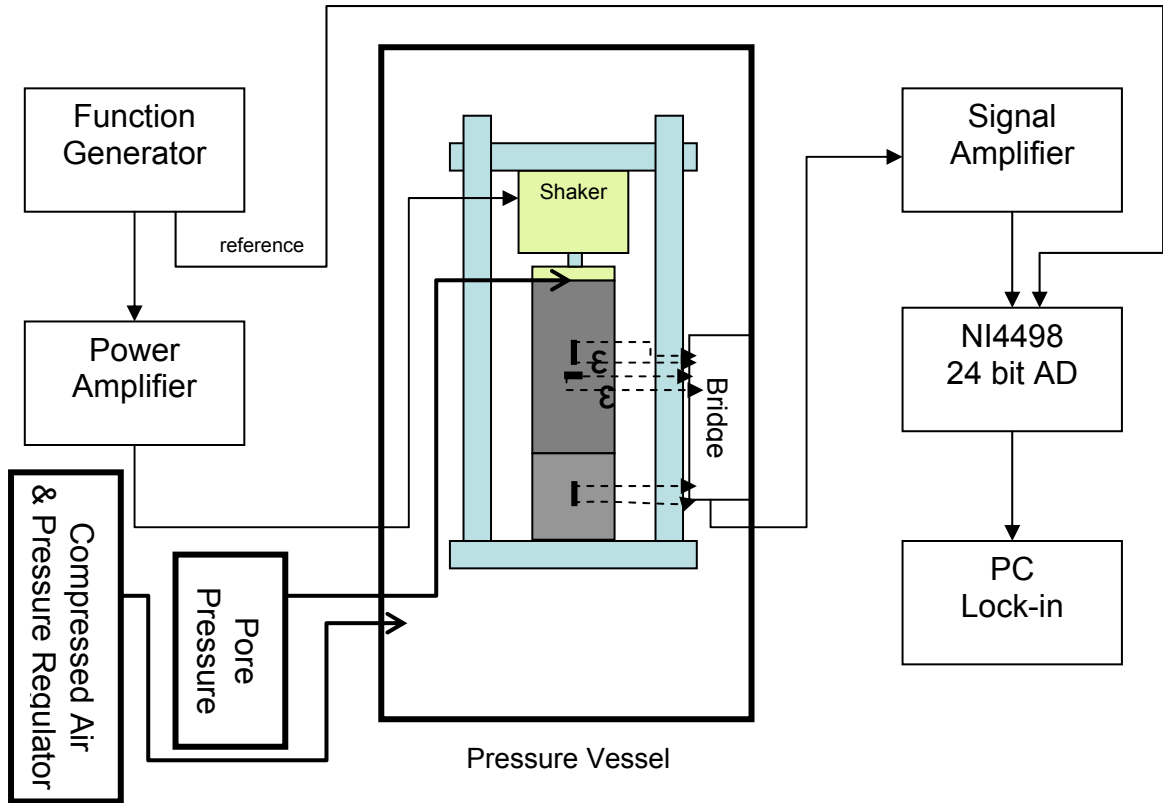


Figure 4.8 Schematic for low frequency measurement system.

Under predefined confining pressure, pore pressure and saturation conditions, the function generator sends out a continuous harmonic voltage wave, with its frequency and amplitude specified by user, through PC program. This voltage signal is supplied to a linear power amplifier to obtain a harmonic current wave, with desired current level. The current is used to drive a speaker like shaker to generate a harmonic mechanical vibration. The rock specimen and standard aluminum are deformed by the vibration from the shaker. Both axial and radial strains are detected dynamically by the strain gages attached to the surfaces of samples and standard aluminum. The Wheatstone bridges output voltage waveforms to a special weak signal amplifier. The amplified waveforms are fed into a 24 bits multi channel AD converter. In the meanwhile, the original

harmonic voltage wave from the function generator is also fed into the AD converter. This waveform will be used as reference signal in lock-in amplifier.

After the AD converter, the digitized waveforms from each measurement channel, along with the reference signal, are sent to a PC program for real-time processing, recording, and display. The most significant task of the processing is retrieve the amplitude and phase of the dynamic strain for each channel using lock-in amplifier. The results of the lock-in amplifier are used to calculate the Young's modulus, Poisson ratio, and quality factor of measured sample.

Above is the procedure of the measurement at one frequency. The actual measurement has to cover multiple points in a frequency range to analyze the frequency dependent behavior. A program is developed to automatically fulfill this goal. Figure 4.9 is the flow chart of this program. Users can input a desired frequency range and measurement points. Based on those inputs, the program will calculate a list of frequency points in a manner that they are evenly distributed on logarithm scale. A loop structure guides the system to run through each frequency point for necessary measurement operations. Results from each measurement point are displayed on computer monitor literally in a real-time manner, to build a live curve, exhibiting the frequency dependency of various sample properties like Young's modulus, Poisson ratio, and inverse quality factor. Figure 4.10 is a screen shot of a typical measurement running on its way.

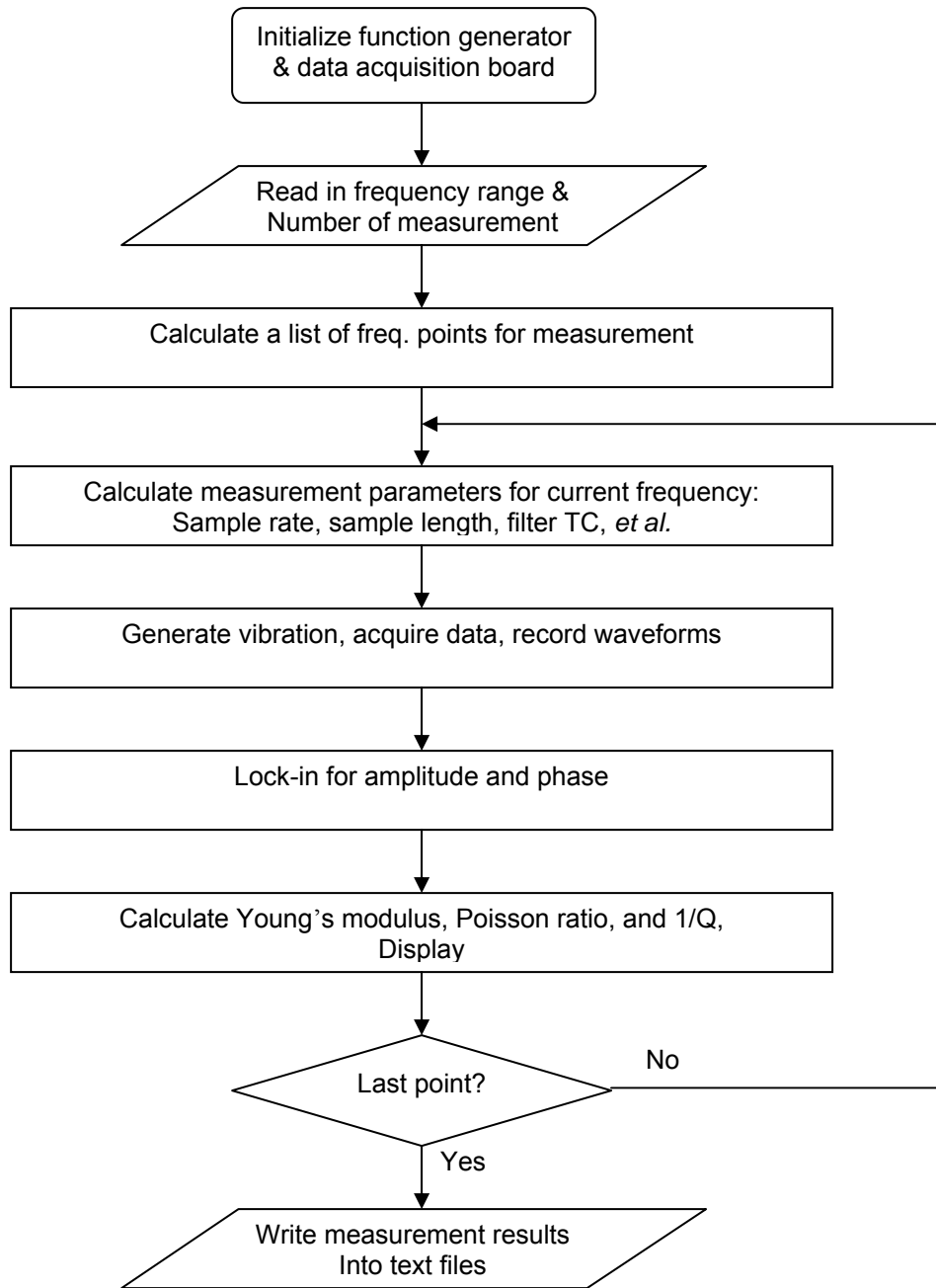


Figure 4.9 Program flow chart for automatic measurement through a range of frequencies inputted by users.

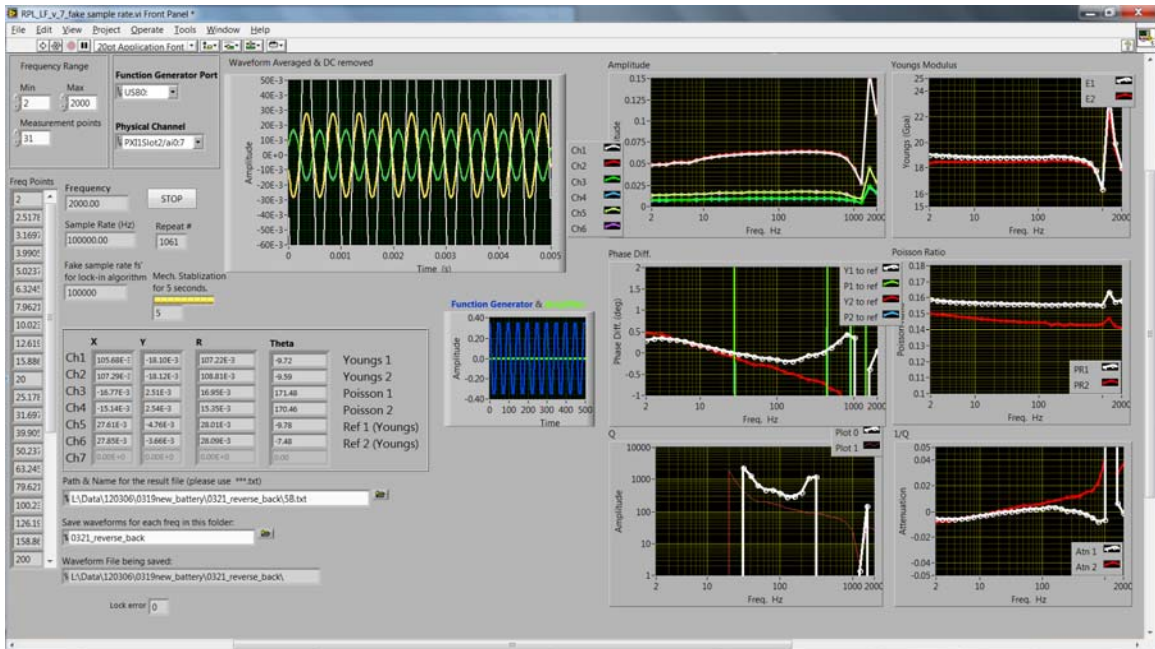


Figure 4.10 Screen shot of a live measurement.

The lock-in results, as well as the original waveforms, from each channel are stored as text data files on computer storage device. They are easy to be input to other tools for further analysis.

4.5 Limitation

While wishing the low frequency measurement system providing us with new observations to enhance our understanding of the attenuation and dispersion mechanism in sedimentary rocks, it is also important to recognize the limitations of the system. Just like any other physical measurement apparatus, the limitations mainly come from its measurement principles, but also are affected by design and fabrication qualities, and experiment operations.

4.5.1 Frequency range

A relatively stable strain level has to be maintained in a frequency range as wide as possible, to ensure the performance of the apparatus. When the strain level goes too low ($<10^{-8}$), the signal-noise ratio is also too low to retrieve the amplitude and phase. In the other end, a higher strain level ($>10^{-6}$) is unrealistic to mimic the subsurface phenomenon due to seismic wave disturbance.

The low frequency limit is controlled by the performance of the power amplifier and vibration generator. The manufacturer specifications determine the frequency range in which each device has linear performance. Figure 4.11 is the frequency response of the acceleration peak for the B&K 4810 Small Vibration Exciter, which is used as the vibration generator in our system. It shows that the amplitude begins to decrease when the frequency goes below around 70 Hz. Although we have managed to compensate this amplitude drop at low frequency by increasing the function generate output, it is obviously that at very low frequency the vibration generator will lose its power.

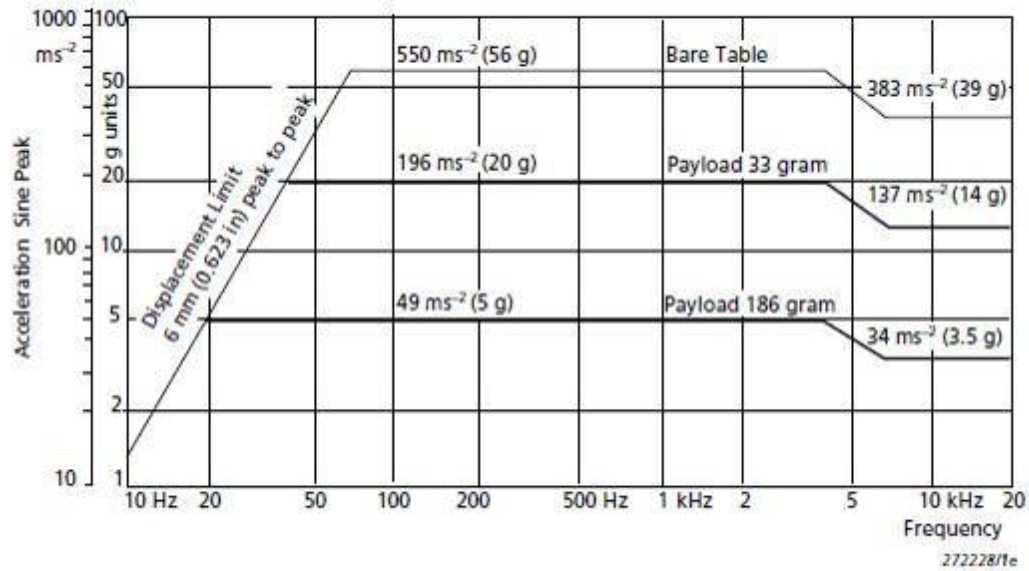


Figure 4.11 Frequency response for B&K 4810 Small Vibration Exciter.

Furthermore, since the vibration generator is the load of the amplifier, the coupling between those two devices also affects the final response of the system. A solenoid type stress generator tends to draw a large current at low frequency and causes the power amplifier exceed its linear range. We have experimentally found that when the frequency is below 0.5 Hz, the waveform output of the amplifier is obviously distorted away from the sine wave, and the amplifier will quickly run into overheat status. After numerous tests, it is determined that our system can stably provide the vertical strain level on rock sample at 10^{-7} to 10^{-6} down to frequency of 1Hz. This is monitored by real time strain gauge output and force sensor output.

The high frequency limit is controlled by the first resonance frequency appearing in the vibration system. In general, the resonance modes in a 3D structure are complicated, especially when the geometry of the structure is irregular, and/or the

material property in the structure is inhomogeneous. This is the case for our system, because it consists of not only the center column of sample-standard assembly, but also the top and bottom platens, as well as the supporting rods to connect the platens (Figure 4.12). Ideally, those platens and rods should be completely rigid body to provide fix boundary conditions to center vibration column. In reality, they are made of stainless steel with finite stiffness. They will participate in the vibration, and affect the overall resonance behavior of the whole system. Furthermore, even the center column is not a simple structure itself, since it consists of several cylindrical pieces of different material.

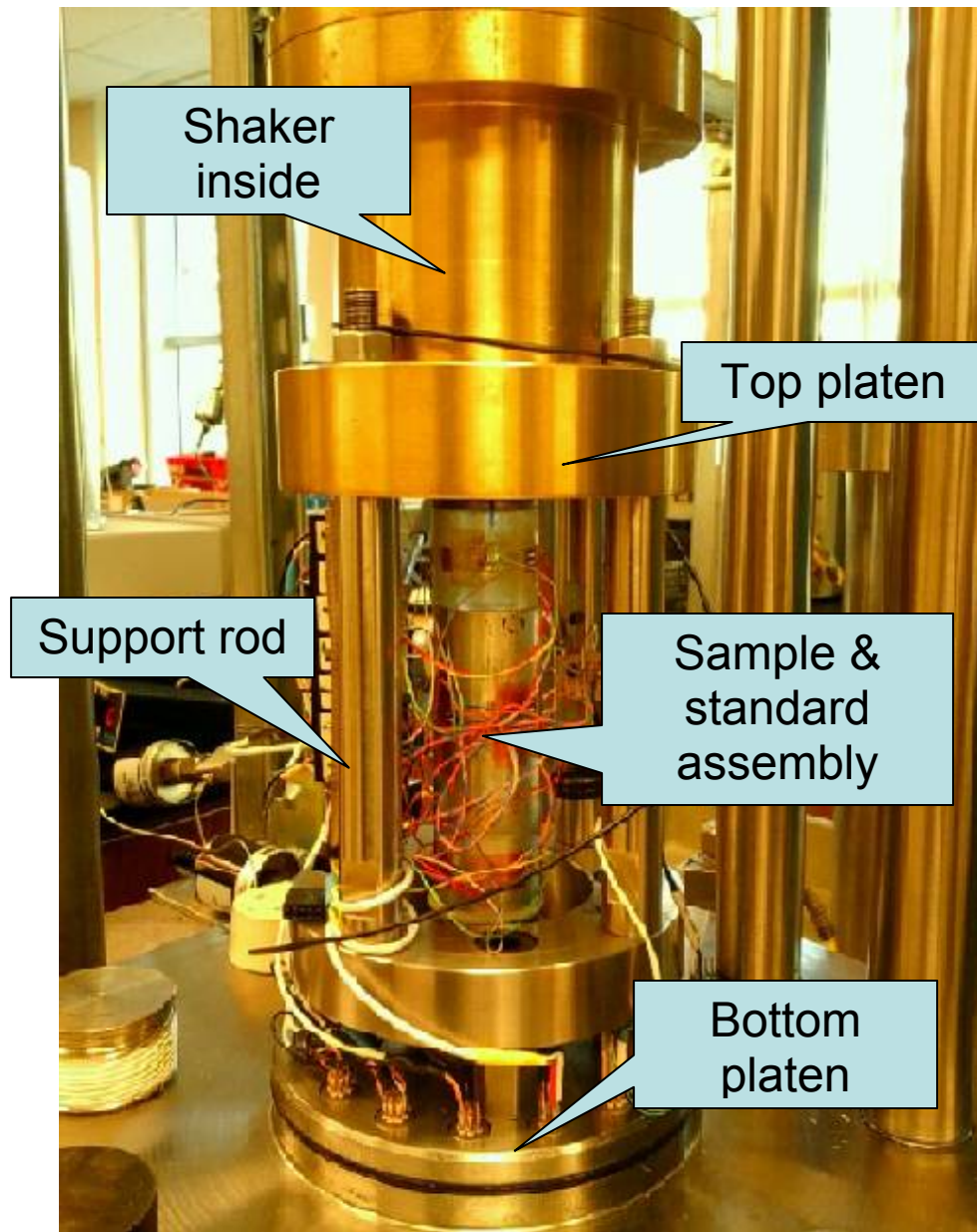


Figure 4.12 Picture of the vibration system.

Although there is such complexity in the resonance modes in our system, it is still helpful to use the resonance frequency in a 1D bar to understand the dominant factors controlling the first resonance frequency. The resonance frequency in a bar can be expressed as

$$f = n \frac{V}{2L} \quad n = 1, 3, 5, \dots \quad (4.19)$$

Here V is the average velocity in the whole bar, and L is the length of the bar. The first resonance frequency correspond to $n=1$; thus it is just $V/2L$. From this expression, one can see that with the same column length, measuring a stiffer sample with high velocity can have a higher frequency range before the first resonance gets in. Of course, the stiffness of the sample is not an option for us to choose. In order to expand the measurement frequency range to a higher frequency limit, one need reduce the total length of sample-standard assembly column.

Under the current design, material selection, fabrication, and assembled with typical sedimentary rock samples, the first resonance frequency in our system occurs around 1 kHz. But the vibration amplitude starts to ramp up around 600 Hz. So conservatively speaking, the frequency range of the current system is from 1 Hz to 500 Hz.

4.5.2 Scale of heterogeneity

While the ultimate goal is to simulate and measure the full scale heterogeneity as seismic wave see, the size of the sample imposes the limit to that. There is no way to duplicate the fluid relaxation with characteristic geometric length larger than several centimeters. Although some investigators (*e.g.*, Boitnott *et al.*, 2011) have suggested using high viscosity fluid to compensate the short relaxation length, one should recognize

that it may also introduce additional relaxation process purely within the fluid, like in the case of heavy oil sand.

Furthermore, the strain gauge has the size around 3-5 millimeters thus they actually are measuring the property of the small area directly beneath them, rather than the whole core plug sample. In order to use this spot property to represent the bulk property, we have to assume a basic homogeneity throughout the whole sample. However, our goal is to evaluate the effective media properties covering the heterogeneity in this volume. The requirement of homogeneity fundamentally impairs that main goal. So strictly speaking, the strain gauge method can only measure the dispersion and attenuation associated with the heterogeneity for less than one centimeter.

Furthermore, if there are larger (than the above mentioned) scale heterogeneities surrounding the area beneath the strain gage, it can affect the measurement results in complicated ways. Based on the discussions on partially open boundary in chapter 2 and 3, one can speculate that when the frequency deviates from high end, the measurement area can either be stiffen or soften, depends on the direction of fluid flow at the boundary of the REV. If the surrounding area is stiffer than the REV, fluid will flow out from the REV and cause the modulus and velocity drop with decreasing frequency. This will exhibit a normal dispersion curve in measurement result. However it neither represents the effective media properties of the whole core sample, nor the REV just below the strain gage. Next one can consider the case that there are one or more softer pockets surrounding the REV. In this case, the fluid will flow from the soft pockets into the REV,

and actually cause the increasing modulus and velocity when frequency decreases. This will exhibit a reversed dispersion curve in the measurement result. We shouldn't be surprised to see this kind of abnormal velocity-frequency relationship in a real measurement. It all depends on whether the strain gage sits on the relatively stiffer or softer spot compared to its surrounding area.

It is important to point out that this effect will be superimposed to the dispersion caused by the small scale heterogeneity within the REV. The magnitude of two mechanisms can be in the same order. This will make the interpretation of the real physical measurement result more difficult. Certain things can be attempted to mitigate the unwanted large scale heterogeneity effect. First, we should select the proper sample to avoid the large contrast heterogeneities in scales larger than strain gage size. Second, if it is impossible, we should try to carefully select the strain gage location to sit on relatively homogeneous area. Third, try to obtain the heterogeneity information can help to interpret the result. All those attempts may rely on the high resolution imaging technologies like micro-CT.

4.5.3 **Drain effect from pore fluid line**

Although leakage between the confining and pore fluid system has been always an issue in laboratory core measurement, and many techniques have been developed to attack it, in low frequency measurements, there are new requirements imposing many more new challenges to this old issue.

First, since our study is focused on fluid flow induced dispersion and attenuation, to include the pore fluid is essential and a dry measurement simply doesn't provide much valuable information.

Second, the rock sample has many open pores at its surface. At high frequency measurement, a rubber sleeve can perfectly seal the pore fluid system from the confining system. However, at low frequency, such a soft sealing will still allow the pore pressure relaxed to certain extend. As discussed in Chapter 2 & 3, this relaxation will cause dispersion and attenuation not belongs to the original rock. Therefore, some stiffer materials have to be applied to block all the open pores at the rock surface. In the meanwhile, the added material must not significantly alter the effective elastic properties of the original rock.

Third, to accurately measure the strain of the rock sample, the strain gages need to be attached to the surface of the sample as close as possible. Ideally, it is best to install the strain gages directly on the rock surface. However, the wiring of the strain gages must be well isolated from the pore fluid, to prevent the electric leak.

While most of the sample surface can be closed by stiff sealing materials like epoxy, the fluid flow line will leave two openings at top and bottom of the sample. Those openings are necessary to control the fluid saturation and pore pressure inside the rock samples. It is very difficult to completely close those openings right at the surface of the sample. Theoretically, those openings serve as leak drainages and will cause artificial

attenuation and dispersion due to the pore pressure relaxation through the openings. To evaluate the real impact of fluid line openings, we use numerical simulation tools to study the pore pressure evolution throughout the whole sample.

In real seismic situations, the external stress is applied as a time variant function, approximately in sine or cosine manner. In numerical simulation, we take a different approach. Assuming the external stress is applied suddenly as a step function, the pore pressure is built up according to the dry rock bulk modulus, fluid compressibility, and external stress (Skempton, 1954) immediately also as a step function. This corresponds to the high frequency case response. Using this as the initial status, and letting the pore pressure start to evolve, we can evaluate the relaxation process in a real geometry. COMSOL multiphysics software was used to simulate such time variant process in porous media.

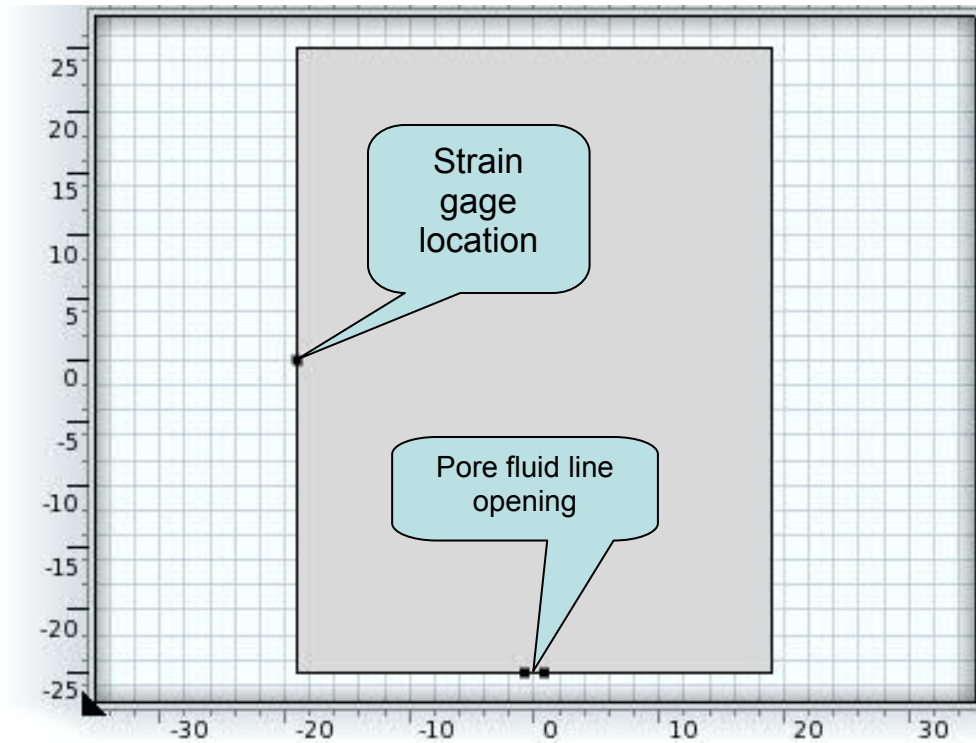


Figure 4.13 Numerical experiment setup to simulate the effect of fluid drainage at pore fluid line opening, on strain measured at the middle of the sample surface.

The model is built with real geometry values as in our physical experiment (Figure 4.13). The rock sample has a height of 50 mm and diameter of 38 mm. The strain gage is located at the midway of its height on the cylindrical surface, and single fluid line opening is located at the center of bottom surface. A set of typical rock and fluid properties are assigned to the model as shown in Table 4.1:

Table 4.1 Rock and fluid properties used in numerical simulation of leak drain effect from fluid line opening.

Description	Value	Unit
Young's modulus	1.50E+10	Pa
Poisson's ratio	0.15	
Fluid Density	1000	Kg/m ³
Dynamic viscosity	0.001	Pa*s
Porosity	0.2	
Compressibility	4.00E-10	1/Pa
Drained density of porous material	2300	Kg/m ³
Biot-Willis coefficient	1	

A vertical stress is applied on the top of the sample. The magnitude of the stress is not significant in this study, but is selected as 70,000 kPa to match the in-situ seismic stress. Figure 4.14 shows the instantaneous pore pressure distribution. One can then see that the pore pressure is higher near the bottom of the sample, especially at the corner (edge). This is due to the welded boundary condition at the bottom, which cause a stress concentration in those areas.

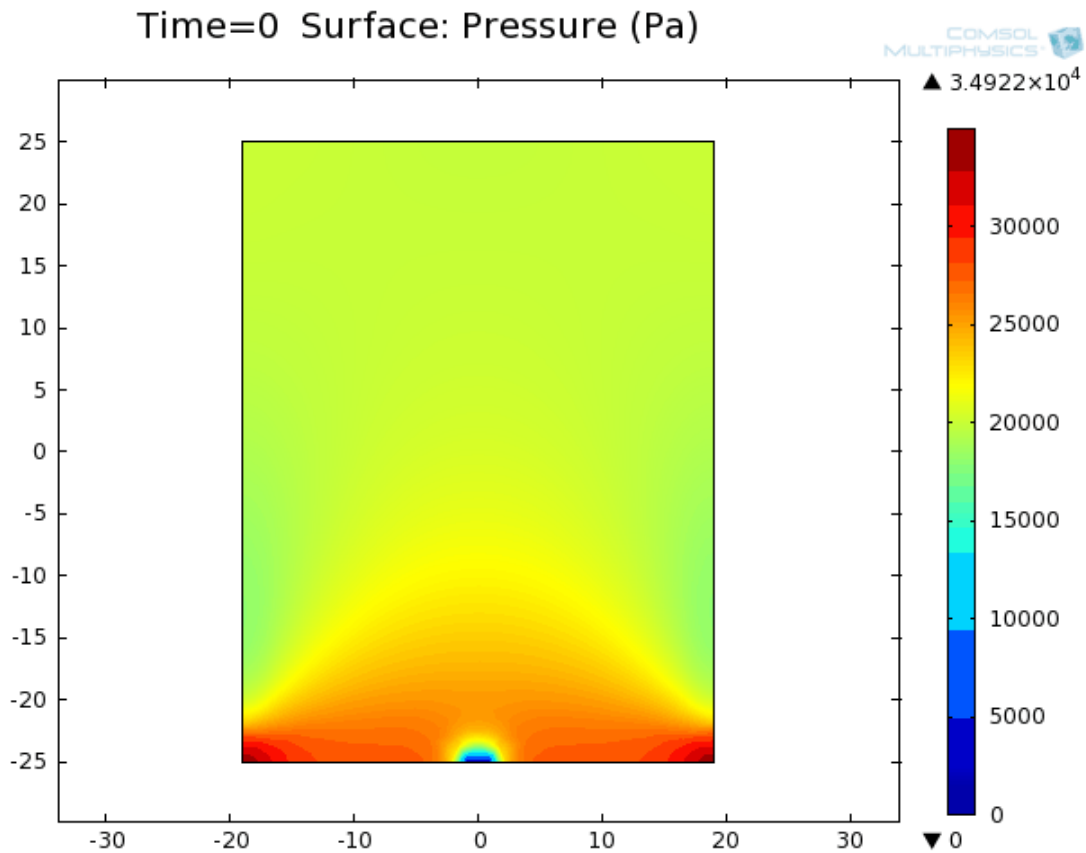


Figure 4.14 Instantaneous pore pressure distribution after the external stress applied on top of the sample.

In the first experiment, we set the fluid boundary condition at the opening as “completely open”. This means it cannot hold any pressure. Physically, it may represent the case that the sample is well connected to a large fluid reservoir with very high compressibility. For example, when a digital pump has air bubbles left in its cylinder, the overall compressibility of the pump fluid system is dominated by the air. Under this condition, any pore pressure reaching the opening will immediately reduce to zero, so the opening will behave as a significant drain spot. In Figure 4.15, we display the pore pressure evolution curve at the strain gage location with various permeability and

opening sizes. Basically the opening size does not have much influence to the evolution of the pore pressure. However, the permeability is an important factor to control this process. With 1000 mDarcy permeability, the pore pressure relaxes to close zero in less than 0.002 second. This implies that if the stress is added slowly, with a frequency around 500 Hz, at the strain gage location there is almost no pore pressure can be built up. Similar analysis tells in lower permeability rock samples, it takes longer time for the pressure under strain gage location to be relaxed. Figure 4.16 expands the time scale into 1 second, and shows that for a 1 mDarcy sample, the pore pressure will reduce to approximate $\frac{1}{4}$ of its initial value in 1 second.

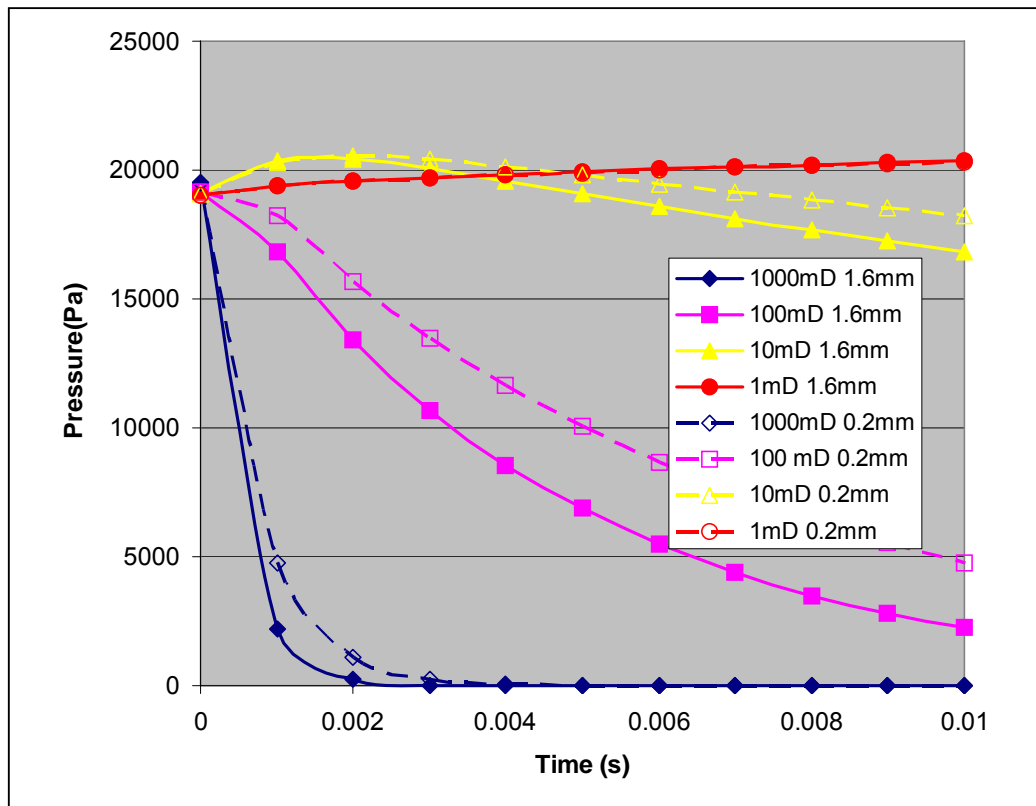


Figure 4.15 Pore pressure evolution curve at strain gage location, in 0.01 second time span, with various permeability and opening sizes.

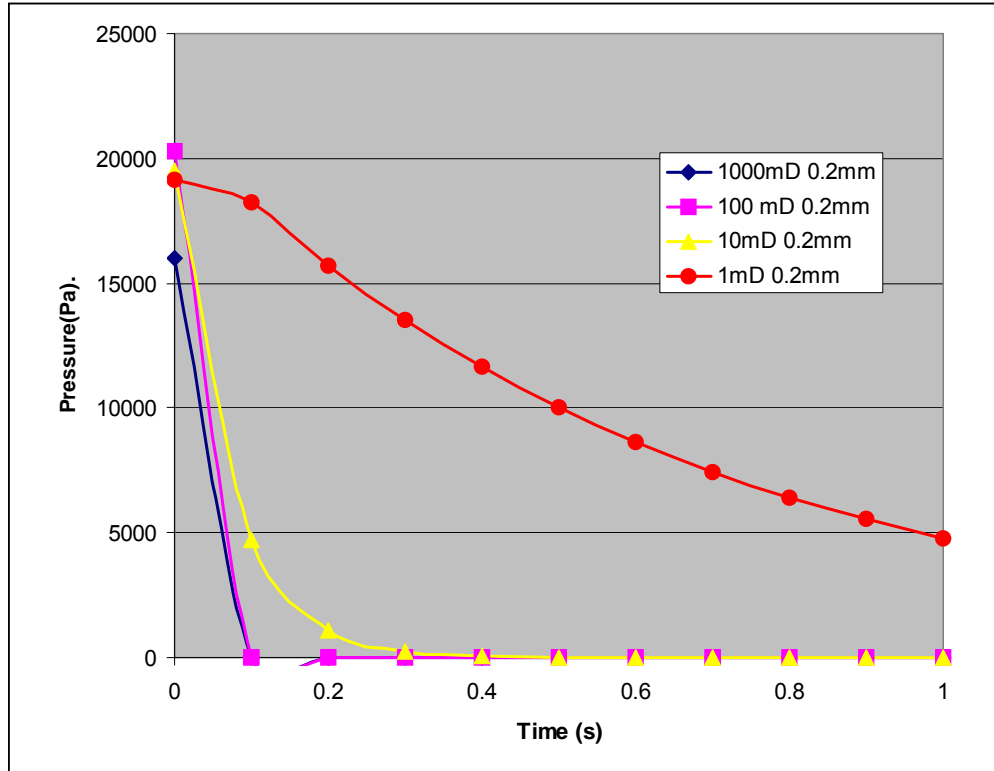


Figure 4.16 Pore pressure evolution curve at strain gage location, in 1 second time span, with various permeabilities.

A 1D diffusion equation can help us to roughly estimate the relaxation time and characteristic frequency. In 1D case, the pressure distribution $P(x,t)$ responding to an initial pressure P_0 can be expressed as:

$$P(x,t) = \frac{P_0}{\sqrt{4\pi Dt}} e^{-x^2/4Dt} \quad (4.20)$$

where D is the diffusivity

$$D = \frac{\kappa K_f}{\eta} \quad (4.21)$$

with κ as rock permeability, K_f as fluid modulus, and η as fluid viscosity.

The relaxation time τ is determined by

$$\tau = \frac{x^2}{4D} \quad (4.22)$$

Using the properties in Table 4.1, and geometry in Figure 4.13, one can estimate that with permeability of 1 mDarcy, the relaxation time is about 0.1 second. So for any frequency below 100 Hz, the pressure will be relaxed by the fluid line opening. This is generally in agreement with the 3D simulation results.

The above numerical experiment suggests that if the pore fluid line is connected to a large fluid tank containing gas bubbles, the measurement results can easily be contaminated by the fake dispersion and attenuation coming from drain effect on those lines, if the permeability of the sample is not low enough (must be below 0.01 mDarcy, for full measurement frequency range, 2- 2000 Hz).

To mitigate this effect, one needs to install a valve as close to the sample as possible. Once the saturation and pore pressure reach the desired condition, closing the valve can effectively reduce the drain effect since it cutoff the connection to the soft reservoir. The remaining “dead volume of liquid” is typically contained in stainless tubing, fitting and valve. All of those containers have very rigid body and not easy to deform. We again use the numerical simulation tool to study the effectiveness of such a method. In this modified numerical experiment, we keep everything the same as in first experiment, but change the fluid boundary condition at the opening. It is now connecting

to a small rigid container, which is filled with the same fluid as inside the sample (Figure 4.17). Due to this constraint, the fluid in the sample can not flow to “nowhere” through the opening, but has to equilibrate with the fluid in the small container. The resultant pore pressure evolution curves in Figure 4.18 exhibit no pressure drops at the strain gage location. This suggests that a closed valve can effectively prevent the drainage effect caused by the fluid line connecting to a soft reservoir.

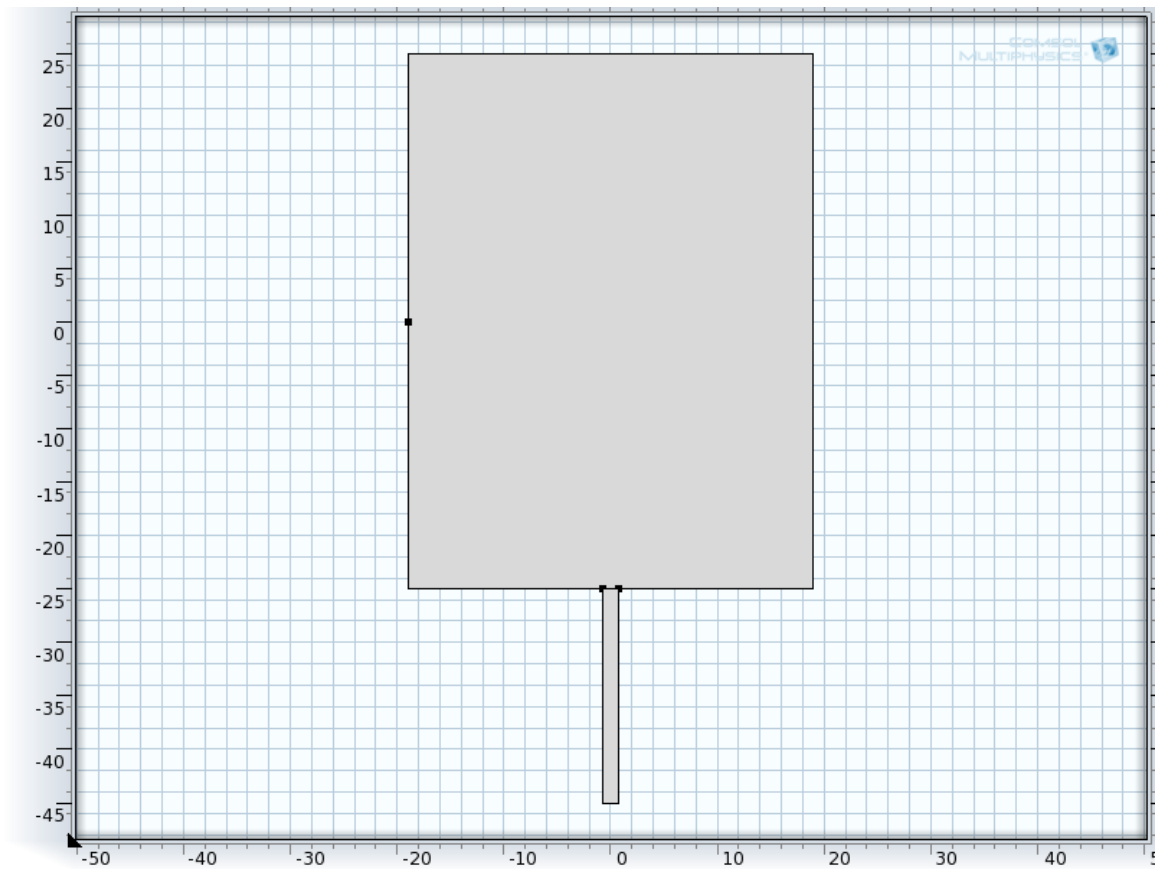


Figure 4.17 Modified fluid boundary condition at pore fluid line opening: connection to a small dead volume of fluid instead of a complete open boundary.

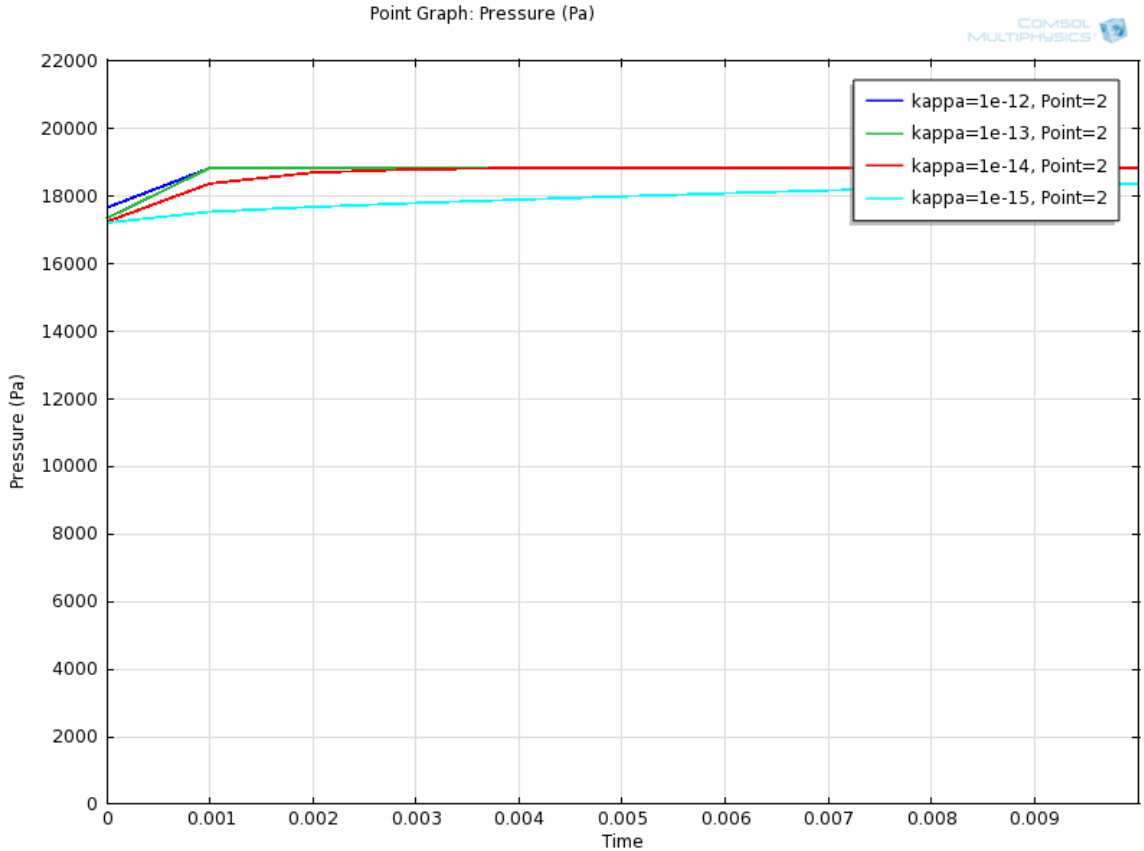


Figure 4.18 With modified boundary condition in Figure 4.17, there is no drainage effect at the strain gage location.

4.6 References

Adam, L., M. L. Batzle, and K. T. Lewallen, 2009, Seismic wave attenuation in carbonates: *Journal of Geophysical Research*, **114**, B06208.

Batzle, M. L., D.H. Han, and R. Hofmann, 2006, Fluid mobility and frequency-dependent seismic velocity—Direct measurements: *Geophysics*, **71**, no. 1, N1–N9.

Boitnott, G., M. Broadhead, and T. Kehe, 2011, Laboratory measurements of modulus dispersion in sandstone at seismic frequencies: *SEG Technical Program Expanded Abstracts*, 2236-2240.

Czichos, H., T. Saito, and L. Smith, 2006, *Springer handbook of materials measurement methods*: Springer.

Das, A., 2010, The viscoelastic properties of heavy-oil saturated rocks, PhD dissertation: Colorado School of Mines.

Domenico, S. N., 1976, Effect of brine-gas mixture on velocity in an unconsolidated sand reservoir: *Geophysics*, **41**, 882–894.

Gist, G. A., 1994, Interpreting laboratory velocity measurements in partially gas-saturated rocks: *Geophysics*, **59**, 1100–1109.

Gregory, A. R., 1976, Fluid saturation effects on dynamic elastic properties of sedimentary rocks: *Geophysics*, **41**, 895–921.

Gautam, K., 2003, Fluid Effects on attenuation and dispersion of elastic waves, MSc thesis: Colorado School of Mines.

Liu, H.P., D.L. Anderson, and H. Kanamori, 1976. Velocity dispersion due to anelasticity: implications for seismology and mantle composition: *Geophysical Journal of the Royal Astronomical Society*, **47**, 41–58.

Liu, H., and L. Peselnick, 1983, Investigation of internal friction in fused quartz, steel, plexiglass, and Westerly Granite from 0.01 to 1.00 Hertz: *Journal of Geophysical Research*, **88**, 2367-2379.

McKavanagh, B., and F.D. Stacey, 1974, Mechanical hysteresis in rocks at low strain amplitudes and seismic frequencies, *Phys. Earth Planet. Inter.*, **8**, 246-250.

Murphy, W. F., 1982, Effects of partial water saturation on attenuation in Massillon sandstone and Vycor porous glass: *Journal of the Acoustical Society of America*, **71**, 1458–1468.

———, 1984, Acoustic measures of partial gas saturation in tight sandstones: *Journal of Geophysical Research*, **89**, no. B13, 11549–11559.

Murphy, W. F., J. N. Roberts, D. Yale, and K.W. Winkler, 1984, Centimeter scale heterogeneities and microstratification in sedimentary rocks: *Geophysical Research Letters*, **11**, 697–700.

Paffenholz, J. and H. Burkhardt, 1989, Absorption and modulus measurements in the seismic frequency and strain range on partially saturated sedimentary rocks, *Journal of Geophysical Research*, **94**, 9493-9507.

Peselnick, L., H.-P. Liu, and K.R. Harper, 1979, Mechanical hysteresis loops of an anelastic solid and the determination of rock attenuation properties, *Geophysical Research Letters*, **6**, 545-548.

- Skempton, A. W., 1954, The pore-pressure coefficients A and B: *Geotechnique*, **4**, 143–147.
- Spencer, J.W., 1981, Stress relaxations at low frequencies in fluid-saturated rocks: Attenuation and modulus dispersion: *Journal of Geophysical Research*, **86**, 1803–1812.
- Tang, X.M., M.N. Toksöz, P. Tarif, and R.H. Wilhens, 1987, A method for measuring acoustic wave attenuation in the laboratory, *Journal of Acoustic Society of America*, **83**, 453-462
- Toksöz, M.N., D.H. Johnston, and A. Timur, 1978, Attenuation of seismic waves in dry and saturated rocks: I. Laboratory measurement, *Geophysics*, **44**, 681-690.
- White, J. E., 1983, *Underground sound, application of seismic waves*: Elsevier Science Publishers B.V.
- Winkler, K., and A. Nur, 1982, Seismic attenuation—Effects of pore fluids and frictional sliding: *Geophysics*, **47**, 1–15.
- Yin, C. S., M. L. Batzle, and B. J. Smith, 1992, Effects of partial liquid gas saturation on extensional wave attenuation in Berea sandstone: *Geophysical Research Letters*, **19**, 1399–1402.
- Zener, C., 1948, *Elasticity and anelasticity of metals*: University of Chicago Press.

5 LAB MEASUREMENT: SYSTEM DESIGN, BUILD AND CALIBRATION

5.1 Introduction

In last chapter the principles to measure the velocity dispersion and wave attenuation in sedimentary rocks at seismic frequency range, as well as the limitations of this method were discussed. In this chapter, the details on how we design and develop a working measurement system based on those principles will be presented. The emphases will be put on the major challenges we have faced, and the critical selections and solutions we have made.

The force deformation method has been applied in material science and structural engineering to measure the elastic strength of a wide range of materials for a long history. But those are in a static force with a relatively large deformation (normally much larger than 10^{-6} strain level). The measurement using a dynamic force with small deformation imposes non-trivial new challenges. Early works by Spencer (1981), Liu and Peselnick (1983) presented some very attractive results and showed people a great potential of this method. However, they also disclosed some of the difficulties and challenges in this method. The main challenges come from the weak strain gage output signals and very high sensitivity of the measurement results on sample preparation quality and mechanical assembling quality. These issues still remain as challenges today, and prevent this method from becoming a popular and routine lab technique. Batzle's group in the Colorado School of Mines continuously put their effort to develop some practical procedures to overcome the above mentioned problems and generated several valuable results in last

decade (Gautam, 2003; Batzle *et al.*, 2006; Hofmann, 2006; Adamet *et al.*, 2009; Das, 2010). However, they are still experiencing problems like low signal to noise ratio, low repeatability. The measurement efficiency is also low, due to limited number of channels that can be measured simultaneously.

Due to the recent increasing interest and demand on the understanding of dispersion and attenuation, more research groups have joined the effort to develop the laboratory measurement systems using force-deformation method. Among them, the groups at ETH (Swiss Federal Institute of Technology Zurich, Madona *et al.*, 2011) and Curtin University of Technology/CSIRO (Mikhailsevitch *et al.*, 2011) have made notable progresses in certain aspects. The ETH system uses LVDT instead of strain gage to measure the vertical length change of whole sample. It avoids the limitations associated with strain gage technique (see chapter 4), and simplifies the sample preparation process. However, their system lacks the capability to measure horizontal deformation. In principle it is not possible to obtain Poisson ratio and calculate the bulk and shear modulus, as well as the compressional and shear-wave velocities. In addition, at this moment, there is no pressure control in their system. This significantly limits its value to study the pore fluid effect on dispersion and attenuation. Curtin/CSIRO system doesn't have the drawbacks as the ETH system. However, their preliminary results presented at 2011 SEG (Mikhailsevitch *et al.*, 2011) displayed a dispersion curve below the Gassmann saturation value, which suggests a boundary leakage or pore fluid line drainage effect in their setup.

Our goal is to learn the experiences and lessons from previous investigators and current researchers, to build a working system, which can

1. Simulates the in-situ conditions which are critical to evaluate the fluid's contribution to velocity dispersion and wave attenuation.
2. Works on a well established procedures and protocols to minimize the random errors.
3. Controls the measurement efficiency and cost to an acceptable level, with potential to become a routine laboratory technique.

These goals serve as the guidelines during our design and fabrication of the low frequency system. For each functional subsystem, a typical development flow includes the following steps:

1. Search on available resources, and list all possible options.
2. Conduct a comprehensive evaluation and comparison between each option, with focus on performance, difficulty of implementation, efficiency and cost.
3. Select the optimal choice with certain compromises.
4. Implementation with continuous modifications.

During the course of this work, we have developed several unique and proprietary subsystems, which serve very well to our guideline and greatly improved the overall functionality and performance of the whole measurement system.

5.2 Critical design considerations

5.2.1 Pressure vessel structure

Our main research interest is to study the pore fluid-related dispersion and attenuation mechanism. For this purpose, the system must have the capability to inject the pore fluid into rock sample, and control the pore pressure separately with the confining pressure. Basically there are two types of pressure vessel design. The first type of design is depicted in Figure 5.1. The main body of the pressure vessel is fixed and stationary. The measurement assembly, which consists of the sample, standard, vibration source, bridge board, as well as numerous electrical and fluid line connections, is installed onto the vessel cap, and then transferred to the vessel body, for final sealing. The major advantage of this design is that it is possible to possess multiple sets of cap and measurement assembly with just one vessel body. While both measurement and sample preparation are time consuming, it can reduce the downtime of the whole system. However, there is also a major disadvantage with this kind of design. Our dynamic and small amplitude measurement is very demanding on the mechanical assembling quality. During the transfer of finished measurement assembly and sealing of pressure vessel cap, it is possible to change the pre-balanced stress distribution in the sample-standard column. This may significantly affect the measurement results; and this kind of error is random, and not correctable through calibration.

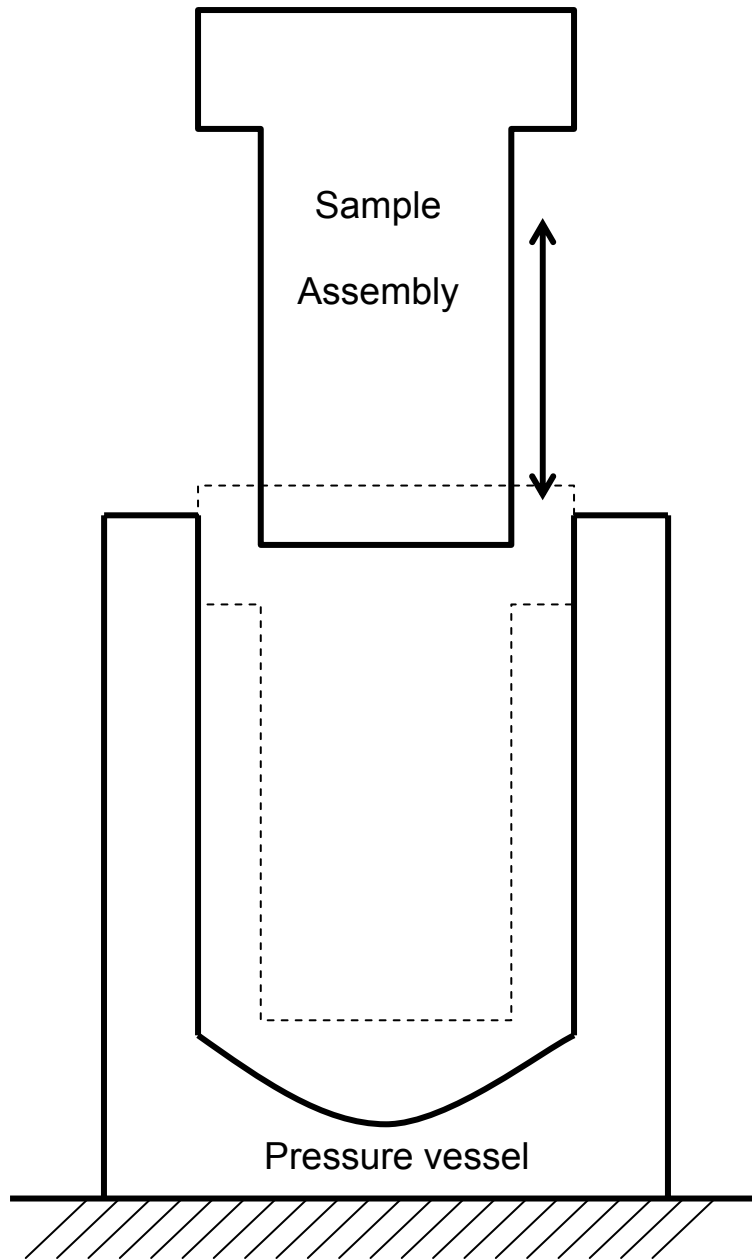


Figure 5.1 Schematic for fixed pressure vessel with moving sample assembly.

Due to the above consideration, we selected the second type of design (Figure 5.2). In this design, a bell-shaped main vessel body is movable by a hanging system. It is the only moving part of the whole system. The measurement assembly is installed directly onto the base platen. It remains stationary after assembled and fine tuned for

even stress distribution. With this configuration, the mechanical disturbance is literally removed. Additionally, by minimizing the frequent electrical and fluid line disconnection and reconnections, the reliability and durability of the system are significantly improved, and the uncertainty is reduced.

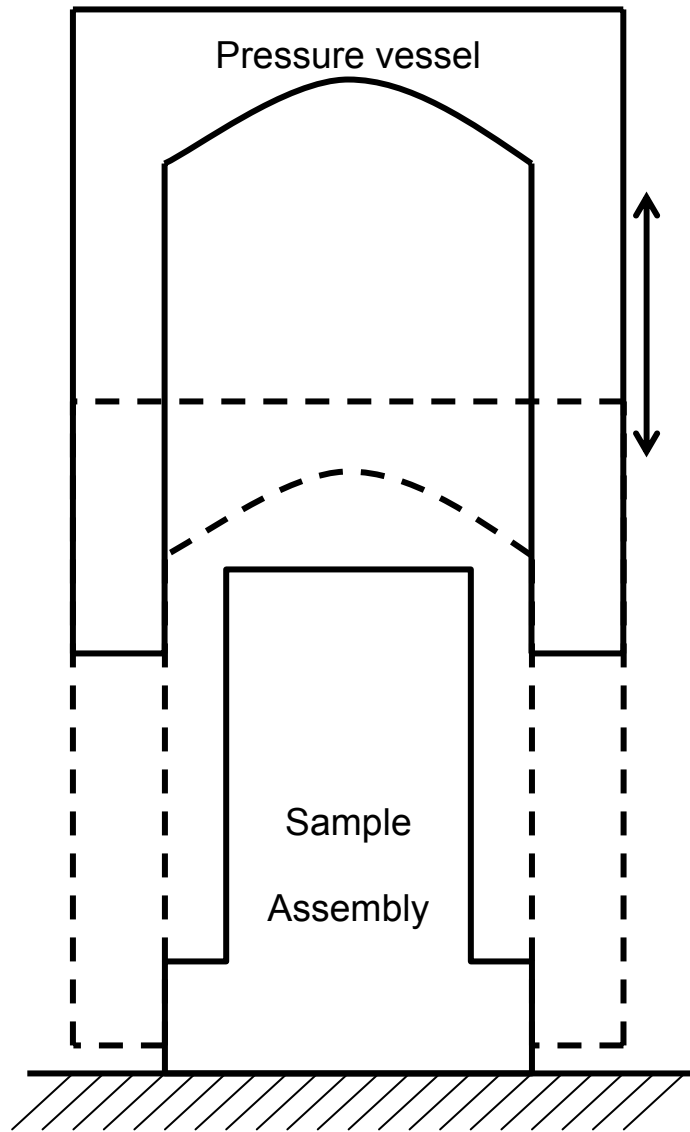


Figure 5.2 Schematic for fixed sample assembly with moving pressure vessel.

A potential benefit of this design is that it is possible to expand our measurement from uniaxial to triaxial stress configuration. With a center throughhole opened on top of

the vessel, we can apply an independently controlled vertical stress to the sample, by a hydraulic pump and a rod from outside of the pressure vessel.

5.2.2 **Vibration source**

The dynamic deformation of the sample is accomplished by an electrical driven vibration source. There are two types of vibrators available in the market. They have distinct features electrically and mechanically. We have done extensive tests on both types of devices. Although highly attracted by the advantages of the PZT actuator, the extremely demanding installation quality has forced us to select a speaker like vibrator in current setup, but continue to pursue a solution with PZT to fully utilize its superior benefits.

The speaker-like vibrator uses a coil and magnet pair to convert the electrical signal into mechanical motion. Electrically it is a series resistor-inductor circuit with its impedance and current as:

$$\begin{aligned} Z &= \sqrt{R^2 + (\omega L)^2} \\ I &= V / Z \end{aligned} \tag{5.1}$$

where Z is the total impedance, R is the resistance, L is the inductance, V and I are voltage and current respectively, and ω is the angular frequency. As a current driven device, one can see that the current it draws from the power supply will increase quickly when the frequency goes to low end. This imposes a limitation to the low frequency limit of our measurement, as the power supply has a maximum allowed current, and an overheat protection threshold. Practically, it has been determined that it is not a good

practice to operate the vibrator at frequency lower than 1Hz since it always push the power supply into a overheat status.

Another big drawback of the speaker-like vibrator is its small force output. Physically limited by the Lorentz force, the maximum force our vibrator can generator is 10 Newton. However, if one wants to achieve a 10^{-6} strain on a rock sample with 20 GPa Young's modulus, one needs to apply 20 kPa stress to it. With the diameter of 38 mm, it requires the total force of 22.7 N.

This means we will not be able to reach the expected strain amplitude and will have to sacrifice the signal-to-noise ratio, which is essential to control the error in measurement results, especially for phase and attenuation calculation.

On the other hand, a PZT actuator works with completely different mechanism and provides superior remedy to the above mentioned problems in speaker-like vibrator.

A PZT actuator consists of a stack of piezoelectric ceramic disks and converts applied electrical voltage into a mechanical force. First of all, the piezoelectric force from a typical PZT stack can be hundreds to thousands times larger than what we can get from a small size coil-magnet pair vibrator. Therefore we can easily tune the strain amplitude into the 10^{-6} level, which is believed to be the maximum realistic seismic strain amplitude without grain boundary slipping and frictional loss.

PZT ceramic is a capacitor; and electrically it is a series resistor-capacitor circuit with its impedance and current as:

$$\begin{aligned} Z &= \sqrt{R^2 + 1/(\omega C)^2} \\ I &= V / Z \end{aligned} \quad (5.2)$$

As a voltage-driven device, it doesn't have the current overshoot problem as in the speaker-like vibrator. Therefore it is a better choice in low frequency measurement.

The above comparison leads us in favor of the PZT actuator as vibration source. However, further tests reveal that there are other issues related to the use of PZT actuator. As discussed in 5.3.1, to ensure the even stress distribution in the sample-standard column, all the contact interface between individual components have to be in a near perfect contact status. It is beyond the current machining serve capability available to us now. Applying a vertical pre-stress can mitigate the problem. Tests show that a 6-8 MPa stress is needed for this purpose. The concern is that this vertical stress will alter the properties of the sample to be measured. Furthermore, after a confining pressure is applied, the shrinking of the sample will release the pre-stress, and cause the bad contact status again. Even after numerous tests on various ideas, those complicated issues are still remained as not completely solved. Thus at this moment, we have to make a compromise to use the speaker-like vibrator as our vibration source. Because of its inherent large zero offset tolerance, it is possible for us to glue all components together. The natural curing process of the epoxy between the column and vibrator has a self-alignment effect to evenly distribute the stress azimuthally.

5.2.3 Virtual lock-in amplifier

In chapter 4, the principles of the lock-in amplifier were introduced. In our application, due to small mechanical strain amplitudes, the Wheatstone bridge voltage outputs are normally in micro-volt range. But the various noise sources like power line fluctuation, ground loop common mode noise, and environment EMF can easily have amplitudes larger than that. So it is much desired to use lock-in amplifier to retrieve the signals. Fortunately, the frequency of the signal is well known in the forced vibration experiments. This makes the lock-in amplifier easily applicable and almost a standard configuration in such experiments.

The early lock-in amplifiers were implemented with analog electronic circuits with very high complexity and low stability. Currently, almost all the lock-in amplifiers in the market are implemented with digital signal processor along with an AD convertor that converts the input analog signals into digital ones.

Based on a deep study on the principles and performance of the lock-in amplifier, we believe the major task of the lock-in amplifier can be accomplished completely with software. Through a market survey we found National Instrument has developed a simple virtual lock-in algorithm. Based on this algorithm, we developed the first working virtual lock-in amplifier system in the world. Compared with the stand-alone hardware lock-in amplifier, there are several notable advantages:

1. By separating the lock-in process from the data acquisition, we have the ability to select the best acquisition instruments for our application. In a

typical measurement, we need to install at least 6 channels of strain gage (2 sets of Young's gage and 2 sets of Poisson gage on rock samples, another 2 sets of Young's gage on aluminum standard). The very small signals require the acquisition board has a high vertical resolution. The NI4498 acquisition system we selected has 16 input channels with 24 bit vertical resolution. With a +/-10 V input range, this 24 bit means a resolution to 37nV, which is superior and capable enough to handle our signals.

2. Developed in National Instrument Labview platform, this lock-in amplifier has the highest integrity with the NI acquisition hardware. It is also highly integrated with the post acquisition operations, like data recording, derived value computing, and real time display and monitoring.
3. It provides users with high flexibility to configure the system according to different measurement setups. For example, one can easily change the channel assignment in each measurement. One can also easily add calibration coefficients to correct the system errors from various sources (see discussion in section 5.4).

Since the lock-in amplifier plays a critical role in the data acquisition and processing, we have carried out many tests to evaluate its performance. Next, two of those tests are presented to demonstrate the quality of our virtual lock-in amplifier.

5.2.3.1 Test on synthetic data

In this test, synthetic data were used to test the lock-in amplifier's ability to retrieve signal with various level of noises. Each data set consists of 6 waveforms. The first one is a zero phase noise free sinusoid wave. Total length is 600 periods, and amplitude is 1. The other 5 are generated from the first one by adding 1%, 10%, 50%, 100%, and 1000% white noise to it. In Figure 5.3, the first 3 periods of the waveforms are displayed.

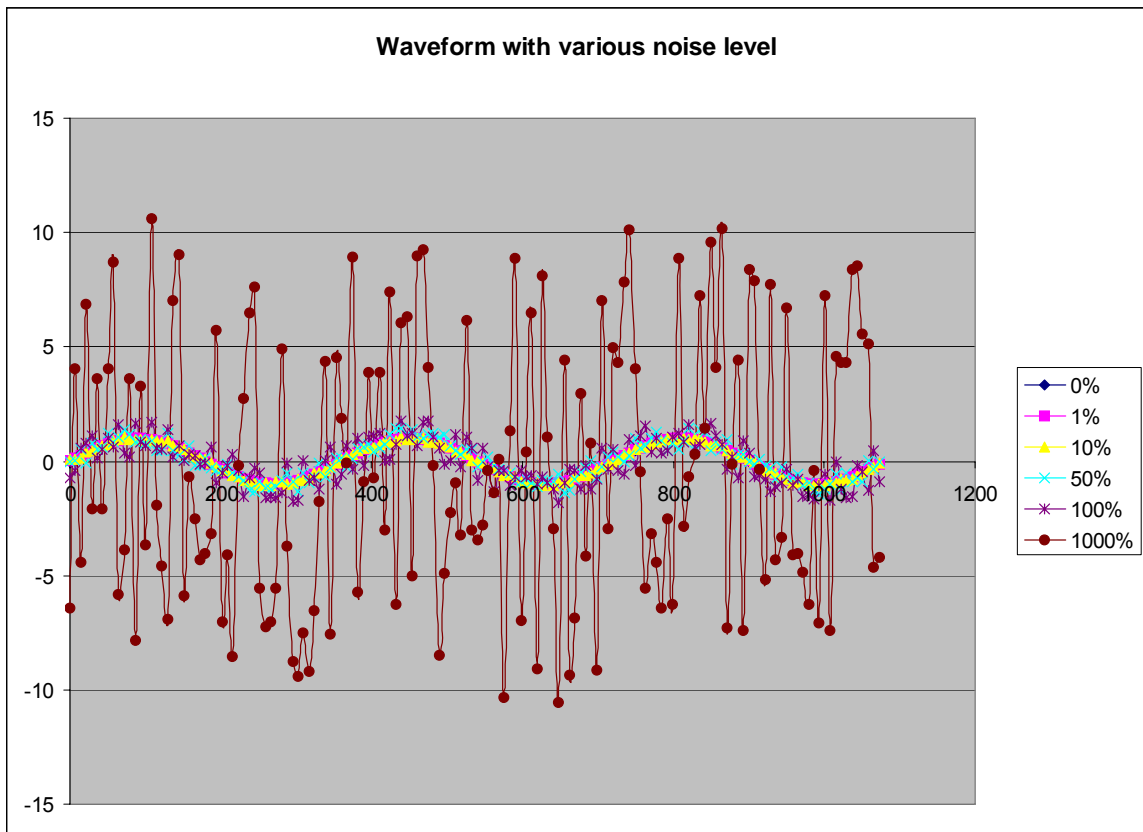


Figure 5.3 First three periods of synthetic waveforms, with different level of white noises, to test the performance of the lock-in amplifier.

To statistically study the performance, the data sets are randomly generated for ten realizations. Each realization is input into the lock-in amplifier to retrieve the amplitudes and phases for all waveforms. The results are listed in Table 5.1

Table 5.1 Amplitudes and phases retrieved from synthetic noisy data by virtual lock-in amplifier.

Realization #	Retrieved Amplitude by Lock-in Amplifier						Retrieved Phase by Lock-in Amplifier (degree)					
	Noise/Signal						Noise/Signal					
	0.00	0.01	0.10	0.50	1.00	10.00	0.00	0.01	0.10	0.50	1.00	10.00
1	1.000	1.000	1.001	0.998	1.005	0.902	0.000	0.001	0.014	0.077	0.296	1.811
2	1.000	1.000	1.000	1.003	0.989	0.981	0.000	0.001	0.053	0.050	0.234	2.780
3	1.000	1.000	1.000	0.998	0.998	1.001	0.000	0.003	0.031	0.450	0.063	2.833
4	1.000	1.000	1.000	1.003	0.995	0.928	0.000	0.002	0.013	0.101	0.388	1.305
5	1.000	1.000	1.000	0.999	0.991	1.000	0.000	0.002	0.040	0.262	0.711	2.729
6	1.000	1.000	1.000	0.999	1.005	1.121	0.000	0.002	0.008	0.025	0.094	2.282
7	1.000	1.000	1.000	0.999	0.992	0.994	0.000	0.001	0.031	0.102	0.473	5.306
8	1.000	1.000	1.000	0.998	0.993	1.016	0.000	0.001	0.021	0.006	0.463	4.549
9	1.000	1.000	1.000	1.003	0.990	0.999	0.000	0.001	0.032	0.228	0.029	2.305
10	1.000	1.000	0.999	1.000	0.999	0.984	0.000	0.001	0.025	0.215	0.560	1.697
Ave.	1.000	1.000	1.000	1.000	0.996	0.992	0.000	0.000	0.002	0.064	0.123	0.913
Stdv.	0.000	0.000	0.001	0.002	0.006	0.058	0.000	0.002	0.031	0.199	0.396	3.020

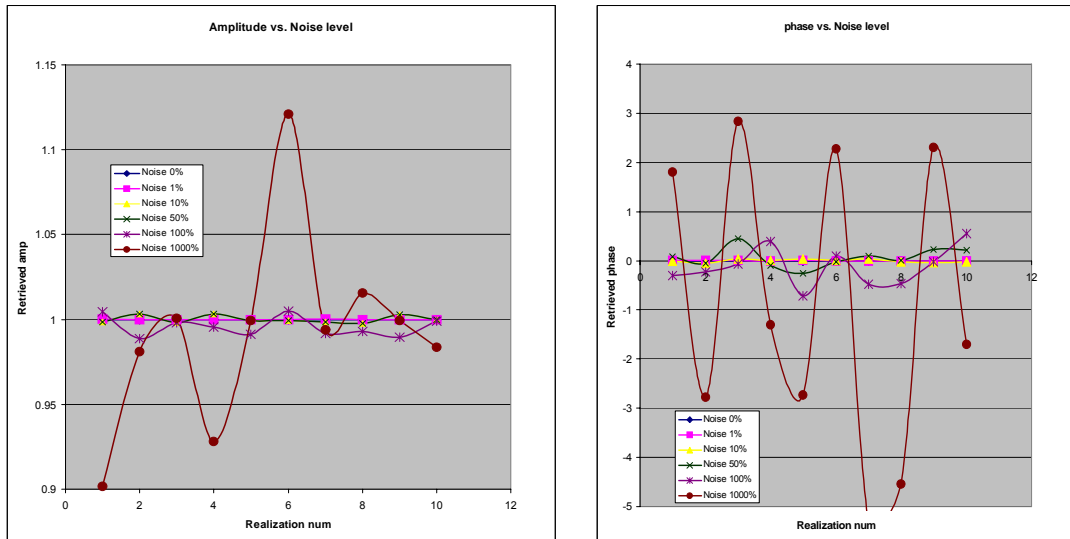


Figure 5.4 Using lock-in amplifier to retrieve amplitude (left) and phase (right) from 10 realizations of synthetic noisy data.

In Figure 5.4, the retrieved amplitudes (left) and phases (right) are plotted for all realizations. These plots suggest that when the data contain 100% noise, the retrieved amplitude may have less than 2% error, and the phase may have about 0.5 degree error, which approximately converts to 0.01 in $1/Q$ value. With 1000% noise, the errors in amplitude and phase can exceed 10% and 5 degree (0.1 in $1/Q$ value) respectively, thus not acceptable for Young's modulus and attenuation estimation. From the 10 realizations, we calculated the average and standard deviation under each noise level (Figure 5.5). It shows that error level increase slowly with the noise level before the noise reach 100%. Beyond that, the error goes up quickly making the experiment results unacceptable. This provides a guideline that we must control the hardware noise protection to ensure the signal to noise ratio above 1 when the data reach the acquisition board. In figure 5.6, we display three typical waveforms from sample Young's gage (left), sample Poisson gage (middle) and Al Young's gage (right), acquired at vibration frequency of 20 Hz. The data from sample Young's gage have the best signal-noise ratio, followed by the Al Young's gage. Sample Poisson gage has the lowest signal-noise ratio. This is mainly due to the difference of the strain amplitudes from those three types of gages, while the noises are similar on all of them. Nevertheless, from this figure one can see that both time domain waveforms and frequency domain spectra show the signal-to-noise ratio in our acquired experimental data is well above 1.

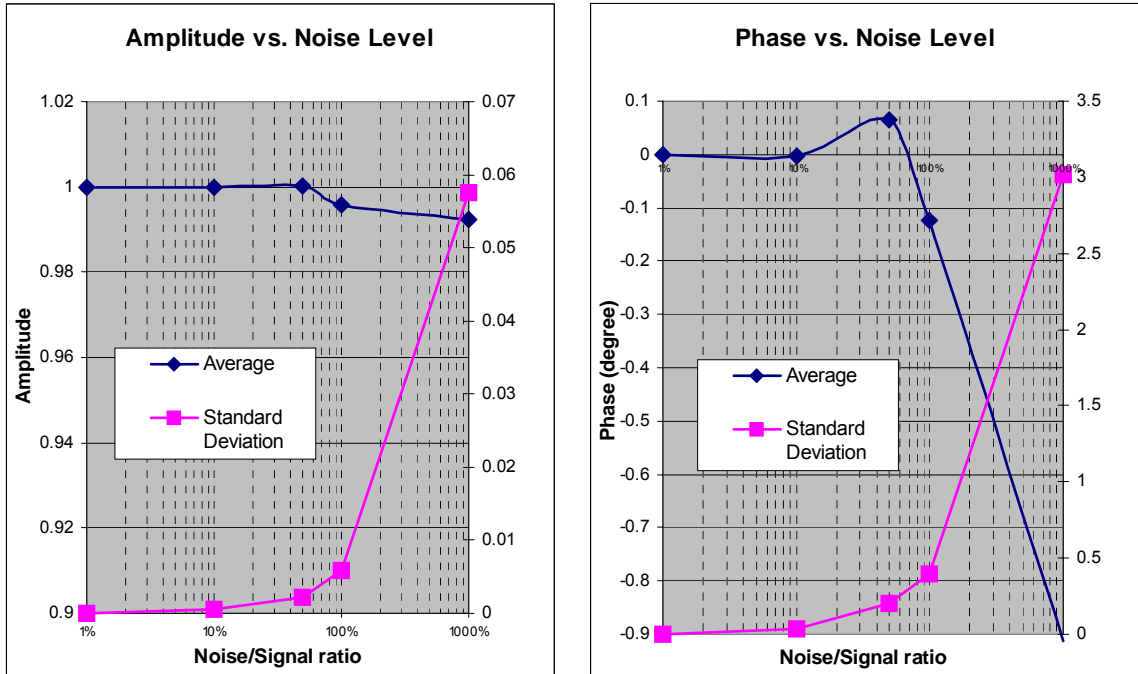


Figure 5.5 Error analysis based on experiments on 10 realizations of synthetic data.

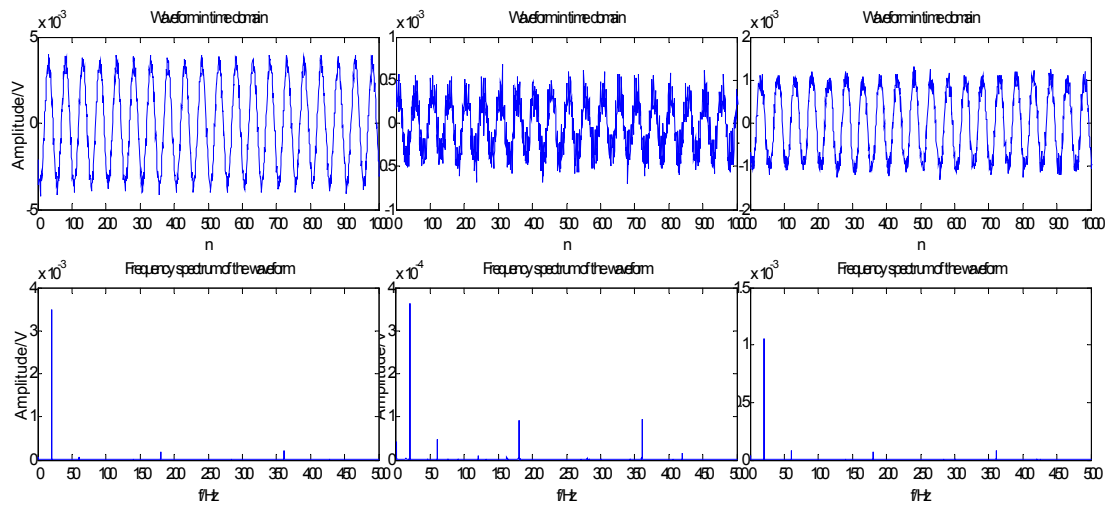


Figure 5.6 Typical waveforms from sample Young's gage (left), sample Poisson gage (middle) and AI Young's gage (right). Vibration frequency is 20 Hz. Both time domain waveforms and frequency domain spectra show the signal-noise ratio well above 1.

5.2.3.2 Test on real experimental data

The whole acquisition and processing program is developed based on the NI lock-in amplifier algorithm. The NI user manual (NI, 2006) provides description on its principle, functionalities, and controls, but does not offer the access to its original code. To better evaluate its performance on our particular application, we established another lock-in amplifier implementation, called DPSD (digital phase sensitive detector) in Matlab. We applied both NI implementation and Matlab implementation to the real experiment data, to cross check the relative error between them, as an indirect method to test the performance of both implementations.

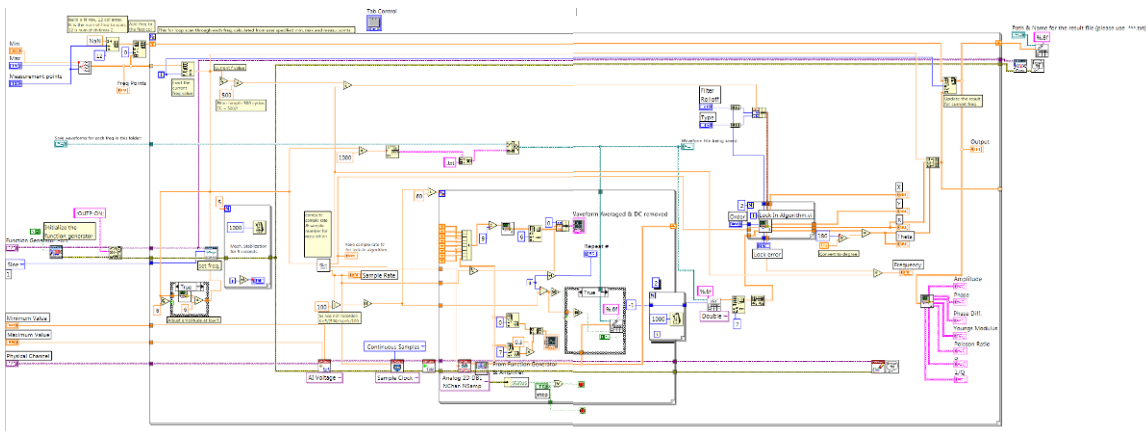


Figure 5.7 PC Labview program for automatic acquisition, processing, display, and recording.

As Labview is a graphical language, the whole finished program is documented in Figure 5.7; and the Matlab implementation is included as Appendix A. The data used for tests include 2 sets of real experimental waveforms, recorded at 20 Hz and 200 Hz respectively. Each set has a reference channel and 6 channels from strain gage Wheatstone bridges. Ch1/2 are from Young's gages on rock sample, Ch3/4 are from Poisson gages on rock sample, and Ch5/6 are from Young's gages on Al standard. Table

5.2 and 5.3 list and compare the results from two independent implementations of the lock-in amplifier. The maximum relative error between them is 0.72%, and the average relative error is around 0.1%. This cross check implies that the NI virtual lock-in amplifier has a reliable and stable performance on typical acquired data from our low frequency measurement experiments.

Table 5.2 Comparison between the retrieved amplitudes and phases by Labview lock-in amplifier and Matlab lock-in amplifier, on a real data set acquired at 20 Hz.

	Amplitude (V)		Relative error	Phase (degree)		Relative error
	Matlab	NI		Matlab	NI	
Ch1	0.003508	0.003501	0.20%	4.339656	4.354987	0.35%
Ch2	0.00352	0.003519	0.01%	4.43879	4.460367	0.49%
Ch3	0.000364	0.000364	0.05%	172.91	172.8154	0.06%
Ch4	0.000242	0.000242	0.03%	173.2978	173.3417	0.03%
Ch5	0.001057	0.001057	0.01%	5.250287	5.24029	0.19%
Ch6	0.001007	0.001008	0.06%	5.271787	5.275756	0.08%

Table 5.3 Comparison between the retrieved amplitudes and phases by Labview lock-in amplifier and Matlab lock-in amplifier, on a real data set acquired at 200 Hz.

	Amplitude (V)		Relative error	Phase (degree)		Relative error
	Matlab	NI		Matlab	NI	
Ch1	0.003287	0.003288	0.04%	-92.8466	-92.9708	0.13%
Ch2	0.003296	0.003299	0.08%	-93.0834	-93.1012	0.02%
Ch3	0.00036	0.000361	0.21%	88.31836	88.28254	0.04%
Ch4	0.000231	0.00023	0.72%	87.07849	86.93269	0.17%
Ch5	0.001013	0.001012	0.14%	-92.2003	-92.2035	0.00%
Ch6	0.000971	0.00097	0.09%	-92.1728	-92.1755	0.00%

One of the main noise sources is from the power line, which has 60 Hz working frequency along with several harmonics at 120 Hz, 180 Hz, etc. To test whether the lock-

in amplifier can effectively retrieve the signal in case the power line noise is not well isolated, we used the real waveforms acquired at 20 Hz, and manually add 60 Hz, 120 Hz, and 180 Hz noises with their amplitudes 1000 times of the signal amplitude. The mixed signal on ch1 in time domain and frequency domain are plotted in Figure 5.8. This mixed signal and the original signal are both processed by the lock-in amplifier. The results are listed in Table 5.4. The relative errors in both amplitude and phase are literally ignorable. This test demonstrates our lock-in amplifier can effectively remove the power line noises.

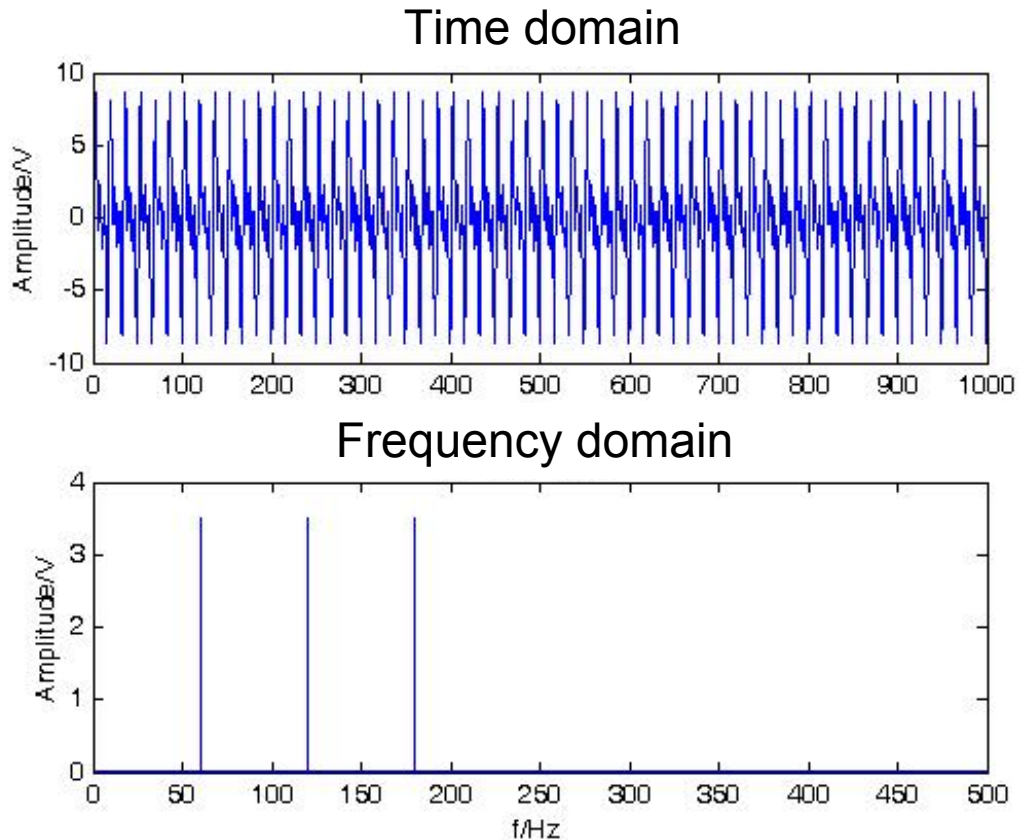


Figure 5.8 Real data from Ch1 at 20 Hz are mixed with power line noise at 60 Hz, as well as its harmonics at 120 Hz, 180 Hz. The noise amplitudes are 1000 times of the signal amplitude. Top is the waveform in time domain, and bottom is amplitude spectrum in frequency domain.

Table 5.4 Adding 1000 times noises from power line does not affect the lock-in amplifier's performance to retrieve amplitude and phase of low frequency measurement signal.

	Without noise	With noises	Relative error
Amplitude (V)	0.003501387	0.003501387	3.998E-12
Phase (degree)	4.347862222	4.347862222	7.620E-12

In the last test with synthetic data, we have shown that a white noise with 100% amplitude can start to deteriorate the lock-in amplifier performance, but in this test a 1000 time larger noise does not introduce any meaningful error. The contradiction between them can be explained by the lock-in amplifier principles.

$$\sin(\omega_{ref}t)\sin(\omega_{noise}t) = \frac{1}{2}[\cos(\omega_{ref} - \omega_{noise})t - \cos(\omega_{ref} + \omega_{noise})t] \quad (5.3)$$

When a noise component is mixed with the reference signal, it generates two terms in the same manner as the signal does. The second term always has the frequency summed by the reference and noise frequency; therefore results in a higher frequency and can be easily removed by a low pass filter. However, the first term has its frequency as the difference between reference and noise frequency. When the difference gets small, this term becomes close to a DC component, and difficult to be removed by a low pass filter. In our first test, the white noise contains all frequency components, including those very close to the signal and reference frequency. But in second test, the added noises have frequencies far away from the signal and reference frequency, so that even the noises have very high amplitudes, they can be effectively removed by the lock-in amplifier.

So it is important to evaluate the minimum frequency difference between noise and signal, where the lock-in amplifier starts to produce unacceptable error. This can be tested by moving the added noise closer and closer to the signal in frequency domain, and compared the processed results with what from original data (without added noise). The test on 20 Hz data shows that when the noise frequency is below 19.9 Hz or above 20.1 Hz, the lock-in amplifier always get almost identical results. Table 5.5 shows the results with noise at 18 Hz.

Table 5.5 The effect of 18 Hz noise on the 20 Hz data.

	Without noise	With 18 Hz noise	Relative error
Amplitude (V)	0.003501387	0.003501387	0%
Phase (degree)	4.347862222	4.347862222	1.98E-12

Tests on data acquired at other frequencies obtained similar results. It suggests that our lock-in amplifier can effectively remove the noises with frequencies beyond +/- 1% of the desired signal and reference frequency. As the power line frequency and its harmonics being recognized as the main noise source, one can design the experiment so that the measurement frequency points are carefully selected to avoid coincident with power line frequency and its harmonics.

5.3 Critical challenges in system building

We have faced numerous challenges during the development of the low frequency measurement system. Some are minor issues and can be solved with limited efforts, but some are major and take very long learning curve to overcome. Among them, the two

most significant challenges are the stress distribution problem in sample-standard assembly, and small signal protection, acquisition, and processing. These will be discussed in detail.

5.3.1 **Vibration mode and stress distribution**

In measurement principle discussed in chapter 4, there is one fundamental assumption: the stress is uniform distributed both vertically and azimuthally throughout the sample and standard assembly column. This is the basis for our relative measurements because both Young's modulus and Poisson ratio are calculated from the ratio of strains on various gages at different locations. In reality, this can only be approximately achieved, even with very careful sample preparation and assembling operations. If not properly handled, this condition can be wildly violated.

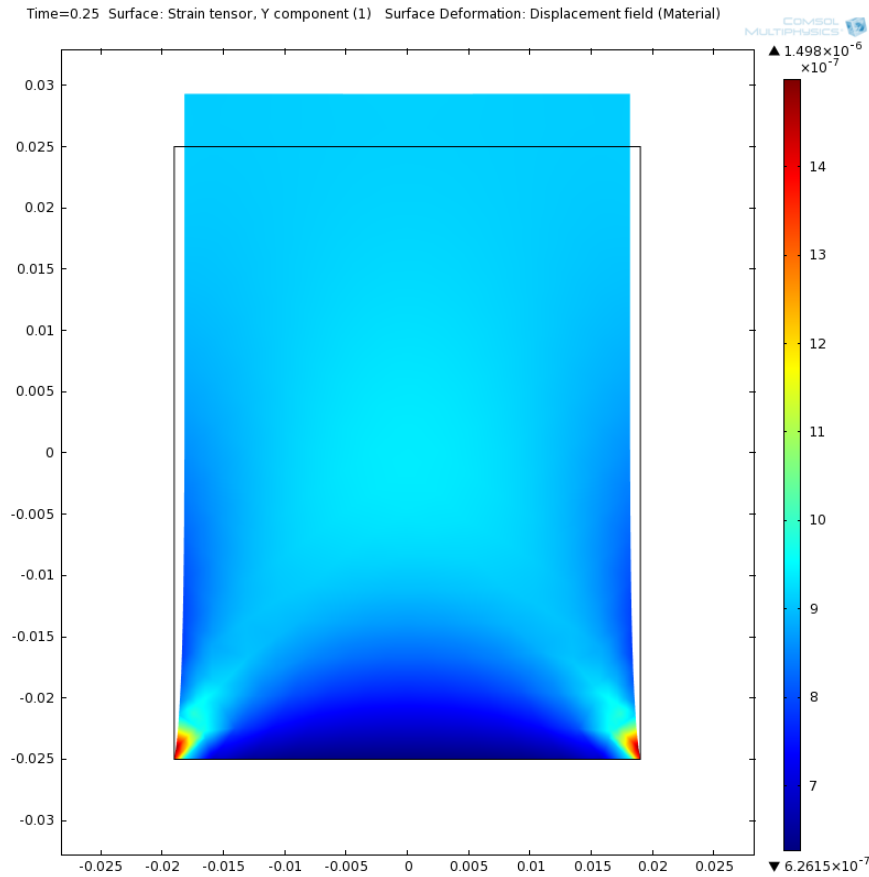


Figure 5.9 Numerical simulation shows an non uniform strain distribution throughout the cylindrical core plug sample, due to the boundary constraints.

Theoretically, uniform stress can only happen in homogeneous medium filling the whole space. In any real object, even the heterogeneity can be neglected, the constraints from boundaries will create the stress concentration at some areas and dilution at other areas (Moghe and Neff, 1971). This can be easily verified with finite element simulation. In Figure 5.9, we applied an upward stress of 70 kPa at the top of an aluminum cylinder with Young's modulus of 70 GPa. If the stress is evenly distributed, one should expect a vertical strain of 10^{-6} everywhere in the cylinder. However, due to the fixed boundary at the bottom and free boundary at the cylindrical surface, Figure 5.9 clearly shows a non-

uniform strain level throughout the body. In Figure 5.10, we plot the strain value on surface, along the vertical axis. The “Arc length” from 0 to 0.05 corresponds to from bottom to top. If the strain gage is located right at the middle of its height, the strain is only about 87% of the expectation value from a uniform stress distribution model.

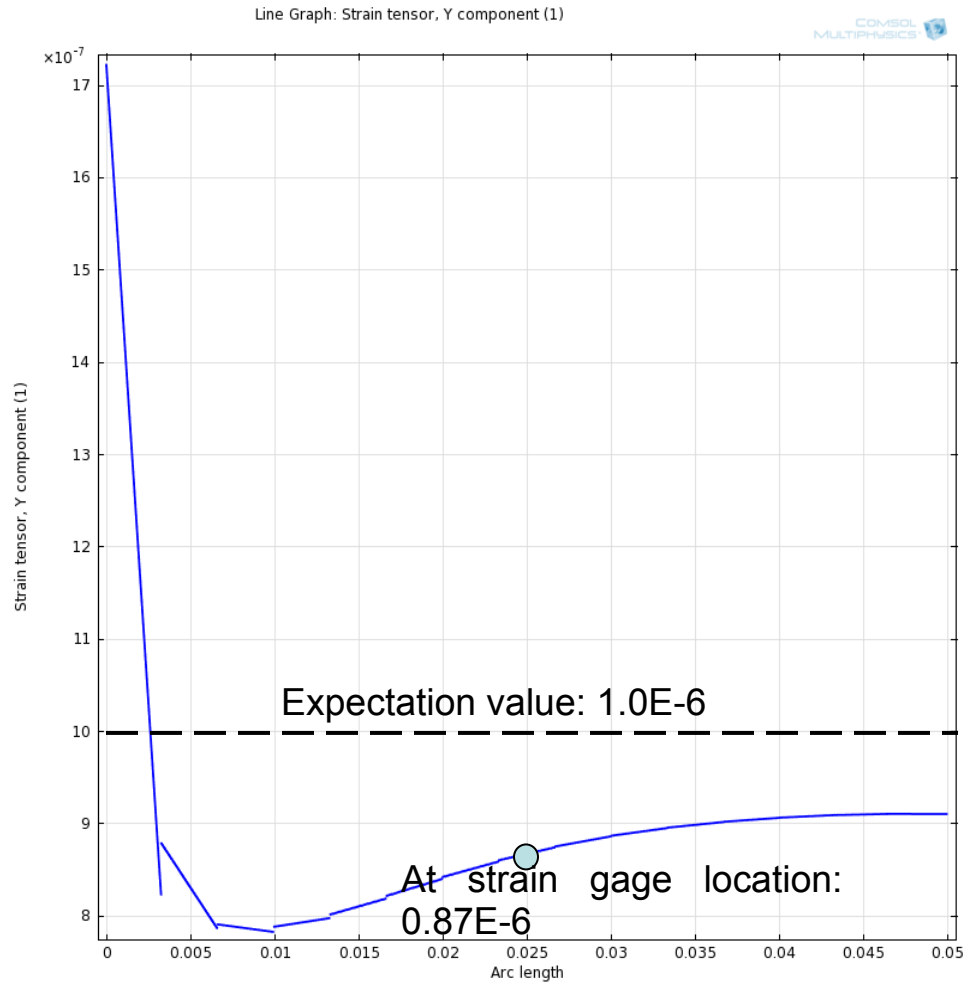


Figure 5.10 Strain variation along the height of the sample. “Arc length” represents the vertical position (bottom to top).

The above numerical model is still over simplified compared with real physical experiment setups. In our measurements, several cylindrical objects have to be stacked together. If not welded, the interface between them will never have a perfect match

between each other, as modeled in above numerical simulation. Such non-perfect interfaces will not only cause non-even azimuth stress distribution, it may also make the surface strain at gage locations wildly deviated from the expected value. These are repeatedly observed by experiments. In Figure 5.11, we applied static vertical stress to an aluminum cylinder through a non-welded contact, and record the resistance change on strain gages at 4 azimuth locations. Three types of different strain gages are used, and all of them show the stress is more concentrated around 270° to 0° location.

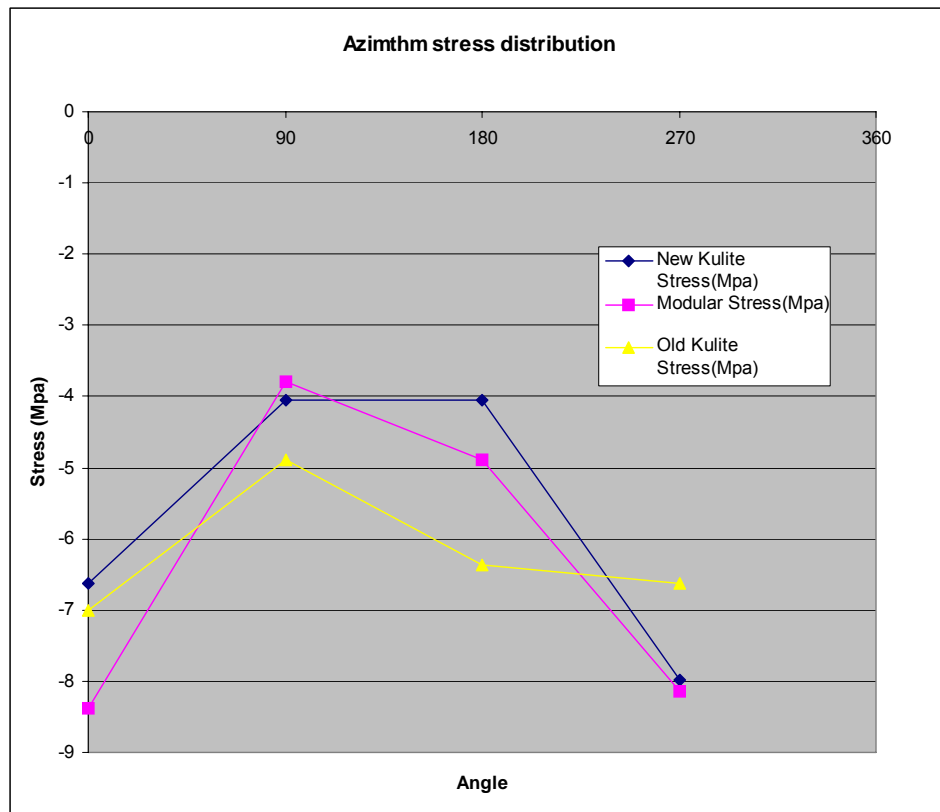


Figure 5.11 With non-welded contacts, the stress in an aluminum sample shows a strong azimuth variation.

Liu and Peselnick (1983) discussed this interface issue and suggested that all end surfaces must have flatness below 0.5 micron and slightly concave surfaces with radius

curvature large than 360 meter. From a microscopic view, when two non-flat surfaces touch each other, the touching will not cover the whole surface. Those not touched area will lose the support from each other thus cannot hold much stress. Those touched area will have to hold more stress to compensate the non-touched area, to reach the overall balance. While the total dynamic strain in our measurement must be controlled below 10^{-6} , the displacement at anywhere in a 5 cm long sample is below 50 nm. In this sense, if there is a gap thicker than 50 nm somewhere in the interface, it will separate the two pieces at that area without support to each other.

Based on this concept, we continued using numerical simulations to evaluate the effect of bad interface contact on stress distribution.

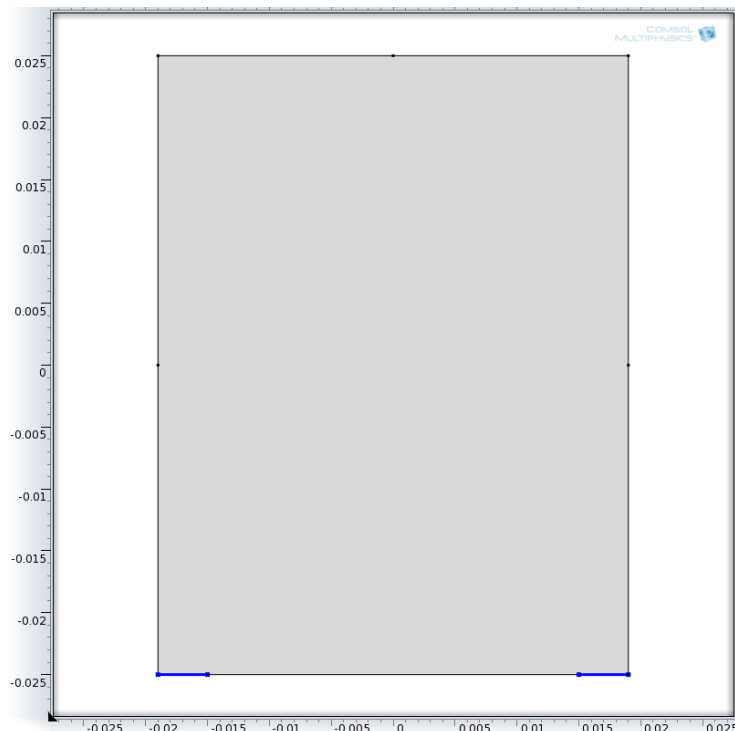


Figure 5.12 Numerical experiment setup to simulate the bad contact at center of the interface.

First, we simulated a concave surface case. Out of the total 19 mm radius, only the outmost 4 mm is firmly supported (Figure 5.12). The simulated strain distribution is displayed in Figure 5.13. Again, by plotting the surface strain along vertical axis, we found the strain at gage location is about 78% of the expectation value (Figure 5.14).

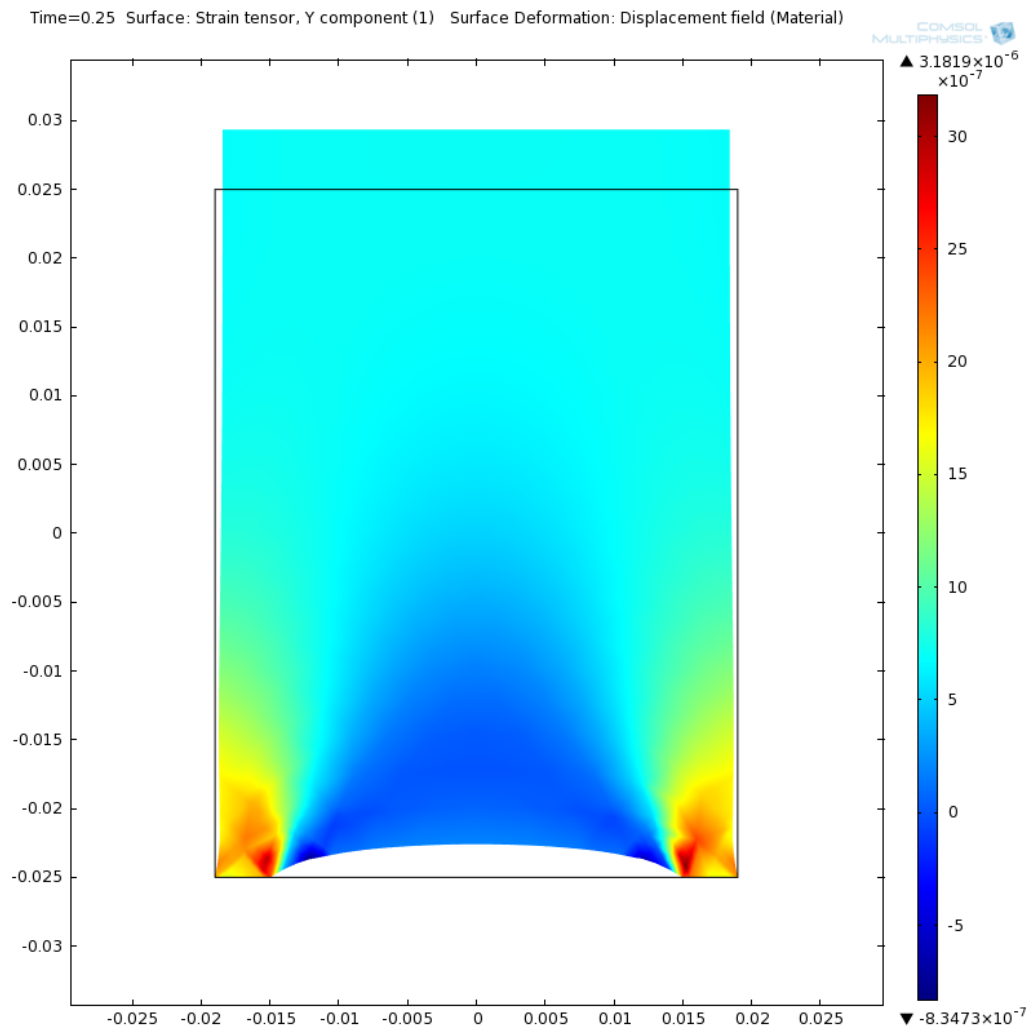


Figure 5.13 Strain distribution throughout the cylindrical core plug sample, with bad contact at center of the interface.

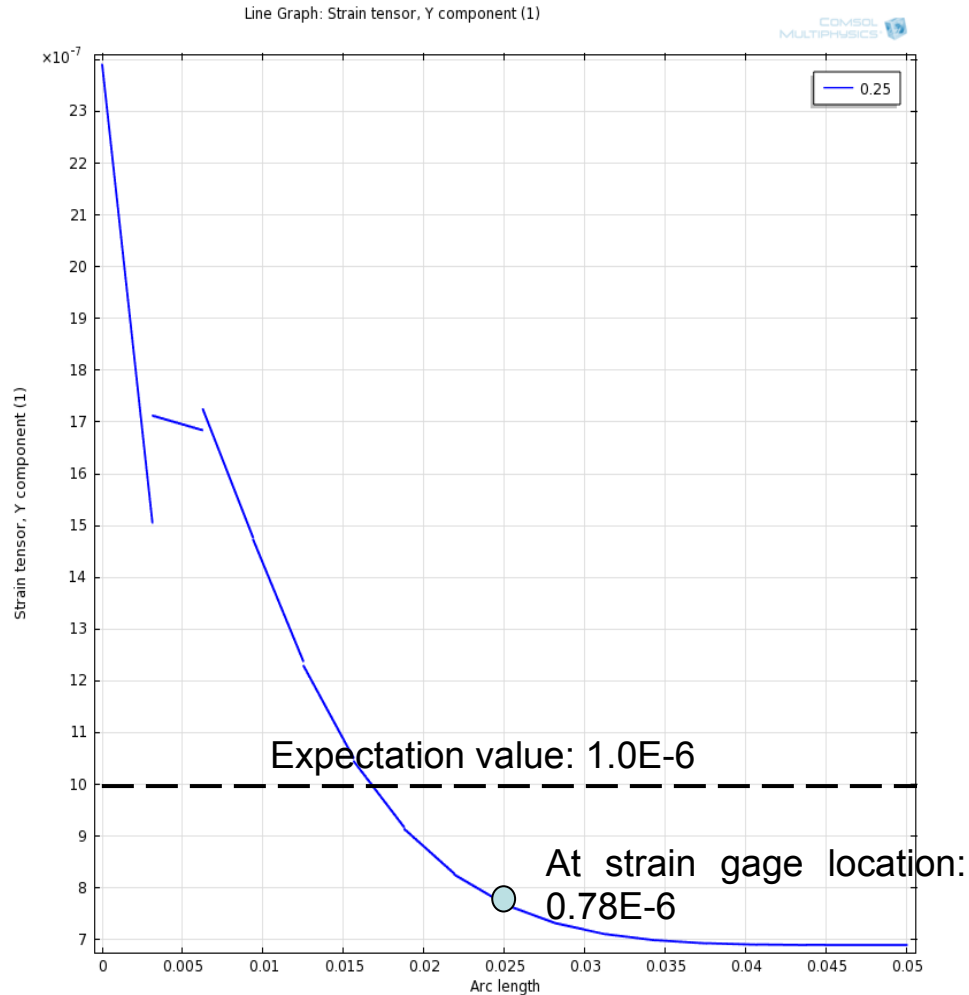


Figure 5.14 Strain variation along the height of the sample, with bad contact at center of the interface. “Arc length” represents the vertical position (bottom to top).

Next, we reversed the above case to simulate a convex surface, in which only the inner 15 mm radius is firmly supported. The boundary condition and simulated strain distribution are displayed in Figure 5.15. In Figure 5.16, although the strain at gage location has 93% of the expectation value, we should notice the curve is very steep, and the strain value goes all the way to zero and even negative, towards the bottom of the cylinder. This indicates that the measurement results are very sensitive to the location of

strain gage. That's why a convex surface must be avoided in non-welded experiment setup.

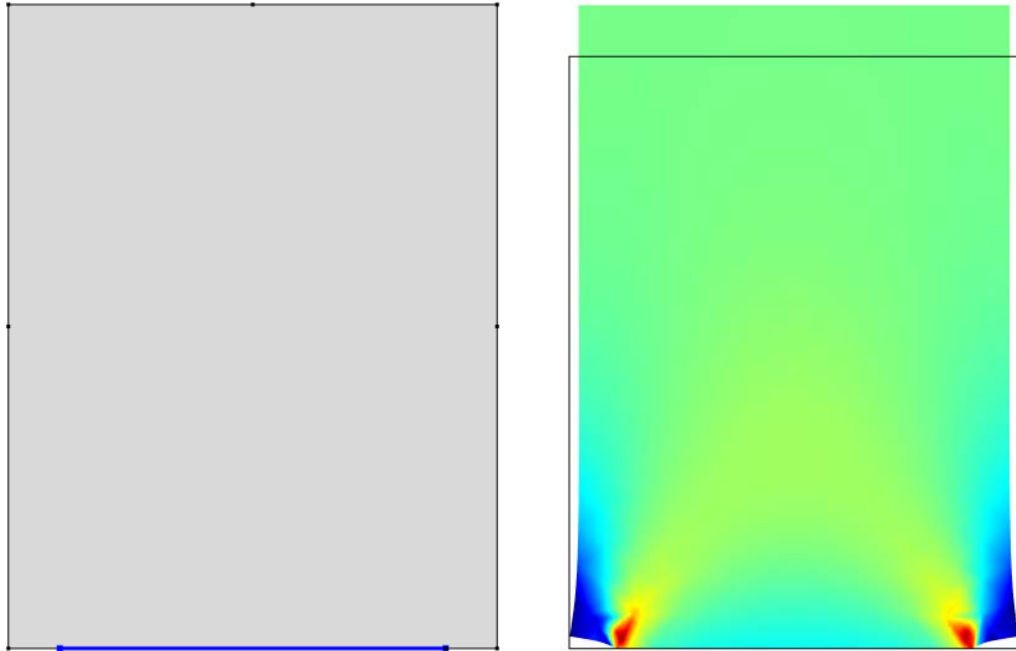


Figure 5.15 Left: Numerical experiment setup to simulate the bad contact at edge of the interface. Right: Strain distribution throughout the cylindrical core plug sample, with bad contact at edge of the interface.

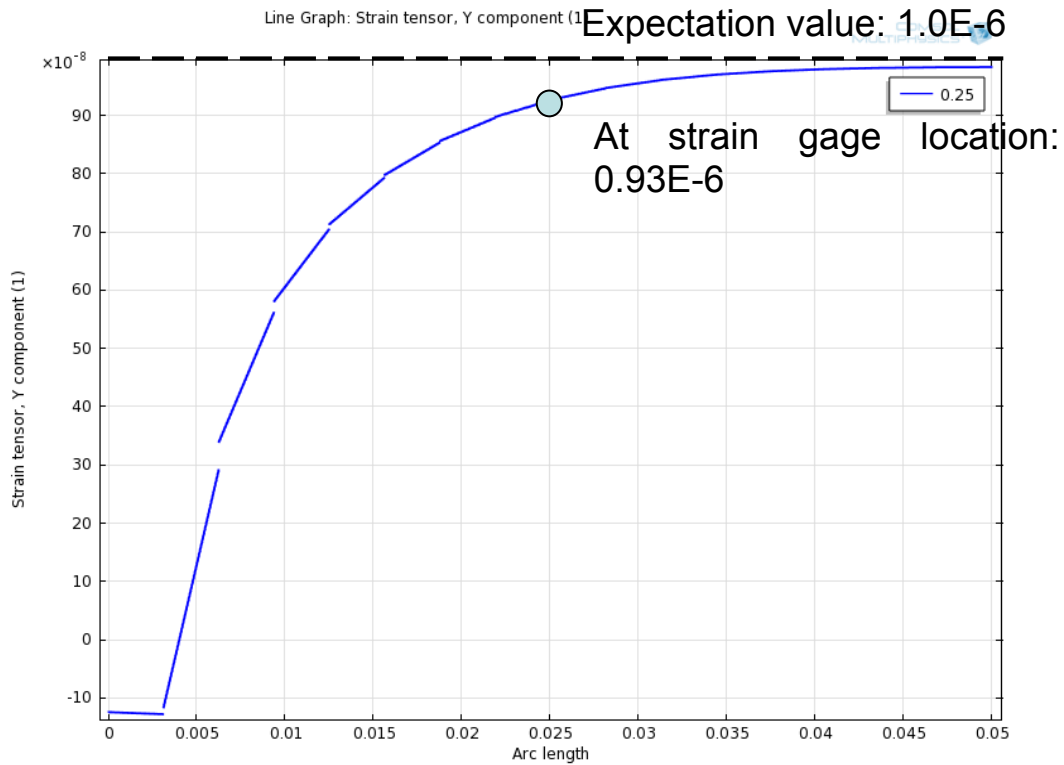


Figure 5.16 Strain variation along the height of the sample, with bad contact at edge of the interface.

“Arc length” represents the vertical position (bottom to top).

The requirements on end surface suggested by Liu and Peselnick (1983) are very demanding to a typical machine shop, and apparently not realistic if we want this kind of measurement a routine one. To solve this problem, our current approach is using epoxy to glue all surfaces together. The epoxy not only fills all the tiny gaps to provide firm support to whole surface, the natural curing process also has a self alignment function that helps to evenly distribute the stress azimuthally.

5.3.2 Acquisition: small signal protection

The small amplitudes of the strains and Wheatstone bridge outputs impose high challenge to the signal protection, noise isolation, and data acquisition. Besides the application of lock-in amplifier discussed above, we have taken many special cares on hardware building and instrument selection as well. Table 5.6 lists some of the major features.

Table 5.6 Special features in hardware and instrumentation to protect the small signals.

<i>Features</i>	<i>Functions</i>
Grounding	A dedicated “earthing electrode” is installed outside the building and wired to a thick copper busbar close to the system. The metal racks, frames, signal grounds (not AC power grounds) of each instrument are individually connected to the busbar to avoid ground loop between them.
Wiring	Coaxial cable is not able to transfer signals in micro volt level. Before the signals are amplified with our special “Shield drive amplifier”, each channel uses a shielded and paired cable from the Wheatstone bridge output to amplifier inputs. The potential in the shield of each cable is compensated by the feedback drive from the amplifier, to reduce common mode noises.
Shield drive amplifier	Besides 8 channels, 200 x high fidelity amplification, a special shield drive circuit is implemented in each channel, to provide compensation to noise potential in the input cable.
Differential and Pseudo-differential inputs	To effectively remove the common mode noises, an instrument input must be configured with differential or pseudo differential connection. A Wheatstone bridge with DC excitation is naturally a differential voltage source. The NI4498 acquisition board accepts only pseudo differential connection. The conversion from differential to pseudo differential is accomplished in the “Shield drive amplifier”.
NI PXI-4498 acquisition board	<ol style="list-style-type: none"> 1. 114dB dynamic range with 24 bit vertical resolution, minimum voltage sensitivity 37.7 nV. 2. 16 channel simultaneous sampling, not multiplexing sampling, to minimize the phase-mismatch between channels. 3. Maximum sample rate: 204.8 kHz. 4. AC-coupled analog inputs at 0.5 Hz.

5.4 Errors and calibrations

There are two types of errors in any physical experiment measurements (Taylor, 1982). The random errors affect the precision of the measurement results and systematic errors affect the accuracy of the results. In a traditional perspective, random error can be tackled by multiple measurements and statistical process; and systematic errors are possible to be corrected through careful calibrations. In our system, the random errors like environmental EMF noise, power line fluctuations have been suppressed through hardware and software. Adam *et al.* (2006) used least square fitting to evaluate the random errors in a similar apparatus. Their results show a standard deviation of 1.2 GPa in bulk modulus, and 0.3 GPa in shear modulus respectively. In Figure 5.17, we compare a typical measurement result of Young's modulus and Poisson ratio from our system, with the results by Adam *et al.* A similar comparison has done on the phases from our results and published results by Adam *et al.* (2009) and Piane *et al.* (2011), in Figure 5.18. These comparisons suggest our apparatus has an equal or better control on the random errors.

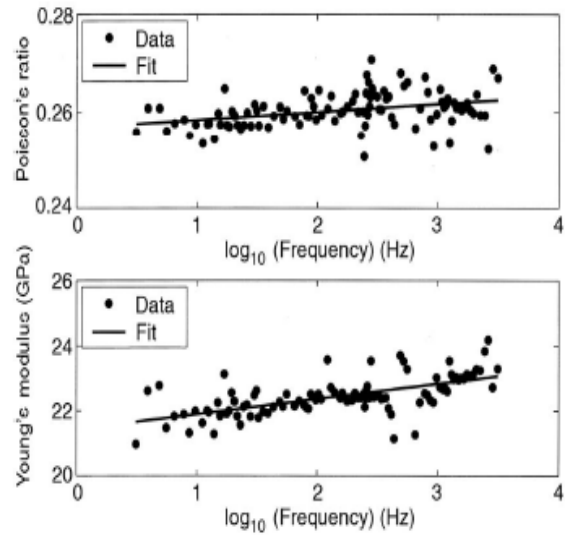
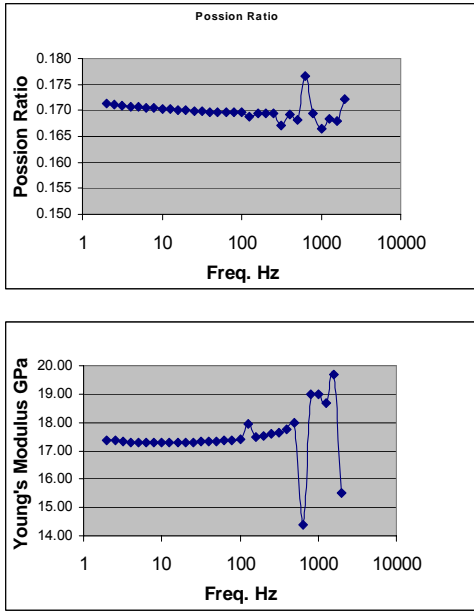


Figure 5.17 Comparison of random errors on Young's modulus and Poisson ratio, between our system (left) and Adam *et al.*, 2006 (right).

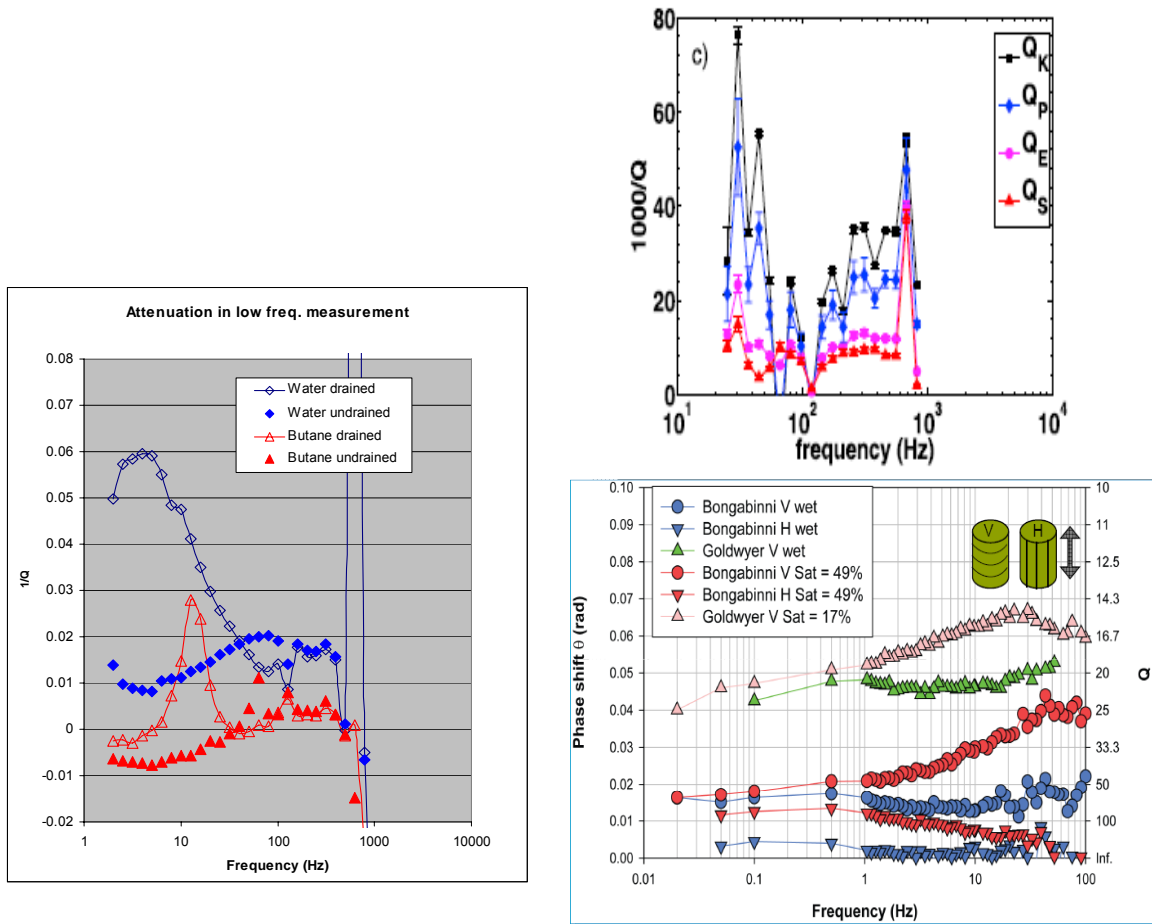


Figure 5.18 Comparison of random errors on attenuation, among our system (left), Adam *et al.*, 2006 (right top), and Piane *et al.*, 2011 (right bottom).

For systematic errors, we have identified several main sources and managed to calibrate each of them to reasonably close to true values. Two types of basic parameters are measured from the waveforms recorded for each channel. The first type is Young's modulus and Poisson ratio, which come from the amplitude ratio between strain gages. The second type is quality factor, which comes from the phase difference between strain gages. The causes of systematic errors on amplitude and phase are relatively independent to each other, so that we have chance to treat them separately.

5.4.1 Phase errors

Ideally, the measured phase should be only the reflection of the mechanical quality factor of the rock sample. But in actual experiments, we found that the electronic circuits can cause phase shift too, mainly due to the capacitance effects between wires. While we are not able to exactly model and quantify this effect with the parameters like capacitance values, we can design experiments to fully characterize such shifts, specific to each channel. These shift values are then used to calibrate the real measurement results to remove the electronic shift effects.

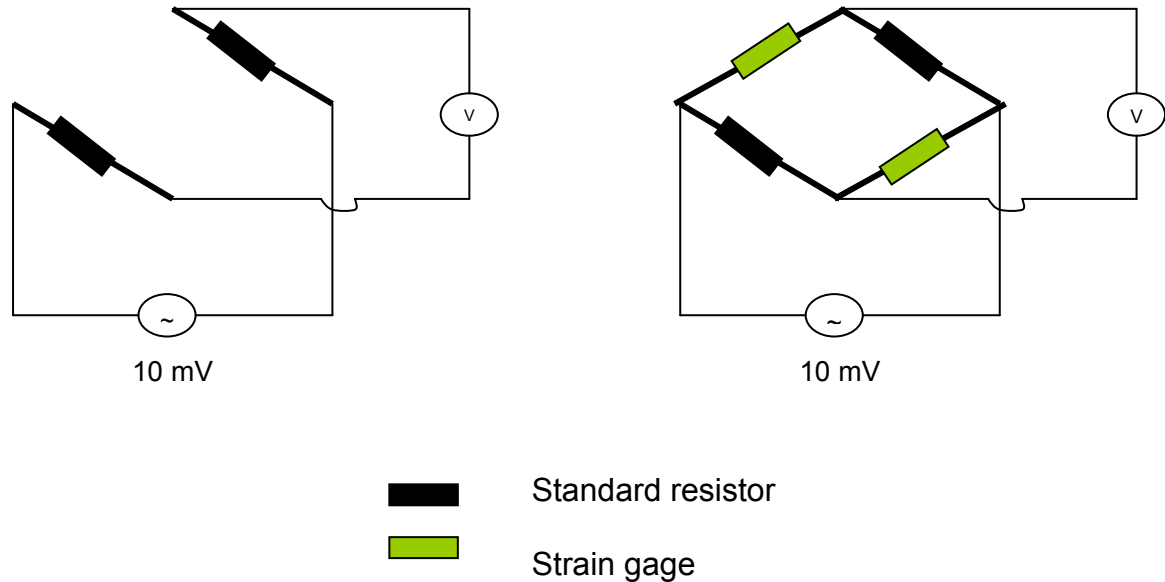


Figure 5.19 Introduce a 10mV AC signal to the original DC excitation input terminals, to calibrate the phase shift due to electronics. Left: without strain gage connected. Right: with strain gage connected.

In first experiment, we introduce a 10 mV AC signal (directly from the function generator) to the original DC excitation ports of the Wheatstone bridge board, without the

strain gages connected (Figure 5.19, left). In this setup, obviously there is no mechanical phase shift involved. The results in Figure 5.20 top shows that there are consistent phase shifts on all channels which go through Wheatstone bridges, cables, amplifier, to NI4498 input ports, compared with the reference channel that directly goes from function generator to the NI4498. Those shifts are frequency dependent. But differences among them are very small (< 0.1 degree below 10 Hz, and almost identical above 10 Hz). The measurement principles discussed in chapter 4 tells that it is the phase difference between sample and standard Young's gage outputs determines the quality factor. Therefore we can conclude that our electronic system including Wheatstone bridge board, all cable wiring, weak signal amplifier, and NI4498 input ports only generate minor phase shift errors which can be ignored.

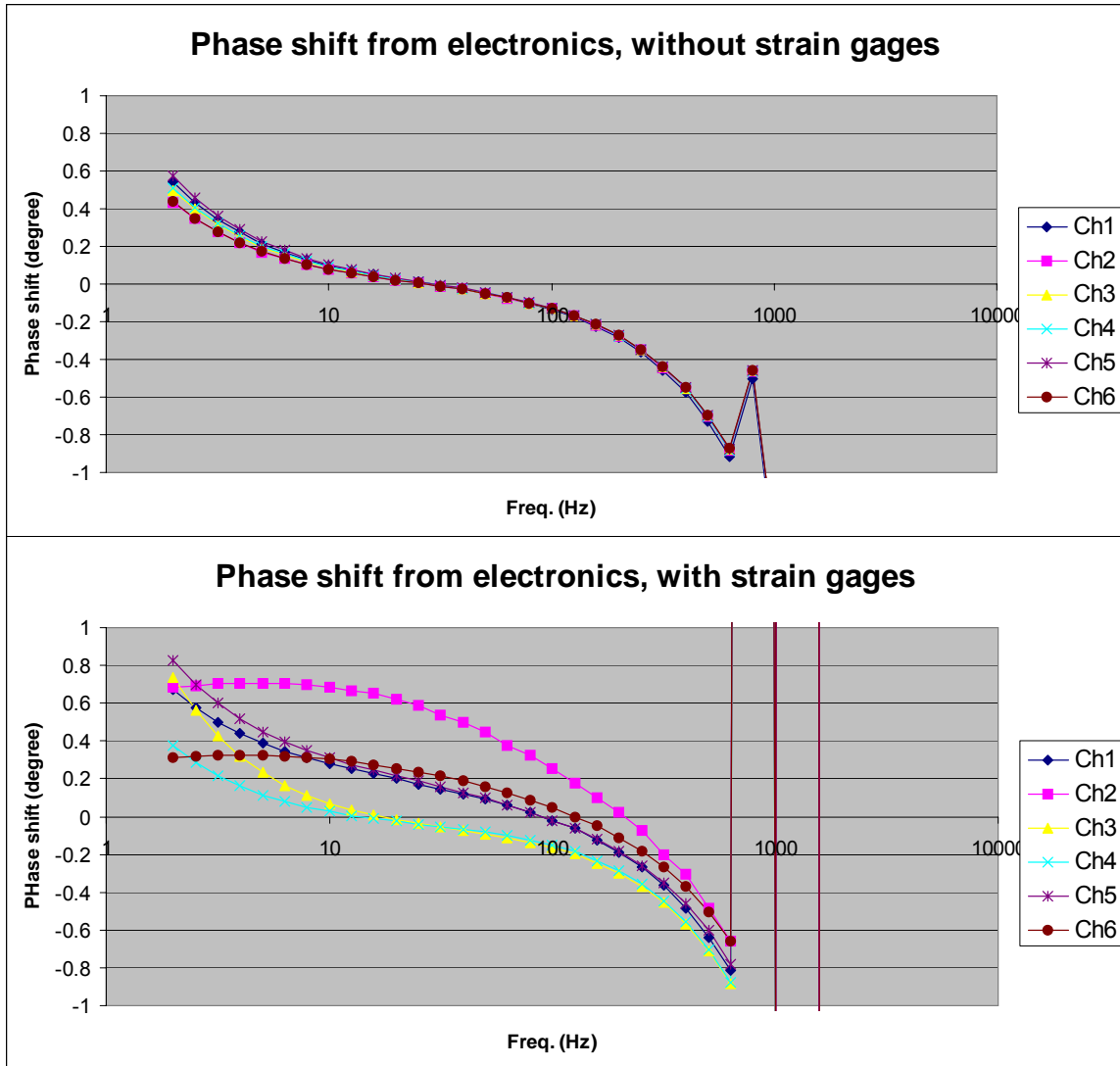


Figure 5.20 Phase shift from electronics. Top: without strain gages. Bottom: with strain gages.

However, when the strain gages are connected to the bridge board (Figure 5.19, right), more variations are brought in. First, the wiring from strain gage to bridge board is through simple twisted paired wires, not shielded cables. Second, the strain gages are glued to the sample or standard surface with epoxy. Varying factors like the epoxy layer thickness, moisture content inside epoxy, curing procedures can result in the variation on final capacitance value of each glued strain gage. As shown in Figure 5.20 bottom, with

all strain gages connected, we can now observe the phase shifts on each channels deviate to each other, sometimes with non-negligible values. For example, if one compares channel 2 (Young's gage on rock sample) to channel 6 (Young's gage on aluminum standard), there is a difference of about 0.4 at low frequency, and it eventually diminishes towards high frequency. This must be corrected from the real measurements. Otherwise it brings in error about 0.007 to the final I/Q quality factor value. And more importantly, the change of the error regarding frequency may mislead the interpretation on attenuation mechanism in the measured rock sample.

Although this kind of error seems quite random since they are highly depend on gage and epoxy quality, and installation procedure, it actually can be treated as systematic. Since once the strain gages are installed, their properties are mainly fixed and will not vary significantly from experiment to experiment. Therefore, the associated errors are systematic. Here the "systematic" does not refer to the whole measurement system but to a specific sample and standard assembly. The calibrations on this kind of errors are more costly compared with those system level (like instrumental) errors. But they are doable as demonstrated in Figure 5.20.

5.4.2 **Amplitude errors**

Similar to the analysis on phase shift, ideally the measured amplitudes should only be the reflection of mechanical properties (Young's modulus and Poisson ratio) of the rock sample and aluminum standard. In reality, there is couple of other factors

affecting the amplitude output as well. We need separate and calibrate those effects in order to obtain the “real” elastic parameters.

First of all, the gage factor (see chapter 4, equation 4.15) inherently has +/-5% error, according to the manufacturer’s specification. When we use the ratio from two independent strain gage outputs to calculate the Young’s modulus or Poisson ratio, the results may contain up to 10% error already. The gage factor is not measurable before the gage is actually installed. Once installed, it is impossible to remove the strain gage and install it onto another material. This tells that the gage factor of a strain gage can not be pre-calibrated. The strain gage installed on standard material with known modulus can be well calibrated, with the help of another independent stress or strain sensor. The real challenge comes from the calibration on strain gages installed on rock samples. Since the Young’s modulus of the sample is not known yet (to be measured), theoretically it is impossible to calibrate the gage factor by itself.

Up until now, the only practical approach we can use to calibrate the gage factor on rock sample is based on the assumption that a dry rock has no modulus dispersion. The modulus from an independent ultrasonic measurement on the same dry rock is used as the calibration point. Any deviations from this point by low frequency measurements are attributed to gage factor and other non-rock-property (discussed later) effect. This assumption is safe for certain rocks under certain conditions (well consolidated, clean sandstone, low strain level), but maybe questionable for others (like unconsolidated, or high shaly sandstone, or shale formation itself). We are still working on this issue for a

better solution. A non-strain-gage sensor, like LVDT, could be an ultimate measure to remove this issue.

Besides the gage factor, the installation of the strain gage also introduces certain errors to its amplitude output. As shown in Figure 5.10, due to the boundary condition, the stress is not uniformly distributed throughout the sample surface. The stress applied on each strain gage is rarely with the expected true value, and are sensitive to its installation location. The problem can be even worse when the length to radius ratio is smaller (Moghe and Neff, 1971). However, we believe this effect is purely in elastic domain hence is not frequency dependent. Based on this assumption, we can group this effect together with the gage factor effect discussed above, and use a single calibration to treat both of them.

5.5 Tests

In this section, I will use three tests to demonstrate the performance of the low frequency measurement system. They are carried out on aluminum, Lucite, and sandstone respectively. In all three tests, the standard material used is always Aluminum with its Young's modulus known as 69 GPa.

5.5.1 Test 1: Aluminum

Since we use aluminum as standard, to measure modulus and attenuation in other materials, the most effective and straightforward method to test the performance of the

system is to use another piece of aluminum as sample. Since aluminum is believed to be non-dispersive and non-attenuative, there are two expectations from this test: the Young's modulus should be flat without frequency dependency and the phase shift or quality factor should be close to zero.

For this purpose, we used two cylinders made of same aluminum material, glued together by epoxy. Four strain gages are installed vertically at middle of each cylinder, with even azimuth distribution at 0° , 90° , 180° , and 270° respectively (Figure 5.22). Strain gages at 0° and 180° along with two standard precision resistors form a Wheatstone bridge, which is designated as channel 1; and the same for 90° and 270° as channel 2. The whole assembly is installed onto the vibration system. The measurement is from 2 Hz to 2000 Hz, consisting 31 points, evenly distributed on 10-based logarithm scale of frequency.

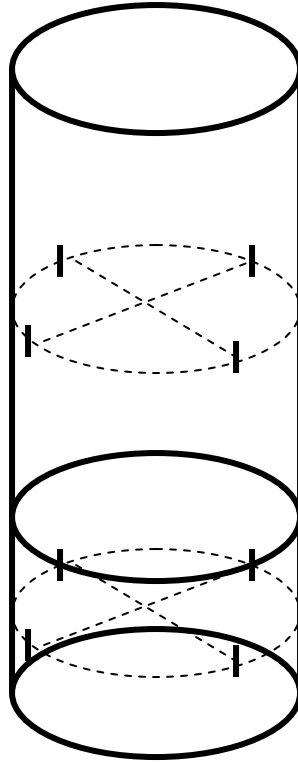


Figure 5.21 Four strain gages are installed vertically at middle of each cylinder, with even azimuth distribution at 0° , 90° , 180° , and 270° respectively.

The results in Figure 5.23 show that the value of Young's modulus is around 71 rather than 69 GPa. The discrepancy is caused by the systematic errors sources like gage factor and gage installation as discussed in section 5.4. However, before the resonance takes its effect above 600 Hz, we find the measured Young's modulus doesn't show any dispersion trend, and the random fluctuation is also very small. Similarly, the measured quality factor has its value within ± 0.002 in that frequency range. Both results meet our expectations. This also confirms that a thin layer of cured epoxy between sample and standard does not bring in any observable dispersion and attenuation into the measurement results.

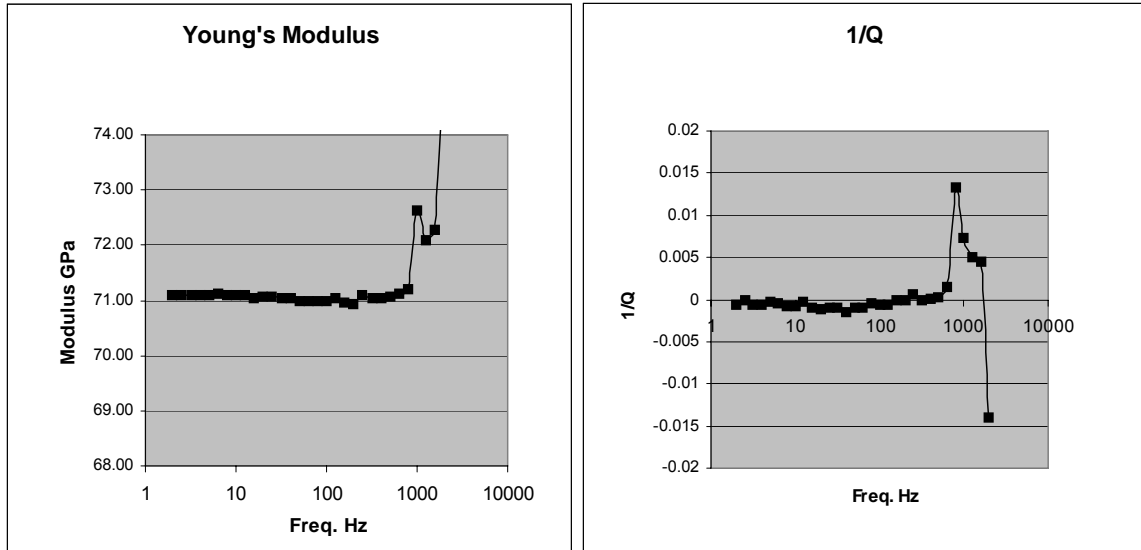


Figure 5.22 Calibration on Aluminum show no dispersion on Young's modulus and a negligible attenuation value.

5.5.2 Test 2: Lucite

In this test, we used a Lucite cylinder as the sample. Lucite is a medium dispersive and attenuative material with very high homogeneity. Therefore it has been frequently used as a testing material to demonstrate the frequency dependent modulus and attenuation measurement apparatus. Spencer (1981) reported Lucite has $1/Q$ value between 0.04 and 0.08, at 4-400 Hz frequency range. Liu and Peselnick (1983) obtained a slightly low value between 0.04 and 0.06, at 0.01 to 1 Hz frequency range. Lakes' (2009) result is slightly high between 0.06 and 0.09, at frequency 0.1 to 100 Hz. And most recently, Tisato *et al.* (2011) published a more tight result between 0.06 and 0.08 in the same frequency range as in Lakes (2009). It is worth to check whether our system will get a result comparable to those literature values.

The experiment setup is similar to test 1, except that on Lucite sample 4 more strain gages are installed horizontally just above the 4 vertical ones. This will enable us to obtain the Poisson ratio as well. The ultrasonic velocity V_p , V_s as well as the density are measured separately and converted to Young's modulus and Poisson ratio, as listed in Table 5.7.

Table 5.7 Lucite properties measured by ultrasonic transducers (1MHz).

Description	Value	Unit
P-wave velocity V_p	2.708	km/s
S-wave velocity V_s	1.372	km/s
Density ρ	1.187	g/cc
Young's modulus E	5.934	GPa
Poisson ratio ν	0.327	

The measurement results are plotted in Figure 5.24. For Young's modulus and Poisson, the ultrasonic values are also displayed, but for $1/Q$, there is no ultrasonic data available.

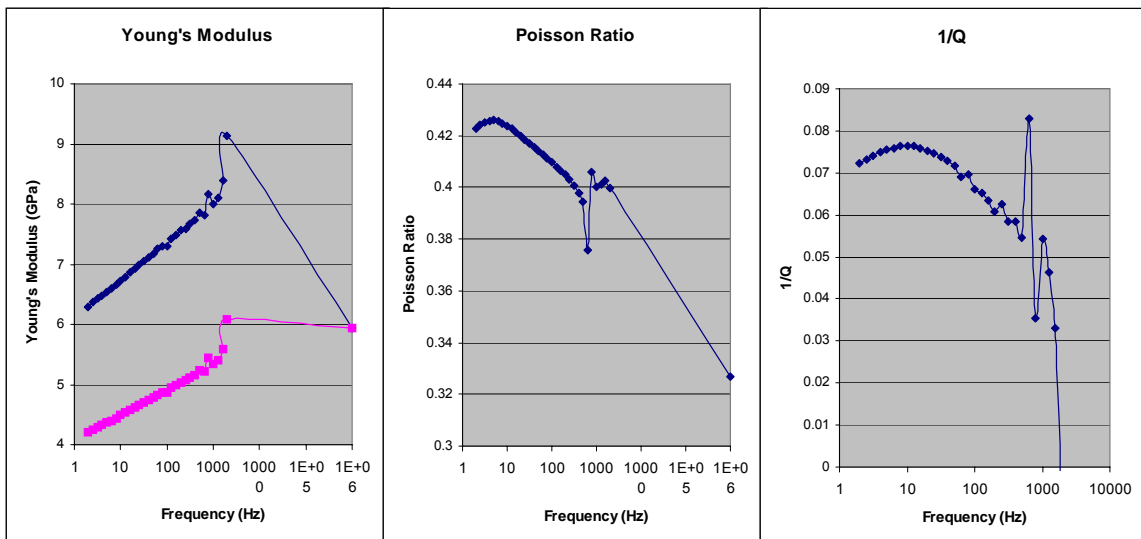


Figure 5.23 Measured Young's modulus, Poisson ratio, and attenuation $1/Q$, on a Lucite sample.

First, the measured Young's modulus (dark blue curve) exhibits a continuous increasing trend vs. frequency, indicating a strong dispersion in this material. But when compared with the ultrasonic value, it is obvious that all low frequency values are systematically higher. As discussed in section 5.4, this error is strain gage related and can only be corrected based on certain assumptions. Unfortunately, for Lucite one can not use the assumption as in dry rock sample. Thus we lack an effective way to calibrate the absolute Young's modulus value in dispersive materials. The red curve is indicating the results that would be obtained if an appropriate calibration could be performed, as a demonstration how a reasonable low frequency modulus curve would look like. Nevertheless, disregard the unreasonable absolute values, the frequency trend in measured Young's modulus is still valuable to interpret the anelastic behavior and mechanism in measured material.

Second, the measured Poisson ratio exhibits decreasing trend vs. frequency. It indicates that for Lucite, the rigidity decays faster than the stiffness when the frequency goes lower. This behavior is somewhat similar to shale formation, which can not hold shear stress at geological time scale, but appears as a solid under normal time scale. However, one should also notice this trend is broken, or even reversed when frequency is below several Hz. This suggests Lucite will never really flow like a liquid even an infinite time is given. Such property distinguishes the Lucite from those super viscous liquids, like tar.

Finally, we found the measured quality factor $1/Q$ is between 0.06 and 0.08, with a peak around 10 Hz. This result is in good agreement with published literatures mentioned above, especially with the most recent result reported by Tisato *et al.* (2011).

The test with Lucite confirms that our low frequency system can fully catch the dispersion and attenuation features from viscoelastic samples.

5.5.3 Test 3: Rock sample

The ultimate goal to develop the low frequency measurement system is to study the dispersion and attenuation in real sedimentary rocks, especially those associated with fluid flow. In this test, we used a Berea sandstone as the sample, measured and compared the properties under dry and water saturated conditions, to check whether our system can detect any fluid flow related dispersion and attenuation.

Before low frequency measurement, the dry V_p and V_s of this sample were measured under ultrasonic frequency. Then a Gassmann substitution was done to predict the low frequency properties. These values are listed in Table 5.8. Pressure is 750 psi.

Table 5.8 Ultrasonic measured dry properties, as well as low frequency properties predicted by Gassmann fluid substitution

Description	Dry by ultrasonic measurement	Water saturated by Gassmann	Units
Porosity ϕ	22.86%		
Bulk density ρ	2.035	2.264	g/cc
P-wave velocity V_p	3.33	3.47	km/s
S-wave velocity V_s	2.18	2.06	km/s
Bulk modulus K	9.66	14.39	GPa
Shear modulus G	9.64	9.64	GPa
Young's modulus E	21.7	23.64	GPa
Poisson ratio ν	0.125	0.228	

For low frequency measurements, we first measured the dry properties under 750 psi confining pressure. Then the sample was saturated with water. Pore pressure was maintained at 300 psi, and confining pressure at 1050 psi. To evaluate the pore fluid line drainage effect (discussed in chapter 4), we ran two different tests. There is a valve placed very close to the entry point of the pore fluid line into the sample. In first run we closed this valve after the pore pressure reached the desired setting value, so that the sample pore system was on a closed or undrained condition. In second run, we opened this valve. Due to the fairly high permeability (407 mD) of this sample, the pore system inside the sample was well connected to the pore pressure control system, which includes the ISCO digital pump. The pump is equipped with a large fluid reservoir, and imposes a single dashpot like friction force relaxation mechanism into the whole fluid system; therefore the pore fluid inside the sample was under a typical partially drained condition with a viscous boundary.

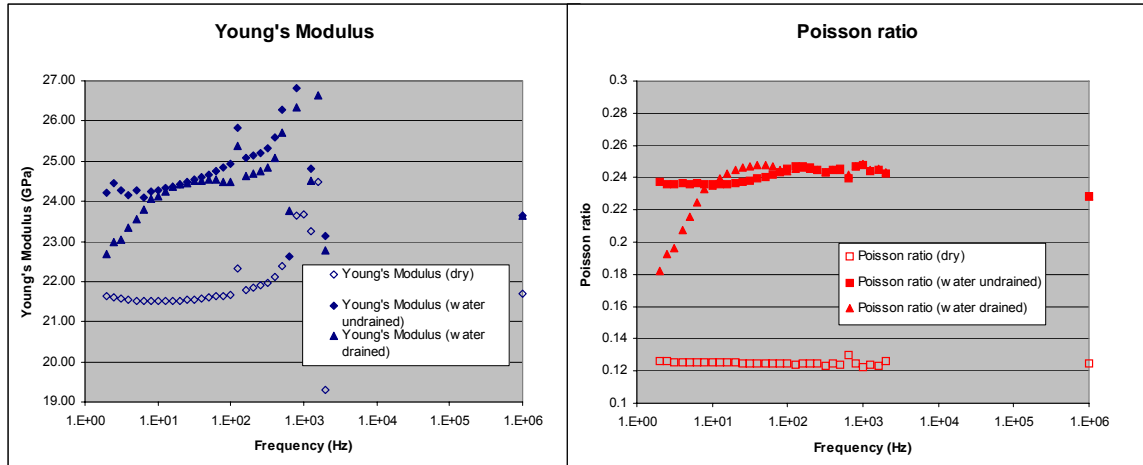


Figure 5.24 Measured Young's modulus and Poisson ratio on a sandstone sample.

The measured Young's modulus and Poisson ratio under all three saturation conditions are plotted in Figure 5.25. All values are calibrated with dry ultrasonic data using procedures described in section 5.4. The most prominent feature in the figure is that for drained condition, both Young's modulus and Poisson ratio exhibit a strong dispersion below 10 Hz. It also well matches the high and narrow attenuation peak plotted in Figure 5.26. This is a clear indicator of fluid related dispersion and attenuation. More specifically, it is caused by the external flow partial drainage effect at the pore fluid line opening. (More details are analyzed in chapter 3 and chapter 4). According to the theories discussed in chapter 3, the fluid flow related dispersion is mainly reflected in bulk modulus but not on shear modulus. To confirm this, we converted the Young's modulus and Poisson ratio into bulk and shear modulus, and plot them in Figure 5.27. First we noticed at dry condition the bulk and shear modulus curves almost overlap to each other. This confirms $K/G \approx 1$ in dry sandstone, which is widely recognized by many investigators (*e.g.*, Smith *et al.*, 2003). Second, the shear

modulus is barely altered by the water saturation, no matter whether it's drained or undrained condition. Finally, for bulk modulus, although both conditions show clear fluid effects, one can see distinct behaviors in two cases. For closed valve measurement (undrained condition), bulk moduli in whole frequency range have values larger than Gassmann predicted zero frequency value, suggesting certain fluid pressure gradient not relaxed even in seismic frequency. Without the strong dispersion ramp as observed in open valve measurement (drained condition), we can still see a weak dispersion ramp between 10 Hz to 100 Hz. The attenuation data in Figure 5.27 also show a weak peak for undrained measurement at the same frequency range. At high frequency end, the drained and undrained moduli are quite close to each other, but at low frequency end, the drained bulk moduli drop to values much lower than Gassmann predicted value, and showing a trend approaching towards the dry bulk modulus, if the measurement can extend to lower frequencies. This is easy to understand using the "dynamic fluid modulus" concept developed in chapter 3. With the open drainage, although the rock is fully water saturated, but the water appears as having a zero bulk modulus at very low frequency, because no pore pressure can be built up if sufficient time is given. In velocity data, this will result in the saturated P-wave velocity even below the dry P-wave velocity, since the bulk moduli have no increment but the bulk density is increased. This is confirmed in velocity plots in Figure 5.27, which are calculated from our measured modulus.

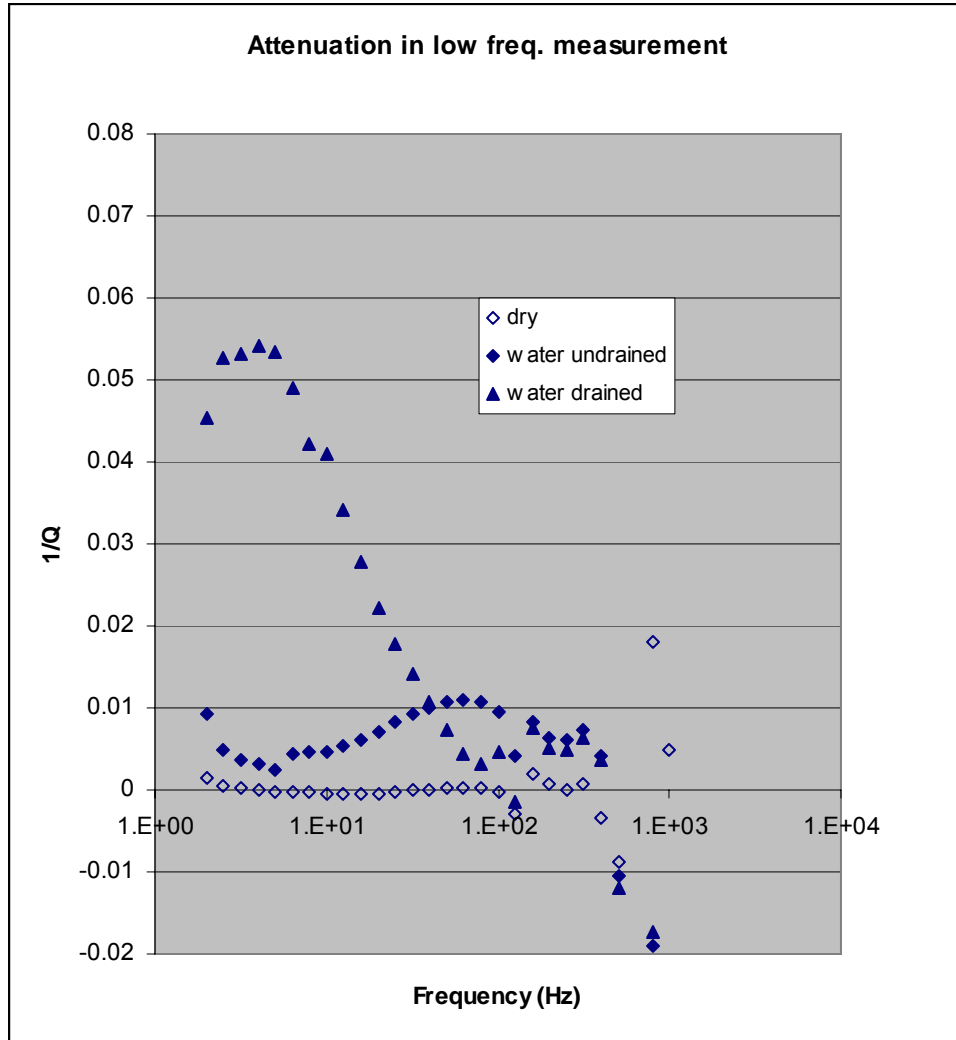


Figure 5.25 Measured attenuation 1/Q on a sandstone sample.

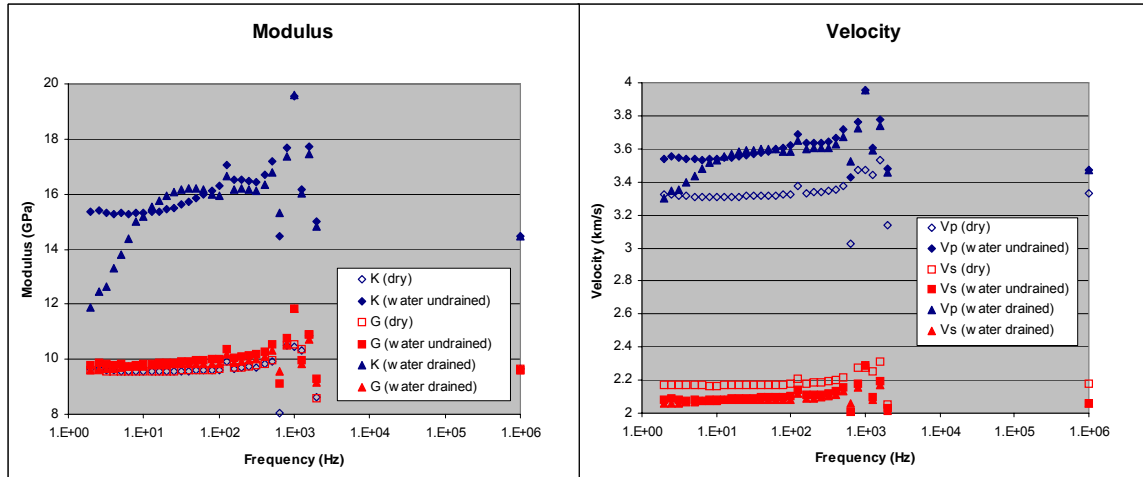


Figure 5.26 Calculated bulk and shear modulus (left), Vp and Vs (right) on a sandstone sample.

The test with real rock sample demonstrates our low frequency system can successfully detect the fluid flow related dispersion in modulus or velocity, and attenuation in wave energy. The measurement results can be used to distinguish different relaxation mechanisms (external flow or internal flow) in the sample.

5.6 References

Adam, L., M. L. Batzle, and K. T. Lewallen, 2009, Seismic wave attenuation in carbonates: *Journal of Geophysical Research*, **114**, B06208.

Adam, L., M. Batzle, and I. Brevik, 2006, Gassmann fluid substitution and shear modulus variability in carbonates at laboratory seismic and ultrasonic frequencies, *Geophysics*, **71**, F173-F183.

Batzle, M. L., D.H. Han, and R. Hofmann, 2006, Fluid mobility and frequency-dependent seismic velocity—Direct measurements: *Geophysics*, **71**, 1, N1–N9.

Das, A., 2010, The viscoelastic properties of heavy-oil saturated rocks, PhD dissertation: Colorado School of Mines.

Gautam, K, 2003, Fluid Effects on attenuation and dispersion of elastic waves, MSc thesis: Colorado School of Mines.

Hofmann, R., 2006, Frequency dependent elastic and anelastic properties of clastic rocks, Ph.D. dissertation: Colorado School of Mines

Lakes, R., 2009, Viscoelastic materials: Cambridge University Press.

Liu, H., and L. Peselnick, 1983, Investigation of internal friction in fused quartz, steel, plexiglass, and Westerly Granite from 0.01 to 1.00 Hertz: Journal of Geophysical Research, **88**, 2367-2379.

Piane, C.D., C. Madonna, D. Dewhurst, E. Saenger, and M. Raven1, 2011, Attenuation and physical properties of shales from the Canning Basin, Western Australia, Proceeding of 1st International Workshop on Rock Physics, Golden, 2011.

Madonna, C., N. Tisato, S. Boutareaud, and D. Mainprice, 2010, A new laboratory system for the measurement of low frequency seismic attenuation, SEG Expanded Abstract, 2675-2680.

Mikhaltsevitch, V., M. Lebedev, and B. Gurevich, 2011, A low frequency laboratory apparatus for measuring elastic and anelastic properties of rocks, SEG Expanded Abstract, 2256-2260.

Moghe, S.R., and H.F. Neff, 1971, Elastic deformations of constrained cylinders, Journal of Applied Mechanics, **38**, 393-399.

NI Lock-In Amplifier Start-Up Kit User Manual, 2006,
http://digital.ni.com/express.nsf/bycode/lockin?opendocument&lang=en&node=seminar_US, accessed Dec. 10, 2012

Spencer, J.W., 1981, Stress relaxations at low frequencies in fluid-saturated rocks: Attenuation and modulus dispersion: Journal of Geophysical Research, **86**, 1803–1812.

Taylor, J.R., 1982, An introduction to error analysis: University Science Books.

Tisato, N., C. Madonna, B. Artman, and E. Saenger, 2011, Low frequency measurements of seismic wave attenuation in Berea sandstone, SEG Expanded Abstract, 2277-2280

Smith, T.M., C.H. Sondergeldz, and C.S. Rai, 2003, Gassmann fluid substitutions: A tutorial, Geophysics, **68**, 430-440

5.7 Appendix A: Matlab code of Virtual Lock-in Amplifier

```
f_1=20; % signal freq, in Hz
f_s=1000; % sampling freq, in Hz
periods=600; % num of periods
nums_per_period=50; % num of sampling in each period
channels=8; %num of channels

N=periods*nums_per_period;

format long;
fid = fopen('G:\Yao\Work\Designs\Low
frequency\Electrical\lockin_by_DPSD \Yaodata\20000.txt','r'); %file
path for input data
    for i = 1:1:N;
        for j = 1:1:channels;
            a(j,i) = fscanf(fid,'%f',1); %read the data into
matrix of "channels" num of col,0
        end
    end
fclose(fid);

val_1=0;
val_2=0;

n=0:N-1;
ref_sin=sin(2*pi*n*f_1/f_s);
ref_cos=cos(2*pi*n*f_1/f_s); %generate sin & cos ref

for j = 1:1:channels;

    figure;
    subplot(2,1,1);
    plot(n,a(j,:), 'B');
    xlim([0,1000]); %only display 20 periods
    title('Waveform in time domain');
    xlabel('n');
    ylabel('Amplitude/V');

    subplot(2,1,2);
    M=fft(a(j,:),N);
    Y=fftshift(M)/(N/2);
    f=linspace(-f_s/2,f_s/2,N);
    plot(f,abs(Y)); % in freq domain
    xlim([0,f_s/2]);
    title('Frequency spectrum of the waveform');
    xlabel('f/Hz');
    ylabel('Amplitude/V');

    for i=1:N
        val_1=val_1+a(j,i)*ref_sin(i);
```

```

        val_2=val_2+a(j,i)*ref_cos(i);
    end
    val_1=val_1/N;
    val_2=val_2/N;

    Amp(j)=2.0*sqrt(val_1^2+val_2^2);    % retrieved amplitude
    Angle(j)=180.0*atan(val_2/val_1)/pi;    % retrieved phase in
degree

end

data=fopen('G:\Yao\Work\Designs\Low
frequency\Electrical\lockin_by_DPSD\Yaodata\amp_angle_20Hz_2.txt','wt');
%path for output file

fprintf(data, '\t\tAmplitude_ref/V\t\tPhase_ref/Celsius_degree\n');
fprintf(data, '        ref\t\t%17.15f \t', Amp(1));
fprintf(data, '%17.15f \n\n', Angle(1));

fprintf(data, '\t\tAmp_ch(i)/V\t\tPh_ch(i)-Ph_ref/Celsius_degree\n');
for i = 1:1:channels-2;

    % Amp_ch(i) = Amp(i+1)/Amp(1);
    Amp_ch(i) = Amp(i+1);
    Angle_ch(i) = Angle(i+1)-Angle(1);

    fprintf(data, '        ch%d\t\t', i);
    fprintf(data, '%17.15f \t', Amp_ch(i));
    fprintf(data, '%17.15f \n', Angle_ch(i));
end
fclose(data);

```

6 CONCLUSIONS

The existence of velocity dispersion and wave attenuation in sedimentary rocks not only imposes challenges to the interpretation of geophysical data, but also offers new opportunities to detect the fluids in subsurface. Through the effort by many investigators for several decades, the mechanisms of the dispersion and wave attenuation in fluid filled porous media have been well revealed. Theories and models have been developed to use rock and fluid parameters to predict the viscoelastic behaviors of seismic wave in such media.

To make the theories and models applicable to exploration geophysics requires more work to link the measured data to certain simple parameters that represent the heterogeneities of rocks and/or fluids. We have focused our efforts to this goal in two aspects: obtaining the robust data, and searching the easy to use parameters.

To obtain robust data, we have designed and built a low frequency measurement system in UH rock physics lab. From measured Young's modulus, Poisson ratio, and phase difference, the velocities and attenuation in rock samples can be obtained. Tests with the system demonstrate it can successfully detect the fluid flow related velocity dispersion and wave attenuation. The random error and system error are evaluated to be within reasonable level. Limited by the strain gage techniques, the current system may not obtain very accurate absolute values on modulus or velocity for soft rock samples like heavy oil sand. But the attenuation and relative dispersion trend are still

trustable. One of the major contributions in the laboratory work is that we have developed a virtual lock-in amplifier which greatly reduces the random errors, and improved the efficiency in data acquisition.

To search for easy to use parameters, we propose a new concept of dynamic fluid modulus, based on poroelastic analysis. This parameter can link the rock heterogeneity to the fluid flow within porous media, and quantitatively predict the velocity dispersion and wave attenuation. Modeling of multiple sets of heterogeneities becomes possible with this concept. Dynamic fluid modulus can also be deterministically inverted from measured data and help to reveal the characteristic heterogeneities in samples. Examples from both low frequency and ultrasonic measured data show that inverted dynamic fluid modulus can help to identify the type of fluid flows, and further infer the microstructure inside the sample.

For future works, first we need use the newly developed low frequency measurement system to obtain velocity dispersion and wave attenuation data in various sedimentary rocks. Second we need improve the methods on how to observe, describe, and characterize the heterogeneity in rocks. We plan to utilize advanced imaging technologies, like microCT, MRI, and SEM to explore in this direction. The goal is to evolve the heterogeneity descriptions from qualitative ones into quantitative ones, and link them to the dynamic fluid modulus, or other modeling parameters. Finally, we want to apply the newly developed techniques to field applications. One of the possible applications could be interpretation on abnormally high attenuation observed in

gashydrate-filled shallow formations. The growth of gashydrate in pore space alters the pore structure, and may create crack-like compliant pores. The resultant heterogeneity could be a contributor to the observed wave attenuation.

